Title

Solution-processable infrared photodetectors: Materials, device physics, and applications

Authors

Li, Ning

Mahalingavelar, Paramasivam

Vella, Jarrett H

et al.

Publication Date

2021-10-01

DOI

10.1016/j.mser.2021.100643

Peer reviewed

Materials Science & Engineering R 146 (2021) 100643

Contents lists available at ScienceDirect

Materials Science & Engineering R

journal homepage: www.elsevier.com/locate/mser

Solution-processable infrared photodetectors: Materials, device physics, and applications

Ning Li [a], Paramasivam Mahalingavelar [b], Jarrett H. Vella [c], Dong-Seok Leem [d], Jason D. Azoulay [b], Tse Nga Ng [a,*]

[a] Department of Electrical and Computer Engineering, University of California San Diego, La Jolla, CA, 92093, United States
[b] Center for Optoelectronic Materials and Devices, School of Polymer Science and Engineering, University of Southern Mississippi, 118 College Drive #5050, Hattiesburg, MS, 39406, United States
[c] Sensors Directorate, Air Force Research Laboratory, Wright-Patterson Air Force Base, OH, 45433, United States
[d] Samsung Advanced Institute of Technology (SAIT), Samsung Electronics, Co., Ltd., 130 Samsung-ro, Yeongtong-gu, Suwon-si, Gyeonggi-do, 16678, South Korea

ARTICLE INFO

Keywords:
Infrared semiconductors
Solution processing
Thin-film photodetectors

ABSTRACT

This review is written to introduce infrared photon detectors based on solution-processable semiconductors. A new generation of solution-processable photon detectors have been reported in the past few decades based on colloidal quantum dots, two-dimensional materials, organics semiconductors, and perovskites. These materials offer sensitivity within the infrared spectral regions and the advantages of ease of fabrication at low temperature, tunable materials properties, mechanical flexibility, scalability to large areas, and compatibility with monolithic integration, rendering them as promising alternatives for infrared sensing when compared to vacuum-processed counterparts that require rigorous lattice matching during integration. This work focuses on infrared detection using disordered semiconductors so as to articulate how the inherent device physics and behaviors are different from conventional crystalline semiconductors. The performance of each material family is summarized in tables, and device designs unique to solution-processed materials, including narrowband photodetectors and pixel-less up-conversion imagers, are highlighted in application prototypes distinct from conventional infrared cameras. We share our perspectives in examining open challenges for the development of solution-processable infrared detectors and comment on recent research directions in our community to leverage the advantages of solution-processable materials and advance their implementation in next-generation infrared sensing and imaging applications.

1. Introduction

Photodetectors that convert photons to electrical signals are the foundation of light detection technologies. Depending on the range of electromagnetic radiation absorbed by the active material, photodetectors are given different classifications, these include e.g., X-ray detectors, visible detectors and infrared (IR) detectors. Infrared light detection [1–7] underpins applications spanning diverse areas such as biomedical sensing, environmental surveillance, industrial inspection, among many other areas. Commercially available IR detectors are predominantly based on vacuum-processed inorganic compound semiconductors, which are structurally rigid, brittle, and require fabrication via complex epitaxial growth and costly processes. A new generation of solution-processable semiconductors have been reported in the past few decades including colloidal quantum dots (CQDs) [1,8,9], organic semiconductors (OSCs) [4,7,10,11], perovskites [1,12,13], and two-dimensional (2D) materials [5,14]. These materials offer sensitivity within the IR spectral regions and the advantages of ease of fabrication

Abbreviations: 1D, 2D, one-dimensional, two-dimensional; BHJ, bulk heterojunction; BLA, bond length alternation; CCN, charge collection narrowing; CMOS, complementary metal oxide semiconductor; CP, conjugated polymer; CQDs, colloidal quantum dots; CT, charge-transfer; DA, donor-acceptor; FET, field-effect transistor; FP, Fabry–Perot; FPA, focal plane array; FWHM, full-width at half-maximum; HOMO, highest occupied molecular orbital; IR, infrared; LHJ, layered heterojunction; LED, OLED, light emitting diode, organic light emitting diode; LUMO, lowest unoccupied molecular orbital; MCT, mercury-cadmium-telluride; NFA, non-fullerene acceptor; OSCs, organics semiconductors; PC, photoconductor; PD, OPD, photodiode, organic photodiode; PPG, photoplethysmography; PT, phototransistor.

* Corresponding author.
E-mail address: tnn046@ucsd.edu (T.N. Ng).

https://doi.org/10.1016/j.mser.2021.100643
Received 28 June 2021; Received in revised form 27 August 2021; Accepted 7 September 2021
Available online 14 September 2021

at low temperature, tunable materials properties, mechanical flexibility, scalability to large areas, and compatibility with monolithic integration. Thus they are promising alternatives for IR sensing when compared to their vacuum-processed counterparts that require rigorous lattice matching during integration.

The rapid developments in solution-processable IR photodetectors enrich detector functionalities on account of the synthetically tailorable properties and tunable optoelectronic characteristics of the semiconducting materials. These solution-processable IR materials enable new concepts for photo sensing, including upconversion pixeless imaging [15–17], trap-assisted photomultiplicative gain [18–20], and non-planar form factors [16,21,22] in IR sensing systems. The progresses in such IR sensing technologies will be tremendously beneficial for both civilian and defense applications.

This review is written to introduce infrared photon detectors based on solution-processable semiconductors, as opposed to infrared thermal detectors. We explore recent advances in solution-processed IR detectors in terms of functional materials, device physics, and novel applications enabled by these materials. In general, there are three types of photon detector structures: photodiodes, photoconductors, and phototransistors [11,13]. The three types of detectors have their own characteristic features in terms of photosensitivity, response speed, noise level, and device size. Deliberate device configurations can enable sensing functions such as upconversion detectors [4,23] and multispectral detection and imaging [24,25]. When compared to prior reviews [1–5], this work focuses on IR detection using disordered semiconductors, including organics, CQDs, and low dimensional materials, to articulate how the inherent device physics and behavior are different from conventional vacuum-processed inorganic semiconductors.

First, we present a brief introduction of IR detectors, including a technology timeline, to explain the motivation and need for the development of new IR detection materials. The advantages and disadvantages of traditional vacuum-processed semiconductors and solution-processed semiconducting materials are compared. The second section of this review details mechanisms of operation in disordered materials, including charge generation, transport, and collection. We also discuss the diversity of detector configurations and material properties such as charge mobility and trap density that affect the performance characteristics of IR detectors. In the third section, the performance metrics for detectors are presented, in terms of responsivity, noise, detectivity, response speed, and photo-multiplicative gain. In the fourth section, we survey the performance of detectors based on solution-processable semiconducting materials, including CQDs, 2D materials, organics, and perovskites. The performance of each material family is summarized in tables. The fifth section of this review presents device designs unique to solution-processed materials, including narrowband photodetectors and pixel-less up-conversion imagers, and highlights application prototypes distinct from conventional IR cameras. Last, we share our conclusions and perspectives and examine open challenges that remain in the development of solution-processable IR detectors. For example, the disorder inherent to solution-processed semiconductors introduces trap states that impact the detector performance. Throughout the review, we comment on recent research directions in our community so as to leverage the advantages of solution-processable materials and advance their implementation in next-generation IR sensing and imaging applications.

1.1. History of infrared detectors

This section introduces infrared detection from a unique historical perspective, intended to add background information to standard detector review articles [2,26] or textbooks [27].

1.1.1. Discovery of infrared radiation

The first infrared detector was technically a mercury thermometer placed behind a prism. On a sunny, spring day in April of 1800, William Herschel mounted a rocksalt prism behind a hole in a wall. This separated incident sunlight into its component wavelengths. Herschel carefully constructed an array of thermometers and placed them 0.25 in. behind the lowest energy, barely visible red wavelengths transmitted by the prism. He incrementally moved the thermometers further away from the barely visible, red colors. Table 1 describes his observations, adjusted for ambient temperature [28].

He went on to describe his observations:

> "[T]here are rays coming from the sun, which are less refrangible than any of those that affect the sight. They are invested with a high power of heating bodies, but with none of illuminating objects; and this explains the reason why they have hitherto escaped unnoticed."

He divided the solar spectrum into two regions: the *prismatic spectrum* and the *thermometrical spectrum*. Today, the *prismatic spectrum* is the visible region, wavelengths between 0.4−0.75 μm. The *thermometrical spectrum* has been subdivided into several different regions: the near infrared (NIR, 0.75–1 μm), the shortwave infrared (SWIR, 1−3 μm), the midwave infrared (MWIR, 3–5 μm), the longwave infrared (LWIR, 8–15 μm), and the far infrared (>15 μm). There are other sub-divisions of the IR past LWIR, but since they are not presently accessible using solution-processed photodetectors, they are not described here. The corresponding wavelengths and frequencies for each region are shown in Fig. 1a, and b compares the detector response of various semiconducting materials.

Different materials absorb light in different spectral regions. For example, imaging under SWIR light enables the inspection of objects behind a silicon (Si) wafer, because Si is opaque in the visible region but transparent in SWIR (Fig. 1c and d). For any object with a temperature above absolute zero, thermal emissions (MWIR and LWIR signatures) exist. Fig. 1e and f compare the SWIR and MWIR images of two cups of water at different temperatures, respectively. While visible or SWIR light cannot differentiate the temperature of the water, the MWIR image distinguishes objects with different temperatures [29]. This demonstration underscores the differences in detectors and their sensitivity to different wavelengths.

Fig. 2 depicts the principal types of solution-processable IR detectors in use today, alongside their current-voltage characteristics. These detectors include photoconductors, bolometers, photodiodes, and phototransistors. Briefly, a photoconductor absorbs incident photons and converts them to electron-hole pairs, which then drift to their respective electrodes under an external bias. A bolometer uses thermally induced changes in resistance to detect IR radiation. A photodiode generates charge carriers within the depletion region of two oppositely doped semiconductors. A phototransistor is basically a version of a photoconductor with an additional gate electrode that serves to enhance the photoresponse.

1.1.2. Photoconductors

The photoconductor was accidentally discovered in 1873 by Latimer Clark and Willoughby Smith while investigating materials for use in underwater telegraph cables [30]. In a typical experiment, selenium bars 5−10 cm long and 1–1.5 mm in diameter were sealed in a glass tube, with platinum wires attached to either end of each bar to act as electrical connections. They became confused when there were large discrepancies in the electrical resistance of each bar when measured by different people. This was eventually determined to be caused by the

Table 1
Herschel's data for thermometer number one.

Line number	Position behind Red (inches)	Temperature Rise, No.1
1	0.25	6.5
2	0.5	2.75
3	1	5.25
4	1.5	3.125

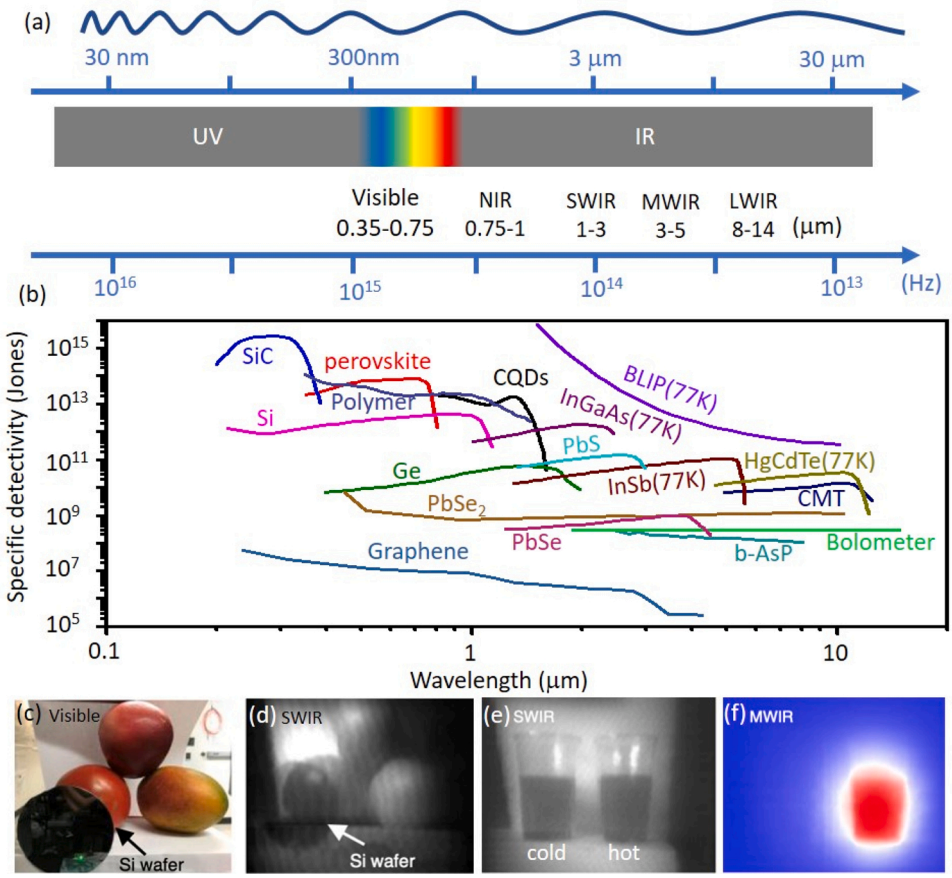

Fig. 1. (a) The spectrum of electromagnetic waves spanning from ultraviolet (UV) to IR. (b) Typical semiconducting materials for UV-IR light detection. (b) Typical semiconducting materials for different spectral ranges. (c) Visible and (d) SWIR images of objects. (e) SWIR and (f) MWIR image of two cups of water at different temperatures. (c-f) were reproduced with permission of Ref. [29].

absorption of light:

> "[W]hen the bars were fixed in a box with a sliding cover, so as to exclude all light, their resistance was at is highest, and remained very constant. [When] the cover of the box was removed, the conductivity increased from 15 to 100 per cent. [sic] according to the intensity of the light falling on the bar."

The effect persisted even when the device was immersed in water to minimize changes in external temperature. Clark and Smith did not name this effect, but today this is regarded as the first documented case of a photoconductor.

A photoconductive detector consists of a semiconductor sandwiched between two electrodes. A direct current bias is typically applied across the semiconductor which has a resistance in the MΩ range. Absorption of light by the semiconductor generates pairs of electrons and holes, which drift under the action of an external bias to the appropriate electrode. The semiconductor electrical resistance temporarily decreases, which is measured through changes in current.

1.1.3. Bolometers

Frustrated by the lack of sensitive IR detectors (mainly the 1836 thermopile) [31], Samuel Langley in 1881 connected identical lengths of various metals using a Wheatsone Bridge with a galvanometer to measure changes in current. Metal on one side of the bridge was exposed to heat sources, and the other was shielded. He named his device the Actinic Balance because it strongly resembled in shape and packaging, the type of analytical balance used by contemporary chemists: [32]

> "It measures radiations and acts by the method of the 'bridge' or 'balance,' there being always two arms, usually in juxtaposition, and exposed alike to every similar change of temperature arising from surrounding objects, air-currents, etc., so that the needle is (in theory at least) only affected when radiant heat, from which one balance-arm is shielded, falls on the other. Its action, then, bears a close analogy to that of the chemist's balance."

Eventually, the name Actinic Balance fell out of favor and was replaced by the terminology of bolometer. The first example made of iron generated a current of 0.4765 Wb for a 102.3 °C temperature rise. In the 19th century, Weber was a CGS unit for electric current, not magnetic flux as it is in the SI system.

In a Nature article from 1898, [33] the detector sensitivity had improved to the point where it could detect thermally induced current changes of 1.2 pA resulting from a temperature change difference of 10^{-7} °C. The development of the bolometer continued and in a 1907 memorial address to the Smithsonian Institution, the bolometer was described as being able to detect the presence of a cow in a field—solely by the heat it radiated—at a distance of ¼ mile [34].

1.1.4. Photodiodes

The first description of photodiodes was not in a journal article or addressed to a scientific society, but was first described in United States Patent 2,402,662 by R. S. Ohl of Bell Telephone Laboratories in 1946. Initially described as a *Photo E. M. F. Cell*, it was discovered while developing a process for purifying silicon ingots for use in point contact rectifiers. In some ingots, impurities rose to the top of the melts that created a p-n junction using only whatever impurities were present in the silicon raw material [35].

> "In a small proportion of the melts, say 3–5 per cent, the top of the melt was covered with material which was extruded from the interior

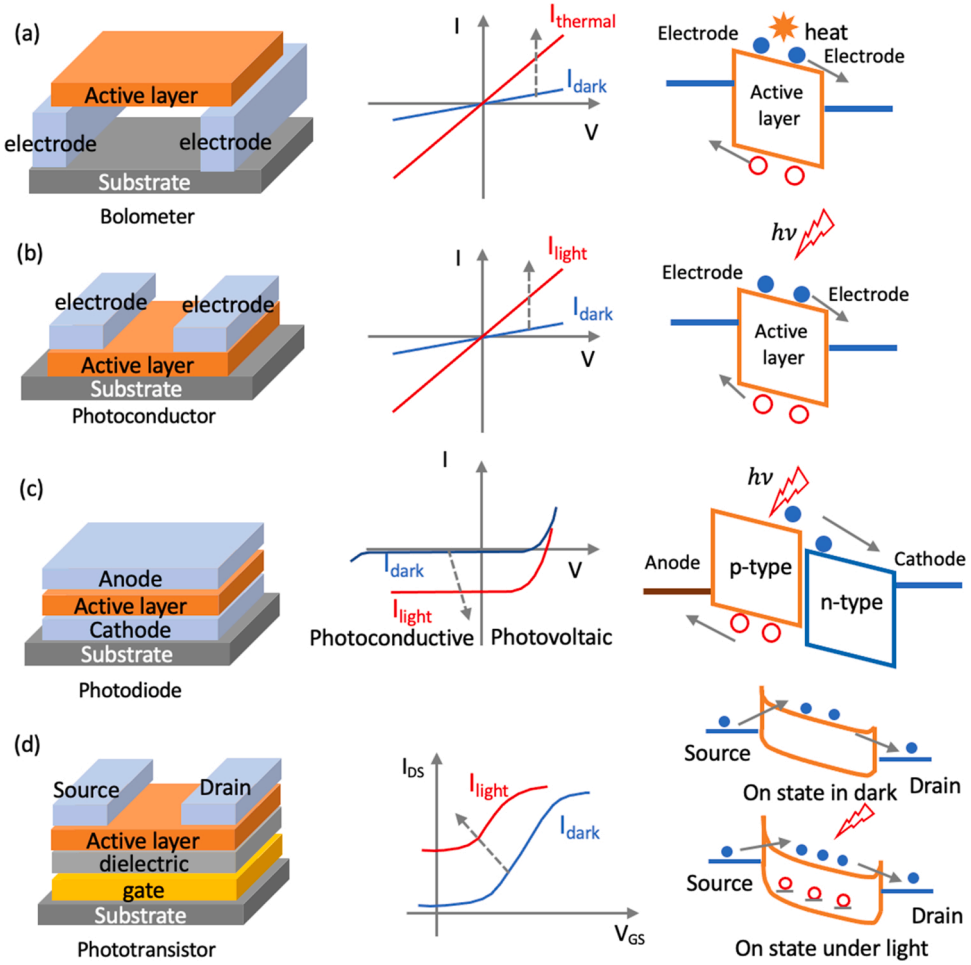

Fig. 2. Structures, current-voltage characteristics, and band diagrams for (a) bolometer, (b) photoconductor, (c) photodiode and (d) phototransistor. The phototransistor is depicted as an n-type device, but p-type is also readily available.

during the cooling process. The top surfaces of some such Ingots had a pale yellowish and greenish fluorescent appearance. It was discovered […] that if a contact were made to the top surface of such an ingot and some other point of the ingot, an electric current would flow if the top of the ingot were irradiated with infra-red or visible light."

The original description of this device—*Photo E. M. F. Cell*—cleanly describes how a photodiode operates. The junction of a p-type and n-type material generates a depletion region where incident photons can be absorbed. The detector generates an electromotive force (E.M.F.) upon absorption of light: a photovoltage. Alternatively, photocurrent can be measured.

1.1.5. *Phototransistors*

The phototransistor was developed just three years after the photodiode in 1949 by J. N. Shive of Bell Telephone Laboratories [36]. His goal was to utilize "a photo-conductive property of germanium which combines high spatial resolving power with an over-all quantum efficiency greater than unity." He modified the double surface transistor geometry common at the time so that when the side opposite the collector electrode absorbed light, it ejected charge carriers.

"A double surface transistor can be envisioned as a square cut from a germanium crystal, with the collector electrode on one of the polished sides. Source and drain electrodes are deposited opposite each other across its thickness. Light up to 1.5 μm was incident opposite the collector, producing a gain between 3–4."

1.1.6. *Materials development*

Over time, the materials used for each of these detectors improved their performance. Today, the selenium Clark and Smith used in their first photoconductor has been replaced with lead salts [37], mercury-cadmium-telluride (MCT) [38] and indium antimonide (InSb) [39]. Bolometers have improved from the iron rods initially used by Langley to materials with strong insulator-semiconductor transitions such as vanadium dioxide [40]. Photodiodes have improved from the helpful impurities in the occasional silicon ingot described by Ohl to epitaxial gallium arsenide (GaAs) [41], InSb [42], MCT [43], and superlattices [44]. Gone are the days of Shive's germanium phototransistors for IR detection; today, heterogeneous integration with silicon-based complementary metal oxide (CMOS) transistors are common [3].

There is currently a third generation of improvements occurring in all of these detector technologies that revolves around lower overall cost, higher operating temperatures, and easier fabrication processes. Most of the materials described above, especially for photoconductors and photodiodes, only work at cryogenic temperatures and are typically epitaxially grown, single crystals. A new class of materials that are solution processable, such as low-dimensional colloidal semiconductors and conjugated polymers, are being developed for the next wave of improvements to these IR detector technologies.

The key feature of these materials—their ability to be deposited from solution at low processing temperature (< 400 °C) —results in fundamentally different active layer structures. The thin films formed at low temperature tend to be disordered, which contrast with crystalline structures in the more traditional vacuum-processed inorganic materials

grown at high temperature. Semiconductors can be put into one of three different classes depending on their amount of long-range atomic order: single crystal, polycrystalline, and amorphous. Single crystal materials consist of an ordered atomic lattice extending over large distances. A polycrystalline material consists of a disordered network of small, highly organized crystal lattices. This can be commonly found in films deposited using physical deposition techniques like high temperature reactive sputtering [45]. The amorphous materials have no long range ordering of atoms; most solution-processable materials fall into the amorphous category. For example, in a spin-coated film, most of the solvent evaporates within the first ten seconds after the substrate begins rotating, effectively setting the polymer chains in random orientations upon drying. Nonetheless, conjugated polymer films can be processed to increase local ordering by mechanisms such as π-stacking and solution shearing [46–48].

The amorphous structure of these films imparts properties not typically found in ordered semiconductors, such as bias stress and differences in electronic conduction mechanisms. Bias stress occurs in amorphous semiconductors because they typically have a very large amount of shallow and deep charge carrier traps [49–51]. As trap sites become filled, the device current changes for the same bias level. This can impart a pronounced hysteresis to current-voltage curves [52]. Because the materials are amorphous, charge carriers cannot drift over long ranges in valence and conduction bands, but rather use a charge hopping mechanism [53]. This has the consequence of significantly depressing charge carrier mobilities [54], although mobilities can be increased for polymers deposited using vapor phase techniques [55]. Current research efforts are targeted at understanding and mitigating these drawbacks so that low-temperature disordered materials can enable high-performance detectors scalable to large areas and with improved mechanical properties and novel form factors.

2. Structures and physics of photon detectors

IR detectors are categorized into thermal or photon detectors [56]. Thermal detectors [5,57] such as bolometers and pyroelectrics are based on the transduction of heat into electrical changes and are broadband by nature. Their thermal response spectrum is not limited by the bandgap of the active material, while the response speed is usually well below 1 kHz due to the slow establishment of thermal equilibrium between the device and the environment. Photon detectors [1,12,24], on the other hand, absorb the incident photons and convert them into conducting charges in the semiconducting material, enabling a fast response up to hundreds of MHz. In this review, we will focus on photon detectors and the new generation of photonic optoelectronic materials that are compatible with solution processing techniques. In photodetectors, the transduction of absorbed photons to an electrical current occurs through (1) charge generation, (2) transport, and (3) collection. This section will discuss the device physics of these three steps and the operating principles of different detector structures to examine exciton and carrier dynamics and the effects of charge injection and recombination on device gain and efficiency.

A bolometer is basically a thermal resistor. The resistance of the active channel is sensitive to IR signals that induce a change in temperature. As shown in Fig. 2a, the structure for a bolometer is similar to a photoconductor (Fig. 2b), but often with an architecture that thermally isolates the active material from the substrate. A photoconductor is based on the photoconductive effect where photon-induced charge carriers change the channel conductivity. The increase in photon-induced current in the channel serves as the readout as shown in Fig. 2b.

A photodiode relies on p-type/n-type heterojunctions. The charge generation process is closely related to the interface at the junction. The typical current-voltage characteristics are presented in Fig. 2c. When a reverse bias is applied, a photodiode operates in photoconductive mode, and its photocurrent scales with light intensity. When a photodiode is at zero external bias, it is in photovoltaic mode, and its photocurrent is driven by the built-in potential at the heterojunction, the same operational mechanism as a solar cell.

A transistor is basically a variable resistor adjustable by a gate voltage. For phototransistors, the photon-induced carriers in the transistor channel lead to conductivity changes, and thus the channel current and threshold voltage change accordingly. The photoconductive gain and noise level in a phototransistor is readily modulated by applying a gate voltage. The structure in Fig. 2d is a lateral configuration, but it is worth noting that, while the most common transistor geometry is as shown with lateral contacts, there are demonstrations of vertical transistors that allow higher channel current, with a trade-off in the device off current [15,58].

2.1. Charge generation

2.1.1. Single component

Inorganic and organic semiconducting materials differ in the generation of charge carriers upon photoexcitation. Optical excitation of inorganic semiconductors produces Wannier-Mott excitons, and the typically high dielectric constants effectively shield the Coulomb attraction between the electron-hole pairs. Hence, thermal energy at room temperature is sufficient for the dissociation of free charge carriers [59]. In contrast, the weak intermolecular interactions and strong electron-phonon coupling due to lattice interactions in π-conjugated molecules result in lower dielectric constants and result in the formation of Frenkel excitons with more localized electronic wavefunctions. The excitons, i.e., electron-hole pairs, generated upon light absorption are bound by the exciton binding energy $E_B = q^2/(4\pi\varepsilon_0\varepsilon_r a)$, where q is the elementary charge, ε_0 is the permittivity of vacuum, ε_r is the dielectric constant and a is the electron–hole pair delocalization distance. The exciton binding energy varies from a few mV in inorganic materials to hundreds of mV in organic films with small polarizability and low dielectric constants. Large binding energies inhibit exciton dissociation into free electrons and holes, which becomes progressively more difficult in organic infrared materials as the bandgap narrows and the probability of recombination increases [60,61].

Fig. 3a illustrates the charge generation process in a thin film of a single organic semiconductor [62]. S_1 and S_n represent excitons at the first excited state and at a higher excited state, respectively. CP is the charge pair state and CP_F is the charge pair state decreased in energy under an applied electric field. Upon light absorption, singlet excitons (S_1 or S_n depending on the photon energy) are generated as depicted by arrows denoted (1) and (2). Charge generation from a thermalized S_1 state may happen through process (3), leading to a charge pair (CP_F) that dissociates into free carriers aided by the applied field. Curly arrows (4) indicate the relaxation of excitons from higher energy states, which either generates a charge pair (CP) or results in a vibrationally hot S_1 state. The vibrationally hot S_1 state from process (4) could also overcome the charge separation barrier to generate CPs through process (5).

2.1.2. Heterojunction

To enhance charge generation in solution-processed semiconductors, heterojunctions comprised of multiple semiconductors are used to facilitate charge separation [7,11,63,64], as schematically depicted in Fig. 3b. In solution-processable semiconducting systems, the terminology often refers to a p-type material as the donor, while an n-type material is the acceptor. In this review, we use the terms “donor” and “acceptor” to describe the PN heterojunction. At the donor-acceptor interface, the energy offset between the highest occupied molecular orbital (HOMO) of the donor and lowest unoccupied molecular orbital (LUMO) of the acceptor is known as the charge-transfer (CT) state. The CT state extends the delocalization distance (a) and reduces the binding energy E_B of the electron-hole pair, leading to more efficient dissociation and charge generation. In Fig. 3c and d, the detailed energy diagram presents the possible charge-transfer pathways upon photoexcitation [64]. The absorption of a photon with energy higher than E_{D^*} results in

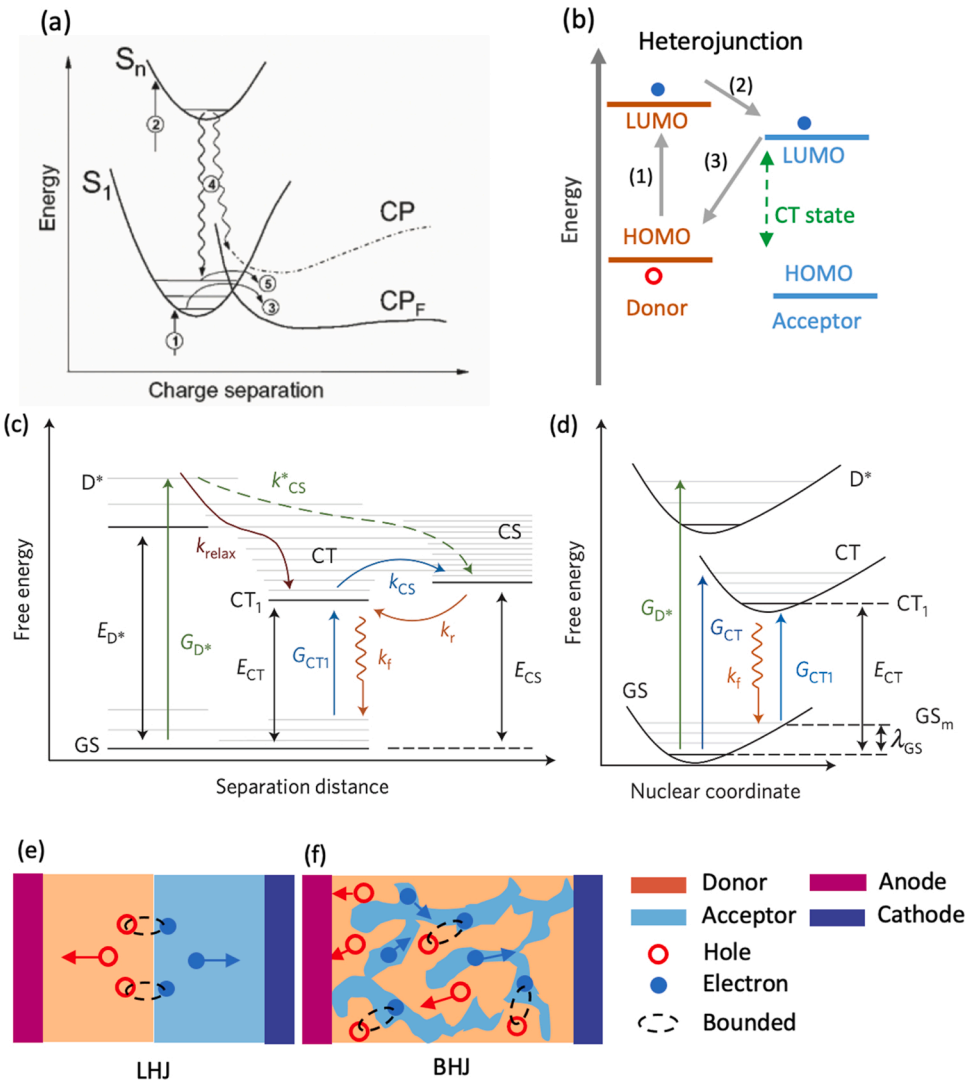

Fig. 3. (a) Charge photogeneration process in a single material. S1 and Sn represent excitons. CP is the charge pair state, and CP_F is the charge pair state decreased in energy under an applied electric field. Reproduced with permission of Ref. [62](b) Simplified energy diagram of a heterojunction. CT is the charge-transfer state. Process (1) is light absorption; process (2) is charge transfer and dissociation; process (3) is charge recombination. (c) Detailed state diagram and (d) coordinate energy level diagram of a heterojunction to show the charge generation and recombination processes upon photoexcitation. Reproduced with permission of Ref. [64]. Schematics comparing charge generation and transport in (e) layered heterojunction and (f) bulk heterojunction.

an excited electron in state $D_{excited^*}$ generated at a rate of G_{D^*}. When the excited electron in the donor is transferred to the acceptor, the CT state is formed. The CT state can either decay to the ground state (GS) radiatively (k_f), or produce a charge-separated state (CS) i.e., free carriers to be collected at the electrodes. Excess photon energy may assist free charge generation at a rate of k^*_{CS}.

The relaxed CT state, CT_1, is sometimes lower in energy than CS states, potentially hindering the generation of free carriers. In the case that the relaxation rate to CT_1 (k_{relax}) is much faster than charge separation through higher energy states (k^*_{CS}), the free carrier yield becomes dependent on the competition between dissociation (k_{CS}) and recombination (k_f), and independent of the photon energy. Meanwhile, it has been shown that a high yield of free carriers from CT_1 is possible in organic systems working in the visible, if the recombination rate k_r is minimized.

Typically, there are two types of heterojunction channels, layered heterojunction (LHJ) and bulk heterojunction (BHJ). A LHJ is composed of two or more layers of different materials, where the interface between the layers forms a type-II heterojunction [65–67] with staggered energy offsets, making it favorable for excitons to dissociate into free carriers as shown in Fig. 3e. As exciton separation occurs at the interface, increasing the interfacial area is beneficial to enhance carrier generation. Thus, the concept of a BHJ (Fig. 3f) was introduced in which the donor and acceptor semiconductors are intermixed throughout the film to produce a much larger interface than in a LHJ. A BHJ film is easily made with solution-processed semiconductors by blending all the components in one solution and then depositing the mixture to form the active layer. Different BHJ compositions include binary [6] and ternary blends [68] and films with inorganic nanocrystals embedded in organic matrices [69]. Particularly for organic semiconductors, charge generation is far more efficient in BHJs than in single-component films. In this review, we use the term BHJ to describe a solution-processable system that comprises two or more semiconducting materials in the mixed active layer, including quantum dots, perovskites, low dimensional semiconductors, and organics.

However, even BHJs have been limited by poor exciton dissociation efficiency in IR materials because of the high non-radiative recombination at narrow bandgaps [61]. Operating the device with an external bias assists exciton dissociation and charge generation, albeit often with the trade-off of increasing the dark current noise. Recently, in BHJ systems with non-fullerene acceptors, charge generation has been shown to be efficient for minimal energetic offsets, much smaller than those required for fullerene-based systems [70–74]. This property facilitates photodiodes that operate in photovoltaic mode at zero bias and avoids dark current injection from an external bias [61,75]. Another approach to increase charge generation is by incorporating high permittivity components into the BHJ film. Raising the material permittivity (i.e. the dielectric constant ε_r) increases the polarizability, which screens Coulombic interactions between the electron-hole pairs and lowers the exciton binding energy [76–78].

2.2. Charge transport

2.2.1. Single layer channel

After the charge generation step, the free carriers are transported across the active layer, producing a photocurrent under the built-in or external bias. Charge transport in solution-processed materials tends to be encumbered by disorder within the film. Due to the energetic disorder in available states, the motion of a carrier is typically described by hopping [79–81], which is a phonon-assisted tunneling mechanism for carriers to travel from site to site (Fig. 4a, b). This multiple trapping-and-release characteristic manifests as thermally activated transport, where the mobility in the disordered semiconductor increases with temperature. This stands in contrast to transport within crystalline semiconductors that shows decreasing mobility with higher temperature. The trapping-and-release transport in disordered materials introduces time dependent hysteresis and also slows carrier mobility.

To improve the detector performance, efforts have been devoted to improving the charge mobility in the transport channel. For example, a planer structure is favorable [82] for molecular packing, which can be tuned to optimize the π-π stacking. In organic semiconductors, linear orientation and close packing of conjugated polymer backbones favor intermolecular transport and boost the photoresponse [82,83]. In films of colloidal quantum dots, the conductance is improved by shortening or removing the surface ligands, because long ligands may block the charge transport between the nanocrystals [84,85]. Ligand exchange, sintering, or cross-linking are effective processing methods to improve charge transport in nanocrystalline films [84–86].

2.2.2. Heterojunction channel

2.2.2.1. Layered heterojunction. Instead of a single-component active layer, layered heterojunctions can be used to separate the charge generation and transport processes. For example, in CQD detectors, the photoresponse efficiency is limited by low carrier mobility in the CQD film. To address this bottleneck, materials with high carrier mobility such as oxides and two-dimensional semiconductors are placed next to CQDs to form heterojunction channels. Fig. 4c gives an example of CQD/graphene channel [87]. The CQDs are responsible for carrier generation, and then the free carriers diffuse into the high-mobility material that serves as the charge transport pathway and improves the transport efficiency. However, it should be noted that high conductivity of the detector channel can lead to high dark current, which reduce the ability to detect weak light.

2.2.2.2. Bulk heterojunction. In organic IR detectors, the BHJ active layer plays two roles, one is to enhance exciton separation at the donor-acceptor interface, and the second is to facilitate charge transport by forming separate pathways for electrons and holes to travel to their respective collection electrodes. As shown in Fig. 3e, a BHJ of percolating donor-acceptor network allows electrons (holes) to travel in n-type (p-type) domains [88–90], but this percolating configuration shows lower diode rectification compared to a LHJ. The anode and cathode are accessible by both donor and accepter materials in the percolating BHJ, while each electrode in the LHJ is connected to only one type of semiconductor to suppress charge injection and dark current. To keep the advantages associated with the large interfacial areas, while also optimizing rectification, the BHJ morphology is modified by phase segregation [91]. The distribution of donor and acceptor domains can be tuned by surface treatments and solvent evaporation control, such that the surface energy of the electrode would favor one component over the other to induce segregation in the donor-acceptor blend [92]. A layer-by-layer deposition process induces phase segregation by leveraging different solubilities of donor and acceptor in the solvent [93]. Overall, phase segregation is helpful to reduce biomolecular recombination [94] and improve transport in BHJs.

2.3. Charge collection

After charge generation and transport, charge collection is the last step in the process of transducing light into an electrical current. Charge collection is heavily dependent on the properties of the interface between the semiconductor and electrodes. The contact regions essentially dictate whether the device operates as a rectifying diode or other resistive types. The energy levels of contacts are adjusted to efficiently collect photogenerated charges before they are lost to recombination; or taking a step further, the contacts can be engineered to promote charge

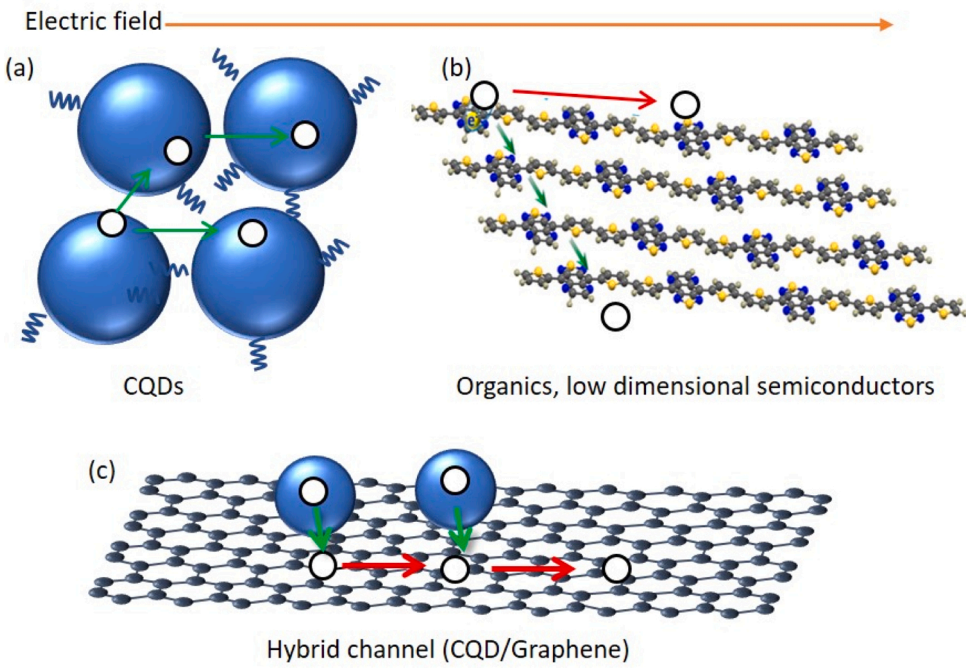

Fig. 4. Schematics showing the charge transport through (a) the CQD film, (b) the organic film and (c) the hybrid channel (CQDs/graphene). The circles represent charge carriers. The green arrow represents intermolecular charge transfer while the red arrow represents intramolecular transfer.

injection that creates photomultiplicative gain. Meanwhile, the dark current characteristics of a detector are also influenced by the contact injection barrier [95,96], affecting metrics such as the signal-to-noise ratio and the detection limit.

2.3.1. Contacts in photodiodes versus photoconductors/phototransistors

The different current-voltage characteristics between solution-processed photodiodes and photoconductors originate from rectifying or ohmic interfaces. Photodiodes with rectifying interfaces are fabricated with PN heterojunctions, or metal-semiconductor Schottky junctions. Asymmetric electrodes, donor-acceptor heterojunctions, and charge selective transporting layers are usually used in photodiodes featuring rectified current-voltage characteristics. While in photoconductors, symmetric electrodes with same work-functions are often used to collect charges, and the current-voltage curve is symmetric. Thus, the difference between photodiode and photoconductor is a combination of interfaces and contacts. We often depict different photonic device types according to the geometries in Fig. 2, where photodiodes have vertically stacked electrodes while photoconductors/transistors use lateral electrodes [11,97]. However, it is worth noting that lateral diodes and vertical photoconductors are possible though not common, and conversely vertical phototransistors have been demonstrated [15].

In photodiodes, the contacts consist of materials with different work functions [1,13,98,99]. Each electrode preferentially collects or injects one type of carrier (electron or hole), and therefore leads to the rectifying behavior characteristic of diodes. The energy level difference between the p-type and n-type semiconductor and work function difference in electrodes establish a built-in voltage [98,100], which enables device operation without an external bias in photovoltaic mode. The photodiodes can also operate in the photoconductive mode under a reverse bias. The external electric field assists charge separation and transport in photodiodes to improve the quantum efficiency.

In photoconductors and phototransistors, the contacts are typically made of the same material patterned side by side. These devices require an external bias to operate. An ohmic contact between the electrode and the active channel is preferred for charge collection. Nonetheless, surface states present at the semiconductor or mismatch in work functions at the active layer-electrode junction might lead to a Schottky barrier, which is sometimes leveraged to suppress dark current [95,96,101].

The structure of a phototransistor is basically a photoconductor with an additional gate electrode, which modulates the carrier density at the active channel-dielectric interface by field effect, thus controlling charge transport and collection in the detector. The phototransistor can deliver a large current in accumulation mode, or output a small current with very low noise in depletion mode. In accumulation mode, the transistor is in the on state with conducting charges attracted to the channel/dielectric interface. The charge generation upon light illumination results in more carriers in the channel and leads to a shift in the transistor threshold voltage and an increase in photocurrent. However, the high channel conductance produces a large background dark current, limiting the signal-to-noise ratio. In depletion mode, the conductivity of the channel is very low. The photogenerated charges significantly increase the charge density and channel conductivity, giving rise to a very high on/off ratio. Recent reviews that provide more detail related to phototransistors can be found in references [4,11,102].

2.3.2. Charge blocking layers

Charge blocking layers are materials that preferentially conduct one type of charge; for example, electron blocking layers will be mainly hole conductors and vice versa. An electron blocking layer is equivalent to a hole transporting layer. The energy levels of charge blocking layers are carefully selected for photodiodes to suppress dark current noise. In addition, by engineering the contact interfaces to control charge collection and injection, photomultiplication effects can be promoted to increase device efficiency. This section will discuss how charge injection barriers affect dark current and photocurrent gain.

2.3.2.1. Effect of charge blocking layers on the reduction of noise current.

Low background noise is crucial to enable high signal-to-noise measurements, and under an applied bias, charge injection would increase the dark current noise. Strategies to lower charge injection are shown in Fig. 5. In solution-processable IR detectors, a BHJ active layer has been used to enhance charge separation upon photon absorption on account of the increased interfacial area and improved charge transport in segregated pathways. However, in a percolating bicontinuous network where both donors and acceptors are in contact with the electrodes (Fig. 5a) [88,89], the injection barrier is low, resulting in high dark leakage current at reverse bias [103]. Separating the donor and acceptor materials to form LHJ would suppress charge injection. However, the LHJ configuration shows low exciton dissociation efficiency due to the limited interfacial area between donors and acceptors. To optimize dissociation while minimizing dark current, the BHJ film morphology have been adjusted to manifest phase segregation, namely, a distribution of donor and acceptor domains. The segregated BHJ can be formed by a layer-by-layer solution processing procedure, where the donor and acceptor materials are intermingled in the bulk but not mixed at the electrodes as shown in Fig. 5b. In this phase-segregated morphology, large interfacial area are retained to facilitate exciton dissocation, while each electrode is mostly in contact with the semiconductor that presents a high injection barrier, thereby reducing charge injection in the dark [93].

In addition to phase segregation, a general way to reduce charge injection is by incorporating charge blocking layers at the contacts (Fig. 5c) [104]. Proper use of charge blocking layers has been shown to reduce dark current by several orders of magnitude, when comparing devices using the same active layer [89,105]. The requirements for effective charge blocking layers are: (1) proper energy level alignment with respect to the donor and acceptor materials, (2) uniform morphology to avoid direct contact between the electrodes and the active layer, and (3) good charge mobility and efficient carrier transfer to the electrodes. The interlayers not only reduce the dark current injection, but also facilitate photogenerated charge collection under light, which promotes the photoresponse [106]. For anodes, one of the most frequently used interlayer is poly(3,4-ethylenedioxythiophene) polystyrene sulfonate (PEDOT:PSS), which has high optical transparency and high conductivity. However, the PEDOT:PSS is not a good electron blocking layer. Alternatively, other electron blocking materials such as poly(N,N'-bis-4-butylphenyl-N,N'-bisphenyl)benzidine (Poly-TPD) [89] and copper(I) thiocyanate (CuSCN) [106] are shown to be suitable for minimizing electron injection while allowing hole extraction. For cathodes, hole blocking layers such as ZnO are routinely used to block hole injection under an external bias [107,108]. By adding a thin polyethylenimine (PEIE) layer to modify the zinc oxide (ZnO) surface, the device dark current is further reduced by the interface dipoles that build up a barrier to hole injection [98,108,109]. On the other hand, the charge blocking layers are non-crystalline semiconductors, and they often have states near the conduction/valence band edges, resulting in lower injection barrier than expected from the conduction/valence energy levels (Fig. 5c, bottom right diagram). Additional mid-gap states would allow Schottky-Hall-Read recombination and degrade the charge blocking function [110]. Charge injection into the states near the band edge of the disordered semiconductors is shown in Fig. 5c, top right diagram. States near the bandtail extend into the effective bandgap in highly disordered semiconductors, which reduce the barrier to charge injection especially in low bandgap detection systems. Factors contributing to dark current require future studies, but there are promising trends that dark current can be reduced using materials with low density of trap states near the band edges, for example in non-fullerene acceptors [75].

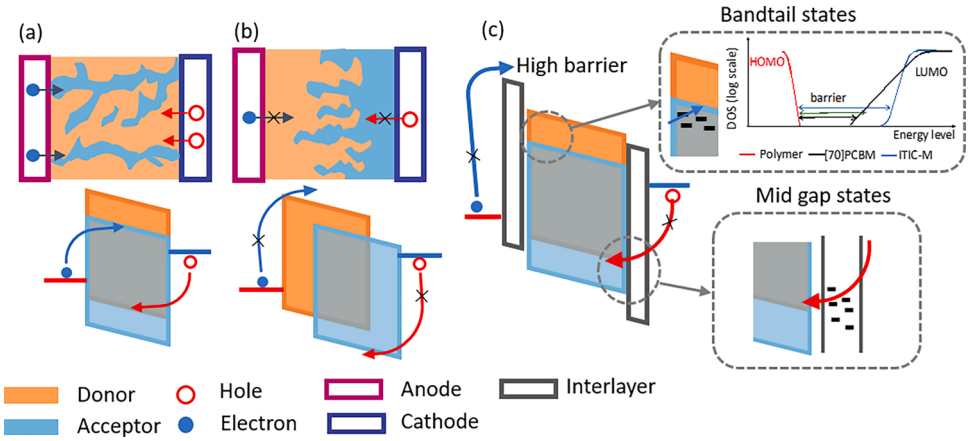

Fig. 5. The schematics showing charge injection process at different interfaces, comparing BHJs (a) with percolating networks and (b) with phase segregation. (c) BHJ with blocking layers. Dark current injection can be suppressed by inducing phase segregation and inserting blocking layers. However, mid-gap states and states near the band edges contribute to additional charge injection that increases dark current.

2.3.2.2. Effect of charge blocking layers on photomultiplicative gain. A typical photo-transduction process converts one photon to one electron-hole pair, and the photon-to-electron conversion efficiency will be at best 100 % if there is no recombination loss. However, the conversion efficiency can be raised above 100 % by using photomultiplicative mechanisms that manipulate charge injection from contacts. In this section, we introduce methods to generate photomultiplicative gain in IR detectors. Below we use the terms photoconductive gain and photomultiplicative gain interchangeably. Photomultiplication occurs when one absorbed photon triggers multiple charges to circulate across the device channel as illustrated in Fig. 6. Upon the photogeneration of an electron-hole pair, one charge (majority) is mobile and can circulate many times before recombination, while the other charge type (minority) is vulnerable to become trapped. To offset the charge imbalance due to trapped charges, mobile charges are injected into the device channel, producing a gain (G) in the photocurrent as expressed below: [111,112]

$$G = \tau_c/\tau_t, \text{ with } \tau_t = L^2/(\mu_c \times V), \quad (1)$$

Where τ_c is the minority carrier lifetime, τ_t is the transit time of majority carrier, L is the channel length, μ_c is the majority carrier mobility, and V is the applied voltage. When the transit time of circulating mobile charges is shorter than the trap lifetime, multiple carriers are collected by the external circuit leading to G over 1, and the photomultiplication continues until trap recombination occurs.

To induce photomultiplication, the channel-contact interface are

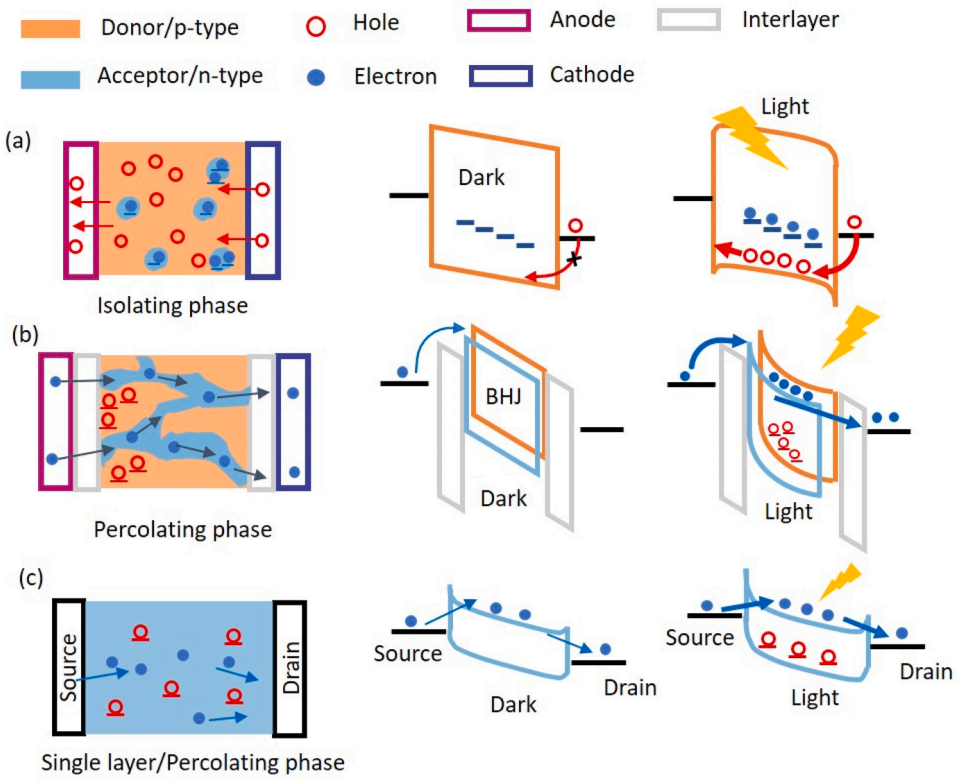

Fig. 6. Schematics to illustrate gain mechanisms due to trap-assisted barrier lowering. Traps states are indicated by the short bars. (a) Photomultiplication in a BHJ with excess donor compared to acceptor. (b) Photomultiplication through injection barrier lowering. (c) Gain in phototransistor where the uncollected trapped charges effectively increased the gate bias.

Table 2
Summary of detector metrics.

Metric	Unit	Defination
Responsivity (R)	A/W	Photocurrent over incident light power at a specific wavelength.
External quantum efficiency (EQE)	%	Ratio between the number of charge carriers collected by the detector and the number of photons of a given energy incident on the device's surface.
Noise equivalent power (NEP)	$W/Hz^{0.5}$	Incident light power that generates a signal-to-noise ratio of 1 in a 1 Hz bandwidth.
Specific detectivity (D^*)	$cm\ Hz^{0.5}\ W^{-1}$ (Jones)	Reciprocal of NEP, normalized to the square root of the detector area and the measurement bandwidth.
Dynamic range	dB	Range of incident optical powers that the detector responds to.
−3 dB bandwidth	Hz	Frequency at which the signal's power spectral density is half of its maximum value.
Gain (G)	Unitless	Ratio bewteen the number of collected carriers and the number of photons absorbed by the detector.

modified to optimize trap sites [19,113] or charge blocking layers [114]. Upon light illumination, the minority charges accumulate and lower the tunneling barrier for majority carrier injection to produce gain. For example, by manipulating the donor:acceptor ratio (e.g., 100:1) in the BHJ layer, a small ratio of acceptors forms isolated domains that act as electron traps as shown in Fig. 6a. Charge injection is prohibited in the dark due to the interface barrier, but under light illumination, photogenerated electrons tend to be trapped in the acceptor domains due to the lack of a continuous transport path. The accumulation of electrons causes band bending to lower the hole injection barrier at the cathode interface [18], enabling multiple holes to be injected per photon absorbed. This gain mechanism depends on the formation of interface traps for minority carriers and on the high mobility of majority carriers in the active layer. The mechanism is not limited to organic semiconductors, and the device design is generally applicable to other soluble processed semiconductors [18,20,115].

In addition to manipulating the trap sites in the BHJ active layer, the interface control is another way to realize PM detection. By tuning the charge blocking layers and selectively block holes at the interface, the accumulated holes at the interface leads to band bending, which facilitates multiple electron injection and collection, as schematically shown in Fig. 6b. This concept utilizes charge blocking layers to confine carriers at the interface. The two blocking layers allow one type of carrier to recirculate in the device under bias until they recombine with the opposite charge [114]. The dark current is a concern because the charge injection happens at high bias, which reduces the detectivity. Besides being induced in diodes, photomultiplication is often observed in phototransistor structures (Fig. 6c), in which charge traps serve as an additional gate bias to increase charge injection and recirculation leading to a photocurrent gain [116,117].

The PM detectors enable sensitive photodetection by providing photoconductive gain. The built-in gain mechanism avoids the incorporation of pre-amplifiers, which is promising for miniaturized sensing and imaging systems. However, there are some concerns regarding the PM detectors, i.e., the dark noise current and photoresponse speed. Due to the gain-bandwidth product limit, high gain detection systems usually suffer slow response, and more studies are needed to understand the trade-off.

3. Metrics for detectors

A photon detector is commonly described by metrics including responsivity (R), external quantum efficiency (EQE), noise equivalent photocurrent (NEP), specific detectivity (D^*), dynamic range, and response bandwidth. Table 2 summarizes the key parameters and their units and definitions.

Responsivity describes the electrical photocurrent I_{photo} generated per watt of incident optical power P. Each photon of a given wavelength is converted to charge carriers at a certain efficiency.

$$R = \frac{I_{photo}}{P} \tag{2}$$

External quantum efficiency describes how efficient a photodetector is at converting photons to a measured photocurrent. It is closely related to the responsivity:

$$EQE = \frac{R(hc)}{\lambda q} \tag{3}$$

Where h is the Planck constant, c is the speed of light, and q is the electric charge, and λ is the wavelength of incident light.

The above equations describe the photosignal. The detector noise in the dark is influential to the sensor performance, because the noise characteristics set the limit on the lowest detectable input. Noise is classified by origins, labeled as shot noise (i_{shot}), Johnson-Nyquist thermal noise ($i_{thermal}$), flicker noise or 1/f noise ($i_{1/f}$), and generation-recombination noise. When the detector is being reverse biased, shot noise often dominates the total noise in photodetectors, but the noise spectra must be measured [61,118] to avoid an under-estimation of the total noise, especially in IR detection systems operating in photovoltaic mode at zero bias, because of the high thermal noise in narrow bandgap semiconductors. Johnson-Nyquist thermal noise arises from thermal generation of carriers across the material bandgap. In considering overall thermal noise, it can be a combination of Johnson-Nyquist noise internal to the device and external fluctuations in the background temperature. Flicker noise is a type of electronic noise with a 1/f power spectral density and thus is often referred to as 1/f noise. It is the dominant noise source at low frequencies in most of the detectors, originating from the impurities in the semiconductors giving rise to the trapping and detrapping of carriers [105,119], or from generation/recombination events [118]. It should be noted that the total noise (i_{total}) includes all noise sources as described by

$$i_{total} = \sqrt{i_{shot}^2 + i_{thermal}^2 + i_{1/f}^2} = \sqrt{2qi_{dark}\Delta f + 4k_B T\Delta f \Big/ R_{sh} + i_{1/f}^2} \tag{4}$$

Where i_{dark} is dark current, Δf is the measurement bandwidth, k_B is the Boltzmann constant, T is the absolute temperature, and R_{sh} is the shunt resistance of the photodetector. Some of the noise reduction approaches have been discussed in prior Section 2.3.2.

The noise equivalent power is the incident light power that generates a signal-to-noise ratio (SNR) of one in a 1 Hz measurement bandwidth. It is equivalent to the ratio of a photoconductor's noise current (I_{noise}) in the dark to its responsivity, as denoted by Eq. 5. For a photon to be detected, the incident optical power must be above the NEP, so that the optical power generates a SNR of >1. A lower NEP value indicates a more sensitive detector, as it is capable of responding to a lower level of light power.

$$NEP = \frac{I_{noise}}{R} \tag{5}$$

Specific detectivity is a figure of merit that allows photodetectors to be compared to each other regardless of operating mechanism and active area. It is roughly the inverse of NEP and is a case where "bigger is better" in the sense that a higher value of D^* describes a more efficient photodetector (Eq. 6), where A_d is the detector active area:

$$D^* = \frac{\sqrt{A_d \Delta f}}{NEP} \quad (6)$$

The detector dynamic range represents the range where the sensor signal changes in response to the incident light, in term of the orders of magnitude from the minimum to the maximum inputs. If the photocurrent scales linearly with incident light power, the linear dynamic range (*LDR*) can be expressed logarithmically in decibels as in Eq. 7 [1].

$$LDR = 10\log(\phi_{max}/\phi_{min}) \quad (7)$$

Where the ϕ_{max} and ϕ_{min} represent the input irradiances between which the photodetector response is linear. If the irradiance unit is in power, the constant in Eq. 7 is 10, and if the irradiance unit is in voltage or current, the constant is 20, as based on the decibel definition. The dynamic range is limited by the dark current noise for the minimum irradiance, while at high irradiance the increased density of photogenerated charges leads to recombination and current saturation [105, 118]. It worth noting that due to recombination, devices with photoconductive gain such as phototransistors usually have a sublinear responsivity to irradiance (decreasing gain or *EQE* with increasing irradiance), whereas devices without gain often exhibit linear responsivity (constant gain or *EQE* over the entire dynamic range). Nonetheless, phototransistors tend to show a wider dynamic range than photodiodes (Fig. 7a), as the gain mechanism increases signals relative to the noise level and the sublinear behavior extends the response range before reaching saturation [112].

The response time of a photodetector dictates the refresh rate and can be characterized by the rise and fall times or the -3 dB bandwidth. The rise (or fall) time is defined as the time interval for the photocurrent to rise from 10 % to 90 % (or from 90 % to 10 %) of its maximum amplitude. The electronic bandwidth is the frequency at which the amplitude decreases by -3 dB. The frequency bandwidth of a detector is closely related to factors including the charge mobility, charge carrier lifetime, detector mechanism, and the circuit resistance-capacitance *RC* constant. The -3 dB bandwidth (*BW*) is estimated using [1,120,121]

$$BW^2 = \left(\frac{C}{2\pi t_{tr}}\right)^2 + \left(\frac{1}{2\pi RC}\right)^2 \quad (8)$$

Where t_{tr} represents the transit time and *C* is a constant typically equated to 3.5 as a factor of the root mean square (RMS) value related to the signal amplitude (for a triangular wave approximation, the peak-to-peak amplitude= $2\sqrt{3} \times$RMS = 3.5 × RMS).

The gain mechanisms in photodetectors may affect their response time. If the photo-multiplicative gain is induced by trap-assisted injection barrier lowering (Fig. 6) [122], there will be trade-offs between the device gain and speed. Minority carriers that remain in trap states would induce injection barrier lowering. For the period that charges stay in trap states, the circulation of injected charges would continue, thus increasing gain with longer trapped charge lifetime; but the slow release of minority carriers from traps constraints the detector to low frequency operations less than 40 Hz. For example, mercury telluride (HgTe) CQDs with larger diameters have more traps, which improves the device responsivity and gain but at a cost of the response speed [123–125]. On the other hand, if the gain mechanism is based on photovoltage that raises transconductance, for example at a trap-free rectifying Si-CQD junction [125], the device gain and response speed can be decoupled, and the transistor is shown to exhibit high gain (10^4) and fast response time (10 μs). A metric that simultaneously accounts for gain and speed characteristics is the gain-bandwidth product, which allows comparisons across different device types as shown in Fig. 7b, with the larger area indicating a better gain-bandwidth product.

4. Solution-processed infrared materials

Traditional infrared semiconductors such as III-V compounds and mercury cadmium telluride (HgCdTe) require high temperature growth and complex die-transfer processes that preclude monolithic integration with large-area readout circuits. The crystalline devices show high thermal noise and need cryogenic cooling that adds weight and costs to the detection system. To address the shortcomings of current infrared technologies, alternative materials are being developed to facilitate scalable fabrication and new form factors for infrared optoelectronics. Solution-processable semiconductors can be easily deposited over large areas as thin films, offering mechanical flexibility and room-temperature operation due to thermally activated transport in disordered thin films. Below, we present the four major categories of solution-processable semiconductors for IR detection. Given the authors' research expertise, this review covers the properties of organics in greater detail than other material categories; however, we aim to compare the key approaches for tuning properties. For example, the bandgap is mainly controlled by changing particle dimensions in CQDs, whereas it is adjusted by changing donor-acceptor units in organic semiconductors, or by manipulating elemental ratios in perovskites. Our discussions will start with zero-dimensional CQDs, then low dimensional materials including 1D carbon nanotubes and 2D nanosheets, and proceed to semiconductors that are not quantum confined, such as organics and perovskites with narrow bandgaps.

4.1. Zero dimensional nanocrystals

Colloidal nanocrystals, namely quantum dots including lead sulfide (PbS) and HgTe [126–128], can be synthesized from solution to tailor properties such as the bandgap and stability. For PbS, the particle diameter was tuned from 3.9 to 9.6 nm, leading to a photoresponse spanning the NIR to SWIR spectral regions (Fig. 8a). In a similar manner, the particle size of HgTe was adjusted to achieve a NIR to MWIR photoresponse from 3 to 5 μm. A hot-injection method was used to obtain

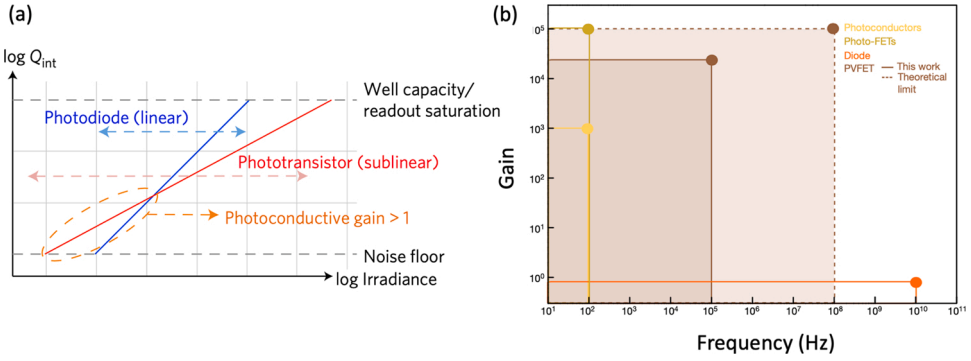

Fig. 7. (a) Comparing the responsivity and dynamic range of a photodiode and a phototransistor with gain. Reproduced with permission from Ref. [112]. (b) Gain vs bandwidth for a typical photoconductor (yellow), diode (orange), photo field-effect transistor (FET) (light brown), and photo-voltage FET (dark brown). All devices are based on CQD absorbers. Reproduced with permission from Ref. [125].

uniform CQDs with a tight distribution of particle sizes. Within the model of quenching by dipole coupling, the non-radiative lifetime scales as r^{-4}, where r represents the nanocrystal radius [85]. Thus, exciton lifetime is dependent on the nanocrystal size, and improving size homogeneity of the CQDs is advantageous to enhance the exciton lifetime.

By exploiting intra-band transitions, the photoresponse of PbS CQDs was extended to longer wavelengths up to 9 μm, which is beyond the intrinsic bandgap of bulk PbS [129,130]. Stable heavy doping is required in such intra-band absorption systems. When the confined ground state is populated with electrons, intra-band absorption within the conduction band may occur, in which the absorption is attributed to electronic excitation between energy levels smaller than the bandgap. For example, the photon energy absorbed through an intra-band transition can be as low as 0.14 eV, much smaller than the 0.41 eV bandgap of bulk PbS [130].

The properties of nanocrystals have been modulated by surface chemistry. The ligands attached to CQDs are used to prevent aggregation. The properties of the ligands, such as the end groups and alkyl chain lengths have a dramatic impact on the properties of the CQD films and impact trap states, conductivity and band structure that influence detector performance parameters such as gain and response speed [122, 131–133]. Ligand exchange processes on PbS CQDs of the same size led to shift in energy levels, as seen in Fig. 8b. Through judicious ligand selection, the stability of the CQDs was enhanced to over one year [69]. The performance characteristics of infrared devices using CQDs are summarized in Table 3.

The narrow bandgap interband transitions in CQD tend to require heavy elements, yet the heavy elements are toxic [134,135], particularly concerning when they need to be incorporated in health care and wearable electronics. Non-toxic CQDs for IR light sensing and imaging are under rapid progress, e.g., narrow bandgap III-V material (InAs [136–138], InSb [139]) based CQDs, silver chalcogenide CQDs [135, 140–142]. The III-V semiconducting CQDs are emerging, but with limited photoresponse up to SWIR [134,138]. Silver chalcogenide CQDs are another group of materials that show promise for IR detection [141], especially for MWIR photodetection [140,142]. The photodetection characteristics of silver chalcogenide CQD devices are sensitive to size [135], ligand, and synthesis temperature [142], which provides tunable photodetection to satisfy versatile requirements.

The IR photodetection enabled by colloidal materials is potentially very attractive for new generation IR sensing systems with versatile properties at low cost. These solution-processable materials are strong alternatives to their vacuum-processed counterparts, especially in flexible electronics, non-invasive fluorescence imaging applications [138]. Also, the much longer wavelength sensitivity in such colloidal materials renders them suitable for SWIR, MWIR or even LWIR photodetection. The interested readers are encouraged to find more details in review papers about QDs [8,134,143,144].

4.2. Low dimensional materials

Low dimensional materials, such as nanotubes [168] and nanosheets [5] have been employed in optoelectronic devices to detect light spanning the visible, IR, and terahertz regions. The bandgaps of atomically thin 2D materials, such as graphene, transition metal dichalcogenides and black phosphorus (structures shown in Fig. 8c) are sensitive to factors including layer number, strain level, and chemical doping [5]. For example, a strong photoresponse from 5 to 12 μm was realized in twisted bilayer graphene by adjusting the twist angle to form a superlattice [169]. In addition, the use of low dimensional nanomaterials for sensing long wave infrared radiation is enabled by their thermoelectric response at room temperature [170–172]. However, the response is usually slow, on account of the long time required to establish thermal equilibrium between the device and its environment.

Most low dimensional materials pose considerable difficulties when considering their solution processability. There are IR detectors based on solution processed platelets of 2D materials [170,173], but the charge transport is diminished when compared to films deposited by dry exfoliation. Another complication for detectors based on 2D materials is that light absorption is limited on account of their atomic scale thicknesses. Additional light absorbers, such as CQDs, organics, or perovskites, are often combined with high mobility 2D layers to form hybrid light detection channels [87]. With unique in-plane charge transport properties leading to high mobility, 2D materials are frequently used as charge collection channels. Additional charge injection into the high mobility 2D layer would give rise to ultrahigh gain in heterojunction photoconductors and phototransistors [174,175].

4.3. Organics

In contrast to inorganic semiconductors, soft-matter (organic and polymer) systems constitute a complex mixture of structural and energetic heterogeneities, which complicates rational design and leaves many open questions regarding control of the bandgap at low energies, interactions with IR light, and the study of fundamental physical phenomena necessary for the design and realization of new IR optoelectronic and device functionalities [176]. While the majority of organic semiconductors devices operate in the visible region of the electromagnetic spectrum, improvements in materials design are extending their utilization into the NIR-LWIR spectral regions [4,177]. Conjugated polymers (CPs) have become a leading materials platform in this context. While controlling the bandgaps of CPs at very low energies still remains a considerable challenge, design rules that connect chemical, electronic, and structural heterogeneities with the degree of electronic correlation and energetic disorder are emerging [178–180].

Various molecular engineering strategies have been applied to tune the bandgap of OSCs. Donor-acceptor (DA) CPs comprised of alternating electron-rich (donor) and electron-poor (acceptor) building blocks are now the dominant class of high-performance materials [6,181,182]. The combination of alternating donor (push) acceptor (pull) building blocks results in hybridization of molecular orbitals, HOMO and LUMO energy levels, and strong intramolecular charge transfer transitions that arise from contributions from the respective donor and acceptor units (Fig. 9a) [183,184]. Thus, notable advantages of CPs are their intense absorption bands and high oscillator strengths that exceed those of inorganic semiconductors and enable substantial absorption (molar extinction coefficient reaching above $\sim 10^5\ M^{-1}\ cm^{-1}$) within thin-film devices.

Significant work for DA copolymers has demonstrated that in addition to the various building blocks utilized, important contributions for controlling the bandgap (E_g) include modification of the bond length alternation (BLA) along the conjugated backbone (E_{BLA}), the dihedral angle between DA units (E_θ), resonance effects (E_{res}), electron-donating and withdrawing substituent effects (E_{sub}), and intermolecular interactions between chains (E_{Int}) ($E_g = E_{BLA} + E_\theta + E_{Res} + E_{Sub} + E_{int}$) (Fig. 9b). The DA approach in conjunction with these features suggests possible synthetic strategies to establish bandgap control [185,186]. Smaller BLA values indicate more significant π-electron delocalization and correlate with a narrower E_g [187]. Aromatic resonance in the conjugation path leads to a localization of π-electrons, yielding a larger E_g. In contrast, higher energy quinoidal configurations reduce E_g [188, 189]. The fusion of auxiliary pro-aromatic units to heterocycles within the conjugated polymer backbone enhances quinoidal character and also planarizes the backbone, corresponding to the reduction of E_{res} and $E_{\theta,}$ [190–192]. In combination with the aforementioned design paradigms, strong proquinoidal acceptors have enabled a red-shifting of the absorption farther into the IR [193]. In particular, benzo[1,2-*c*;4,5-*c*']bisthiadiazole (BBT) and [1,2,5]thiadiazolo[3,4-*g*]quinoxaline (TQ) frameworks are representative of such high-electron affinity acceptors that promote quinoidal stabilization and narrow the bandgap significantly when combined with various donors [194,195].

The solubility of CPs in common organic solvents is critically

Table 3
Comparison of colloidal quantum dots infrared devices from the past five years. PC: photoconductor. PD: photodiode. PT: phototransistor.

Device configuration				Device performance							Year/ Ref #
Absorptionmaterials	Structure	Type	Features	Spectral range (μm)	Responsivity (A W^{-1})	Detectivity (Jones)	*LDR* (dB)	Noise (A $Hz^{-0.5}$)	Bandwidth (kHz)	Rise time/ fall time	
PbS	Single layer	PC	Asymmetric electrodes, Schottky junction	0.7–1.8	5.15 at 1550 nm	1.96×10^{10} at 1550 nm	–	–	–	27/8.3 μs	2018/ [145]
PbS	Single layer	PC	Perovskite ligands, fully printed device	0.5–1.4	0.6 at 1000 nm	~10^{12} at 1000 nm	–	5.2×10^{-13} at 10 Hz	~3.3	–	2019/ [146]
HgTe	Single layer	PC	Transfer-printing, scalable fabrication	1–10	0.1 at 2 μm	2×10^{7} at 2 μm	–	–	–	91.5/ 541.3 ms	2016/ [86]
PbS	Bilayer	PC	Bilayer PbS CQD	0.6–1.2	~0.1 at 900 nm	~6×10^{11} at 900 nm	60.94	–	–	3.63/ 29.56 ms	2017/ [65]
PbS/ZnO	Bilayer	PC	Heterojunction structure	0.4–1.5	~0.46 at 1310 nm	4.1×10^{11} at 1310 nm	–	–	–	4.3/0.3 s	2020/ [147]
PbS/$CH_3NH_3PbI_3$	Bilayer	PC	Ligand exchange to align energy level	0.36–1.55	1.58 at 940 nm	3×10^{11} at 940 nm	60	~10^{-12} at 10 Hz	–	42/42 ms	2019/ [148]
PbS/organic	Bilayer	PC	Low dark current and flexible	0.4–1	6.32 at white light	1.1×10^{13} at 630 nm	65	–	–	0.42/0.37 s	2018/ [149]
PbS	Single layer	PD	TiO_2: Nb interlayer	0.4–1.6	~0.28 at 1400 nm	~3×10^{11} at 1400 nm	–	–	–	–	2018/ [150]
PbS	Single layer	PD	Inkjet-printing	0.4–1.65	0.48 at 1 μm	10^{12} at 1 μm	–	–	41	4.4/8.2 μs	2019/ [151]
PbS	Bilayer	PD	Si:PbS heterojunction	0.6–1.7	0.26 at 1540 nm	1.47×10^{11} at 1540 nm	–	~7×10^{-13} at 100 Hz	29.8	2/5.3 μs	2020/ [152]
PbS	Singer layer	PD + LED	IR to visible upconversion imager	0.4–1.6	~20 at 1200 nm	~4×10^{12} at 1200 nm	–	~10^{-12} at 400 Hz	–	1/1.5 ms	2020/ [16]
PbS/n-Si	Hybrid	PD	High quality van der Waals heterojunction on the Si surface	0.4–1.6	0.22 at 1490 nm	4×10^{11} at 1490 nm	–	–	–	47.6/0.8 μs	2020/ [153]
PbS/$MAPbI_{2.5}Br_{0.5}$	Hybrid	PD	Sensitive infrared field-emission photodetector	0.4–1.6	0.7 at 975 nm	~4×10^{12} at 1200 nm	60	~10^{-13} at 100 Hz	60	<10 μs	2017/ [154]
HgTe	Single layer	PD	Bias controlled dual-band photodetection	1.7–6.7	–	>10^{10} at SWIR	–	–	–	–	2019/ [29]
HgTe	Bilayer	PD	Unipolar barrier to reduce dark current	1–3	0.003 at 2.5 μm	3×10^{8} at 2.5 μm	–	~10^{-13} at 1 kHz	>10	–	2018/ [155]
PbS	Bilayer	PD	Large monodispersed PbS QDs with sensitivity >2.5μm	0.4–2.6	0.385 at 2100 nm	1.5×10^{11} at 2100 nm	>42	–	8.1	43/70 μs	2019/ [156]
PbS	Bilayer	PD + ROIC	CMOS compatible	1.1–1.4	5.9 at 1250 nm	–	–	–	–	–	2019/ [157]
PbSe/$CH_3NH_3PbI_3$	Bilayer	PD	Transparent electrode, trap-assisted photomultiplication effect	0.3–2.6	0.24 at 2400 nm	6×10^{11} at 2400 nm	~70	–	–	4/32 μs	2020/ [158]
PbS	Hybrid	Vertical PT + LED	Infrared to visible light upconversion	0.4–1.4	840 at 1042 nm	1.23×10^{13} at 1042 nm	–	–	20	–	2016/ [15]
HgSe	Single layer	PT	As_2S_3 capping, n-dopping	3 – 20	0.8 at 6 μm	10^{8}	–	~10^{-10} at 10 Hz	0.04	–	2016/ [159]
PbS/graphene	Bilayer	PT	Ambipolar, CMOS compatibility	0.7–1.6	1.8×10^{4} at 1550 nm	4.4×10^{12} at 1550 nm	–	–	–	3/200 ms	2018/ [160]
PbS/graphene	Hybrid	PT	Monolithic CMOS image sensors operated in IR	0.3–2	10^{7}	>10^{12}	–	–	–	–	2017/ [161]
PbS/WS_2	Bilayer	PT	Extend response of PbS QDs to 2μm	0.8–2.2	1400 at 1.8 μm	10^{12} at 1.8 μm	–	~10^{-12} at 10 Hz	–	Fall time 0.2 s	2019/ [162]
PbS/MoS_2	Multilayer	PT	Built-in potential within the two QD layers	0.8–1	5.4×10^{4} at 850 nm	1×10^{11} at 850 nm	–	–	–	0.95/1 ms	2018/ [163]
PbS/P3HT	Bilayer	Vertical PT	Vertical PT, built-in electric field in the heterojunction	0.4–2.1	9×10^{4} at 808 nm	2×10^{13} at 808 nm	–	2.2×10^{-11} at 2 Hz	–	9/9.4 ms	2017/ [164]
PbS/Si	Hybrid	PT	Photovoltage generates at the interface	0.4–1.5	>10^{4} at 1300 nm	1.8×10^{12}	–	~2×10^{-10} at 10^{5}Hz	100	10/10 μs	2017/ [125]
HgTe/MoS_2	Bi-layer	PT	TiO_2 encapsulated MoS_2	0.7 – 2.1	~10^{5} at 2100 nm	~10^{12} at 2100 nm	–	~10^{-12} at 1 Hz	–	–	2017/ [165]
Si/graphene	Bilayer	PT	Plasmonic Si QDs doped with boron	0.3–4.5	~10^{8} at 1870 nm	~10^{12} at 1870 nm	–	~10^{-10} at 10 Hz	–	–	2017/ [166]
HgTe: P3HT	BHJ	PT	Chemical grafting between P3HT and HgTe QDs	1.5–2.5	~2 at 1500 nm	~5×10^{11} at 1500 nm	–	~10^{-12} at 100 Hz	100–200	0.8–1.5 us	2020/ [167]

dependent on the solubilizing groups appended to the constituent monomers. However, the steric interactions of sidechains in the solid-state directly influences the dihedral angle between units of the CP backbone [48]. Because the mean dihedral angle between monomer units sets the limit for the delocalization of π-electrons, solution processability must be balanced with the total electronic coherence in the system. More planar systems facilitate the delocalization of π-electrons (E_g narrowing), while decreasing the solubility of the polymer and increasing long-range order and π-stacking between chains [196]. Tightly packed π-systems narrow E_g through diminishing the E_{int} contribution. Besides restricting single (interannular) bond rotation, non-covalent conformational locking has also proven vital to construct

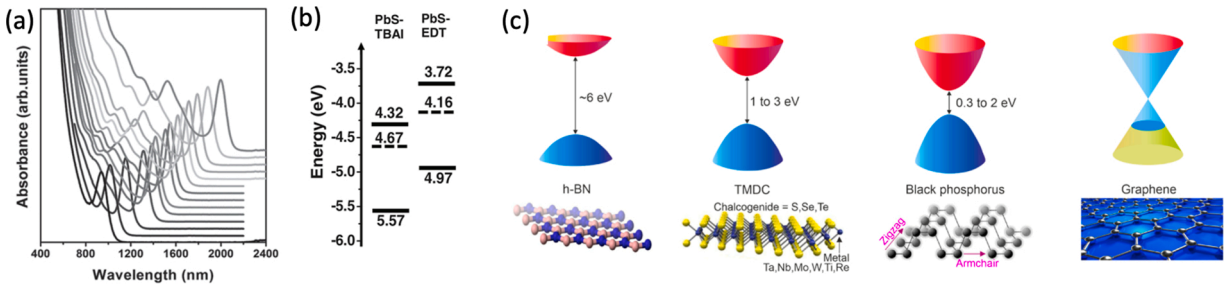

Fig. 8. (a) The absorption spectra measured for PbS CQDs with different sizes from 3.9 to 9.6 nm, showing absorption peak wavelengths from 920 to 2000 nm. Reproduced with permission of Ref. [126]. (b) Energy levels for PbS CQDs with different ligands. The dashed lines represent Femi levels. Reproduced with permission of Ref. 65· (c) Illustration of the bandgaps and molecular structures of various 2D materials. Reproduced with permission of Ref. [5].

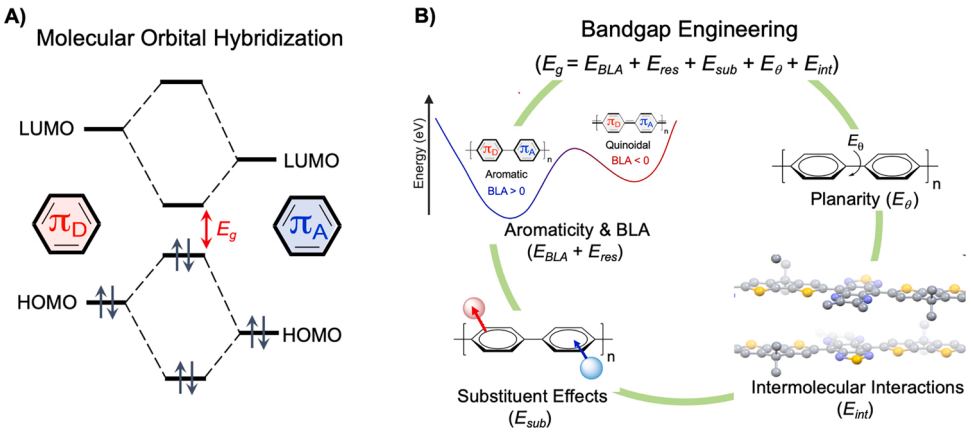

Fig. 9. (a) Energy level diagram for the formation of narrow bandgap DA CPs through molecular orbital hybridization between donor and acceptor units. (b) Strategies for bandgap engineering of DA CPs.

highly planar, extended π-electron systems [83]. Through-space interactions such as O···S, N···S, halogen···S and hydrogen bonding will increase coplanarity, thereby lowering E_g [197,198]. Substitution of electron donating and electron withdrawing groups will affect the electron density and enable control of energy levels and the bandgap through the modulation of the frontier orbital energies [199,200]. Introducing solubilizing groups such as the aliphatic chains at appropriate positions helps to maintain processability, minimize torsion, and enhance π-π stacking [201]. In this section, we consider recent advances that build on these design paradigms and materials which can be applied in organic based IR devices.

In Fig. 10, DA polymers comprised of exocyclic olefin substituted 4-benzylidene-4*H*-cyclopenta[2,1-*b*:3,4-*b'*]dithiophene (*C*=CPhCDT) donors (**P1**-**P11**), in combination with prototypical electron acceptors, display narrow optical bandgaps from 1.2−0.7 eV. The planar sp^2 hybridized olefin aryl functionality places solubilizing substituents at a site remote from the CP backbone [202]. This structural attribute mitigates torsion, increases resilience toward conjugation saturation behavior, and permits strong intermolecular interactions between chains. Linear solubilizing groups (R = $C_{12}H_{25}$) placed at the 3, 5-positions of the phenyl Ph ring promoted the solubility of copolymers comprised of alternating 2,1,3-benzothiadiazole (BT, **P1**), 2,1,3-benzoselenadiazole (BSe, **P2**), pyridal[2,1,3]selenadiazole (PSe, **P3**), and thiophene flanked [1,2,5]thiadiazolo[3,4-*g*]quinoxaline (TQ, **P4**) acceptors. Linear R = $C_{14}H_{29}$ chains were required for the copolymer comprised of a thiophene flanked thieno[3,4-*c*][1,2,5]thiadiazole (TT, **P5**) acceptor. Using **P2**–**P5** in combination with $PC_{71}BM$ showed a long-wavelength photoresponse at zero applied bias with photodiode detectivity $D^* > 10^9$ Jones from 600−1650 nm. Transient absorption spectroscopy on films of **P1**–**P4** and their BHJ blends showed longer exciton lifetimes in polymer aggregates [203]. The aggregation within these materials was found to be essential to compensate for the energy gap law, which predicts that exciton lifetimes decrease with a narrowing of the bandgap. In **P1**–**P4** blends with $PC_{71}BM$, charge carriers formed predominantly at these aggregate sites, leaving rapidly decaying single chain excitons unquenched. These results have important implications toward the further development of materials for infrared organic optoelectronics, where processes such as excited state delocalization will likely be necessary to diminish losses to ultrafast exciton decay in lower bandgap materials.

Further exploration of polymer structure and device physics of these materials has resulted in improved performance. Linear (−OC_nH_{2n+1}) solubilizing groups introduced into the 3,5-positions of the Ph ring enhance photodiode performance in comparison to normal (–C_nH_{2n+1}) variants (*i.e.,* **P6** versus **P4**) [61]. Addition of a high-permittivity additive, camphoric anhydride, to BHJs comprised of **P6** and **P7** blended with $PC_{71}BM$ increases dielectric screening and reduced the exciton binding energy, which led to an increased exciton dissociation efficiency [78]. Adjustment of the **P11**: fullerene blend ratio was found to be another route to reduce the density of deep traps that impede charge transport [204].

A series of DA copolymers comprised of thiophene substituted [1,2,5]thiadiazolo[3,4-*g*]quinoxaline-acceptor (TQ) acceptors and alternating benzene (PBTQ, **P12**), thiophene (PTTQ, **P13**), bithiophene (PBiTTQ, **P14**) and thieno[3,2-*b*]thiophene (PTTTQ, **P15**) donors resulted in polymers with optical bandgaps ranging from 1.14 to 0.87 eV [205]. The effects of auxiliary 2-butyloctyl (BO), 2-hexyldecyl (HD), and 2-octyldodecyl (OD) side chains on the solubility, absorption profiles, and device performance were explored. The large resonance energy of benzene in **P12**-OD gave a polymer with a λ_{max} of 930 nm. The incorporation of thiophene-based donors serves to broaden and shift the absorption onset towards longer wavelengths, resulting in polymers that absorb from 800−1400 nm. Films of **P13**-BO showed a λ_{max} of 1145 nm and measurable absorption extending past 1500 nm. Although a reduction of the gap impacts the dark current density, photodiode detectivities above 10^{10} Jones from 900−1250 nm at -2 V bias were

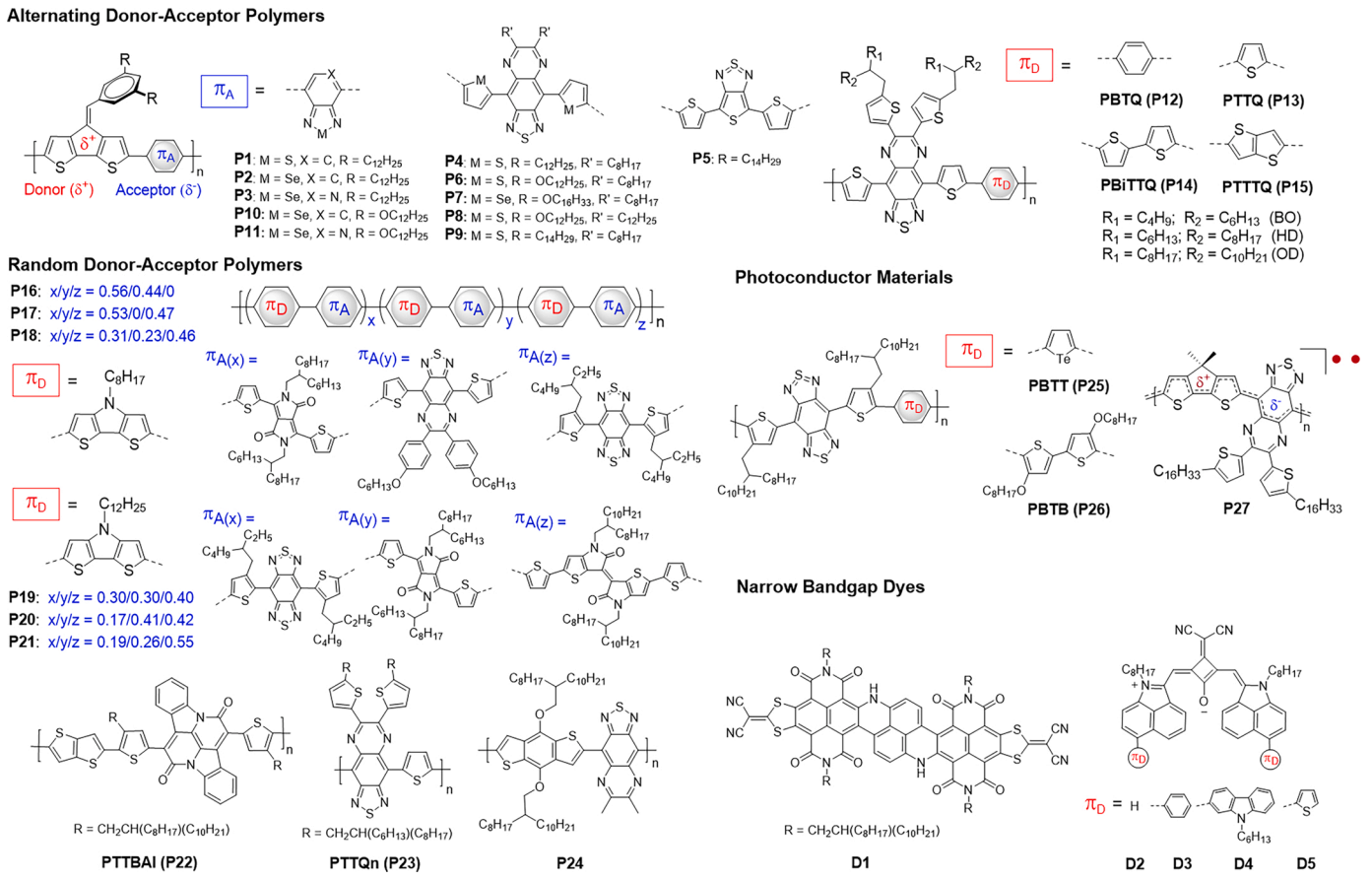

Fig. 10. Molecular structures of narrow bandgap materials mentioned in this review.

achieved for soluble variants.

Three low-bandgap polymers based on *N*-octyl-4*H*-dithieno[3,2-*b*:2′,3′-*d*]pyrrole (DTP) donors and varying ratios of 3,6-dithiophen-2-yl-2,5-dihydropyrrolo[3,4-*c*]pyrrole-1,4-dione (DPP), [1,2,5]thiadiazolo[3,4-*g*]quinoxaline (TQ), and benzo[1,2-*c*;4,5-*c*']bisthiadiazole (BBT) acceptors were synthesized [113]. **P16** paired the DTP donor with DPP and TQ acceptors in a 0.56/0.44 ratio; **P17** contained DPP and BBT acceptors with a molar ratio of 0.53/0.47; and **P18** comprised DPP, TQ, and BBT acceptors with a 0.31/0.23/0.46 M ratio, respectively. The polymer films show a λ_{max} of 988, 726, and 748 nm for **P16**, **P17**, and **P18**, and broad absorption tails extending to ~1100, ~1400, and ~1500 nm, respectively. Using a similar approach, terpolymers comprised of *N*-dodecyl-4*H*-dithieno[3,2-*b*:2′,3′-*d*]pyrrole (DTP) donors and varying ratios of benzo[1,2-*c*;4,5-*c*']bisthiadiazole (BBT), 3,6-dithiophen-2-yl-2,5-dihydropyrrolo[3,4-*c*]pyrrole-1,4-dione (DDP), and (*E*)-[6,6′-bithieno[3,2-*b*]pyrrolylidene]-5,5′ (4*H*,4′*H*)-dione (TII) were synthesized, and their thin films showed a λ_{max} of 814, 838, and 831 nm for **P19**, **P20**, and **P21**, and broad absorption tails extending past 1200, 1400, and 1600 nm, respectively [206]. For **P20** in a photodiode with photo-multiplication, $D^* \geq 10^{11}$ Jones at 300–1600 nm was obtained under a 0.5 V bias. These data are consistent with the incorporation of varying ratios of strong acceptors leading to longer wavelength absorption, tunable properties, and productive charge photogeneration.

Four narrow bandgap photoactive polymers (PBTQ (**P12**), PTTQ (**P13**), PTTBAI (**P22**) and PTTQn (**P23**)) in combination with $PC_{71}BM$ were investigated in BHJ photodiodes to understand the dark current theoretical limit. It was observed that the upper limit for the D^* of NIR OPDs is predominantly limited by non-radiative losses. This allowed calculation of an intrinsic upper limit for D^* of 10^{12} and 10^{10} Jones at 1500 and 2000 nm, respectively [110]. A considerable reduction in the noise and higher detectivity were found in devices using non-fullerene acceptors (NFAs). Seven donor polymers based on **P4**, **P6**, **P8**-**P11** and **P24** with wavelengths of operation between 800 and 1600 nm were paired with $PC_{71}BM$ and NFAs that are derivatives of 3,9-bis(2-methylene-(3-(1,1-dicyanomethylene)-indanone))-55,11,11-tetrakis(4-hexylphenyl)-dithieno[2,3-*d*:2′,3′-*d*']-s-indaceno[1,2-b:6-*b*]dithiophene, with methyl (ITIC-M) or fluoro (ITIC-F) end groups. A significant reduction of the noise and higher D^* was apparent in devices using NFAs. The low noise in NFA blends was attributed to a sharp drop off in the distribution of bandtail states, as revealed by variable-temperature density-of-states measurements [75].

DA copolymers based on alternating tellurophene (PBTT, **P25**) and 4,4′-bis(octyloxy)-[2,2′-bithiophene (PBTB, **P26**) donors combined with 4,8-bis(4-(2-octyldodecyl)thiophen-2-yl)-benzo[1,2-*c*;4,5-*c*']bis[1,2,5]thiadiazole were synthesized [82]. **P25** and **P26** showed an E_g^{opt} of 0.55 and 0.60 eV, respectively. The intrinsic electrical conductivity, on account of the very narrow bandgaps, enabled construction of a photoconductive detector. A $D^* > 1 \times 10^{10}$ Jones was obtained upon illumination at 1064, 1122, and 1342 nm with photoresponse extending to 1450 nm. **P26** adopted a planar conformation, preferential edge on orientation, enhanced exciton lifetime, and slow polaron recombination when compared to **P25**. As a result, **P26**-based photoconductor demonstrated a better responsivity of 0.96 AW^{-1} and *EQE* of 106 % at 1120 nm [82].

A blend of NIR donor polymer based on 2,5-bis(2-octyldodecyl)-3-(5-(5-(thiophen-2-yl)thieno[3,2-*b*]thiophen-2-yl)thiophen-2-yl)-2,5-dihydropyrrolo[3,4-*c*]pyrrole-1,4-dione unit (DPP-DTT) and non-fullerene n-type hetero-polycyclic aromatic SWIR dye (**D1**) showed photoresponse spanning 400−1600 nm and a $D^* > 10^9$ Jones over the 1000–1400 nm range [207]. Small molecules donors based on donor-substituted benz[*cd*]indole-capped SWIR squaraine dyes (**D2**-**D5**) were reported that showed sharp absorption around 1025 nm. These resonance stabilized π-conjugated zwitterionic dyes are comprised of an

electron-deficient central four-membered ring and electron-donating groups in a donor-acceptor-donor configuration to achieve narrow bandgaps [208].

4.3.1. Future challenges for excitonic organic infrared materials

The energy gap law describes that the rate of non-radiative exciton decay increases with a narrowing of the bandgap. As the bandgap is narrowed, increasing vibronic wave function overlap decreases the energy between non-crossing potential energy surfaces and increases the rate of nonradiative decay for both singlet and triplet excitonic states in OSCs [209,210]. As depicted in Fig. 11, the overlap of wavefunctions between the ground and excited states becomes significantly more pronounced, thereby accelerating vibrational relaxation [60]. Thus, a key difference between medium bandgap polymers applied in organic photovoltaics and lower bandgap CPs applied in organic PDs is the closer energy level spacing that gives rise to strong non-radiative processes that limit the exciton lifetime, diffusion length, and ultimately the extractable photocurrent.

However, reports have demonstrated that the dynamics of photoexcited states and non-radiative recombination rates can be regulated in OSCs through modifying coherent coupling by controlling crystallinity, various aggregation phenomena, or by delocalization of excited states over multiple chromophores [203,211]. Moreover, charge generation on ultrafast time scales faster than typical exciton diffusion mechanisms such as direct hot carrier excitation has also been reported. Molecular aggregates are generally classified as H- or J-types aggregates, based on the orientation of the molecular transition dipole moments. For instance, fast vibrational relaxation to the lower excited state as a result of "face-to-face" dipole arrangement in H-aggregates suppress the radiative transitions. On the other hand, "head-to-tail" dipoles of J-aggregates supports radiative transition from lowest excited to the ground state, enabling longer range exciton diffusion [212]. Recently, Chou et al. demonstrated that extended exciton delocalization within J-aggregates bypassed non-radiative pathways [210]. For conjugated polymers, unconventional J-type coupling occurs through intrachain ordering that aligns the transition dipole moments of neighboring repeat units in a head-to-tail fashion, while a high degree of interchain ordering with small spatial separations between neighboring chains is required for H-type coupling. The dynamics are complex and depend highly on local ordering, nanoscale morphology, and molecular design.

The high non-radiative recombination rates in organic semiconductors will likely require new strategies for longer-wavelength detection extending into the SWIR, MWIR, and LWIR [213]. Recent reports have demonstrated that narrow bandgap DA CPs with extensive delocalization and quinoidal character show novel properties such as open-shell electronic structures and intrinsic electrical conductivity [214,215]. The rich behavior of these materials emanates from the collective properties of π-electrons and diminished intramolecular electron pairing. The recent development of high-spin DA CPs with strong electronic correlations and extensive π-delocalization has produced polymers with electronic bandgaps in the SWIR–MWIR and absorption extending well into the LWIR. The first example of a photoconductive detector that used an open-shell DA CP (**P27**) active layer comprised of poly(4-(4,4-dimethyl-4*H*-cyclopenta[2,1-*b*:3,4-*b*']dithiophen-2-yl)-6,7-bis(5-hexadecylthiophen-2-yl)-[1,2,5]thiadiazolo[3,4-*g*]quinoxaline) and senses SWIR, MWIR, and LWIR photons was recently reported [216]. The device architecture consists of transverse gold electrodes on quartz, coated by a polymer film and alumina encapsulant. The device was tested at 5 V bias in the SWIR ($\lambda = 1 - 3$ μm), MWIR ($\lambda = 3 - 5$ μm), and LWIR ($\lambda = 8 - 12$ μm) regions and gave $D^* = 7.53 \times 10^{10} - 1.03 \times 10^{10}$ Jones, $D^* = 3.21 \times 10^{9} - 2.10 \times 10^{9}$ Jones, and $D^* = 2.10 \times 10^{9} - 4.34 \times 10^{9}$ Jones for each region, respectively [216]. Promising pathways and emergent phenomena are being discovered to address the non-radiative recombination loss in disordered semiconductors operating in the infrared regions (Table 4).

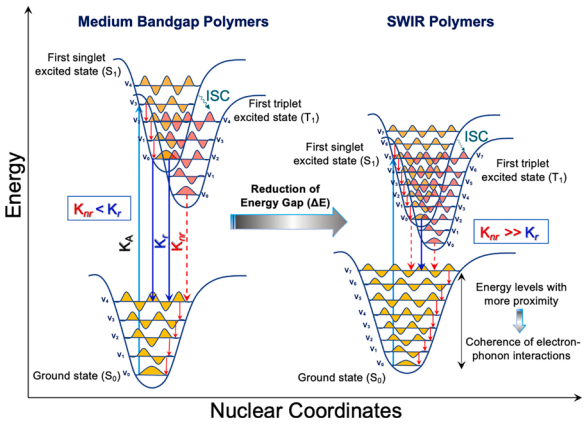

Fig. 11. Potential energy surface of the ground and excited (singlet and triplet) states of the semiconductors absorbing visible (left) versus infrared (right) radiation.

4.4. Perovskites

The family of perovskite materials share the molecular formula ABX_3, where A is a monovalent cation, B is a divalent metal cation and X is a halide anion. Perovskite semiconductors offer the advantages of low exciton binding energy and high charge mobility [230–234], while compatible with solution processing [235,236] for large-area light harvesting and sensing systems, such as solar cells and focal plane arrays. This class of materials has been demonstrated to detect ionizing radiation (gamma and X-ray) [237–239] to terahertz signals corresponding to bolometric effect [240]. The perovskite composition of $CH_3NH_3PbI_3$ exhibits very high absorption coefficient in the visible and sharp optical absorption edge, as shown in Fig. 12a [241]. The high absorption coefficient allows reduction of device thicknesses compared to GaAs and c-Si. The sharp absorption onset indicates a well-ordered microstructure with a low concentration of charge trap states, facilitating fast transport to achieve high-speed electronics capable of MHz response [242,243]. The low trap density in polycrystalline perovskites may potentially lead to lower noise than other solution-processed materials [119].

Currently, research in perovskite devices has been focused on improving response to radiation with wavelengths < 800 nm, but there are some works that show the possibility to extend the spectral response of perovskites to near-infrared, listed in Table 5. The replacement of divalent metal cations Pb by Sn led to tunable absorption profiles of $CH_3NH_3Sn_xPb_{1-x}I_3$, as the increase in Sn to Pb ratio (namely, the parameter x) reduced the material's bandgap (Fig. 12b) [244–247]. Beside the metal cation, changing halide anions in $CH_3NH_3SnI_{3-x}Br_x$ from I to Br extended the photoresponse to 950 nm as seen in Fig. 12c [231]. For perovskites to be used in infrared detection, the community is working on understanding the critical parameters contributing to device degradation and instability [248,249]. Nevertheless, rapid progress is being made in perovskite devices, and it would not be surprising to see this class of materials developed into high-performance infrared detectors in the future. However, the toxic metal Pb is included in these materials or in CQDs, and the potential leakage of heavy metals may hinder their applications to avoid environmental contamination.

5. Unique device designs enabled by thin-film materials

The versatile properties of solution-processed thin films make it possible to process IR detection systems with unique features, such as filter-free wavelength-selective detectors [263–265], large-area pixel-less imagers [15,16,207], flexible detection systems [22,266,267] that are difficult to realize using traditional vacuum-processed inorganic optoelectronics. In this section, we discuss examples of optical designs and

Table 4
Comparison of organic infrared detectors, with response to wavelengths ≥ 900 nm. PD: photodiode. PT: phototransistor.

Device configuration				Device performance							
Absorption materials	Structure	Type	Features	Spectral range (μm)	Responsivity (A W^{-1})	Detectivity (Jones)	*LDR* (dB)	Noise (A $Hz^{-0.5}$)	Bandwidth (kHz)	Rise time/ fall time	Year/ Ref #
PBTB polymer	Single layer	PC	Ultra-narrow bandgap polymer. Flexible detector array for imaging.	0.4–2	0.96 at 1122 nm	>10^{10} at 1064, 1122, 1342 nm	–	–	–	–	2020/ [82]
PDPP3T/ $CH_3NH_3PbI_3$	Bilayer	PC	Complementary absorption	0.3–1	5.5 × 10^{-3} at 937 nm	3.2 × 10^{9} at 937 nm	–	~10^{-12} at 100 Hz	–	30/150 ms	2016/ [217]
PEDOT:PSS/ graphene	Hybrid	PC	photo-thermoelectric effect	Thermal signal	2.2 V/W at	1.4 × 10^{7} at 780 nm	–	–	–	15–30 s	2020/ [170]
PTB7-Th: CO1–4Cl	BHJ	PD	NIR sensitive non-fullerene acceptor	0.4–1.1	~0.5 at 940 nm	3.31 × 10^{13} at 940 nm	126–148	5.9 × 10^{-14} at 100 Hz	240	–	2019/ [105]
PTB7-Th: CTIC-4 F or CO1–4 F or COTIC-4F	BHJ	PD	Three nearly isostructural nonfullerene electron acceptors	0.4–1.1	0.52 at 920 nm for CO1–4F	1.5 × 10^{12} at 920 nm for CO1–4F	–	–	–	–	2019/ [218]
PTB7-Th: $PC_{71}BM$: COi8DFIC	Ternary blend	PD	Complementary absorption	0.4–1	0.35 at 670 nm	~10^{12} at 670 nm	135	1.6 × 10^{-13} at 10 Hz	–	Rise time 900 ns	2019/ [108]
TQ monomers: $PC_{71}BM$	BHJ	PD	Tunable SWIR light absorbing organic materials	0.4–1.5	0.04–0.12 at 1000 nm	10^{10}-2 × 10^{11} at 1000 nm	~180	–	>1000	–	2020/ [205]
CPDT-TQ polymer: $PC_{71}BM$	BHJ	PD	Explain exciton dissociation and charge collection in narrow bandgap systems	0.5–1.5	0.08 at 1000 nm	3 × 10^{10} at 1000 nm	–	~10^{-12} at 100 Hz	–	Fall time ~1 μs	2018/ [61]
Polymer: $PC_{71}BM$	BHJ	PD	Reveal the role of dielectric screening in low bandgap photodetectors	0.5–1.4	0.23 at 1100 nm	1.2 × 10^{11} at 1100 nm	–	5.4 × 10^{-13} at 200 Hz	–	Fall time ~1.5 μs	2018/ [78]
PTB7-Th: NIR acceptor	BHJ	PD	Three norfullerene acceptors with different optoelectronic properties	0.3–1	0.43, 0.34, and 0.25 at 830 nm	4.3 × 10^{12}, 1.9 × 10^{12}, and 2.2 × 10^{12} at 830 nm	150, 137, and 141	2.4 × 10^{-14}, 4.2 × 10^{-14}, and 2.7 × 10^{-14} at 10 Hz	–	Rise time 8.5, 12,10.5 μs	2020/ [219]
NT40: IEICO-4F	BHJ	PD	CuSCN as Anode Interfacial Layer	0.3–1	0.4 at 870 nm	4.4 × 10^{13} at 870 nm	123	~10^{-14} at 10 kHz	–	7.1/ 14.9 μs	2020/ [106]
Four polymer donors: $PC_{71}BM$	BHJ	PD	Non-radiative recombination limits detectivity	0.4–1.6	0.04 at 1000 nm for PBTQ (OD)	~10^{11} at 1000 nm for PBTQ(OD)	–	3 × 10^{-14} for PBTQ (OD)	–	–	2020/ [110]
PMDPP3T: $PC_{61}BM$	BHJ	PD	Conformable imager	0.35–1	~0.68 at 850nm	3.2 × 10^{11}	–	–	–	<150 us	2020/ [22]
PDPP3T: $PC_{61}BM$	BHJ	PD	Large-area, high resolution imager	0.4–1	0.27 at 800 nm	~10^{13} at 800 nm	55	–	–	–	2020/ [220]
(PDPPTDTPT: PCBM)/ $CH_3NH_3PbI_3$	Hybrid	PD	Ultrafast response speed	0.35–1	0.14 at 900 nm	~10^{11} at 900 nm	95	~10^{-12} at 10 Hz	–	5 ns	2017/ [221]
Dye–Perovskite Composites	Hybrid	PD	Narrow band gap organic dyes	0.5–1.8	0.01 at 1500 nm	2 × 10^{7} at 1500 nm	–	3 × 10^{-11} at 1 Hz	85	65/74 μs	2017/ [222]
PTB7-Th: F8IC/ $CH_3NH_3PbI_3$	Hybrid	PD	Complementary absorption and large *LDR*	0.3–1	0.37 at 850 nm	~2 × 10^{11} at 850 nm	191	3 × 10^{-13} at 100 Hz	–	Fall time 5.6 ns	2020/ [67]
PIBDFBTO-HH	Single layer	PT	Small bandgap donor–acceptor polymer	0.4–1.7	0.45 at 940 nm	–	–	–	–	9.4/6.6 ms	2017/ [223]
DPP-DTT: PCBM	BHJ	PT	Wearable photoplethysmogram sensor	–	3.5 × 10^{5} at 810 nm	5.7 × 10^{13} at 810 nm	–	4.3 × 10^{-10} at 500 Hz	–	Fall time 0.6 ms	2017/ [224]
PBIBDF-BT	Single layer	PT	N-type low-band gap donor–acceptor conjugated polymer	0.6–1	0.02 at 980 nm	~4 × 10^{11} at 980 nm	–	–	–	20/30 ms	2018/ [225]
BODIPY-BF2	Single layer	PT	Air-stable n-type organic small molecule, textured film structure	0.3–1.1	1.14 × 10^{4} at 850 nm	–	–	–	–	2.98/ 4.95 ms	2017/ [226]
	Hybrid	PT	Nanowires made from organic small molecule,	0.3–1.2	10.7 at 980 nm	–	–	–	–	3.9/ 1.82 s	2017/ [227]

(*continued on next page*)

Table 4 (*continued*)

Device configuration				Device performance							
Absorption materials	Structure	Type	Features	Spectral range (μm)	Responsivity (A W^{-1})	Detectivity (Jones)	*LDR* (dB)	Noise (A $Hz^{-0.5}$)	Bandwidth (kHz)	Rise time/ fall time	Year/ Ref #
BPE-PTCDI nanowire/Au nanorods			Au nanorods induce plasmon resonances								
SWIR BHJ/IZO	Bilayer	PT	Bilayer decouples charge photogeneration and transport	0.5–1.4	~40 at 940 nm	~5×10^{12} at 1000 nm	127	2×10^{-11} at 1 kHz, (V_G = 0 V)	0.05	–	2019/ [116]
DPP-DTT/ $CH_3NH_3PbI_3$	Bilayer	PT	Complementary absorption bilayer	0.3–0.9	0.08 at 850 nm	~5×10^7 at 850 nm	–	–	–	0.17/ 0.25 s	2019/ [228]
TTF–CA/ graphene	Bilayer	PT	Photogating effect at the organic complex and graphene interface	0.5–3	~5×10^5 at 1000 nm	~10^{11}-10^{12} at 1000 nm	–	~10^{-12} at 1 Hz (V_G=-20 V)	–	11.9/ 15.6 ms	2020/ [229]

electronic upconversion imagers enabled by solution-processed materials.

5.1. Structures to tune spectral selectivity

Typically, the response spectrum of a detector is determined by the absorption profile of the active material [268–272] and the optoelectronic properties of the structures around the detector, e.g., optical resonance cavities or plasmonic structures [25]. When the detector materials show broadband sensitivity, optical filters can be added to block out the unwanted radiation wavelengths. Wavelength-selective detectors can improve the system signal-to-noise ratio by mitigating interferences from the ambient light. For solution processed detectors, in addition to optical filters, there are various designs to achieve selective, narrow spectral response by engineering the materials or/and device structures.

For colloidal quantum dots, the intrinsic property of quantum confinement allows adjustment of their spectral response by changing particle sizes. For example, the absorption peak of colloidal HgSe was tuned with the QD size due to intraband transitions covering 4–9 μm as shown in Fig. 13a [269]. However, the full-width at half-maximum (FWHM) characteristics of the detection spectra were quite broad >2 μm, possibly due to a wide distribution of QD sizes and an inhomogeneous spectral widths caused by coupling of multiple energy levels. To narrow the spectral response, metallic nanostructures were integrated with the detector to enable the redistribution of electro-magnetic field through plasmonic resonance. The resonance wavelength range was adjusted from mid-wave to long-wave IR by changing gold nanodisk dimensions in HgSe QD detectors, with the spectral FWHM < 1.5 μm in Fig. 13b [273].

Organic semiconductors have larger absorption coefficients than traditional vacuum-processed inorganic semiconductors, enabling ultrathin optoelectronics. However, most of the organic detectors are limited in the NIR range. Only a few types of organic semiconductors show photocurrent over 1 μm, due to the difficulty in carrier photogeneration in organics with narrow bandgaps. The charge-transfer states in BHJs extends the device photoresponse to below the materials' bandgaps but are limited by low absorption. Techniques exploiting optical resonance cavities have been shown to enhance the photoresponse originating from charge-transfer states [184]. The mechanism was based on the incorporation of a Fabry–Perot (FP) cavity formed by Ag electrodes, one being completely reflective while the other semi-reflective, as seen in Fig. 13c. The wavelengths at which constructive interference occurred was dependent on the cavity path length and the spacer refraction index, with the peak transmission wavelength dictated by [274]

$$\lambda = \frac{2\pi l\sqrt{n^2 - sin^2\theta}}{\pi m - \varphi} \tag{9}$$

Where l is the optical path, n is the refraction index of the spacer, θ is the incident light angle, m is the interference order, and φ represents the phase shift of light between the two reflective surfaces. With the wavelength selectivity in a resonant microcavity, the detector spectrum reached a remarkably narrow FWHM of 36 nm, with tunable range from 810 to 1550 nm in Fig. 13d. The wavelength-sensitive nature of an FP cavity enhanced the absorption of a specific wavelength of interest, offering the capability to extract spectral information in multispectral detections [21]. In addition, the feasibility to reconstruct a two-dimensional image from the signal of a single organic photodiode was demonstrated by using a FP cavity encoder [204].

Another approach to achieve narrowband detector was through a mechanism known as charge collection narrowing (CCN). In CCN, the charge collection efficiency with respect to wavelengths was shown to vary with the active layer thickness, which in turn led to spectral

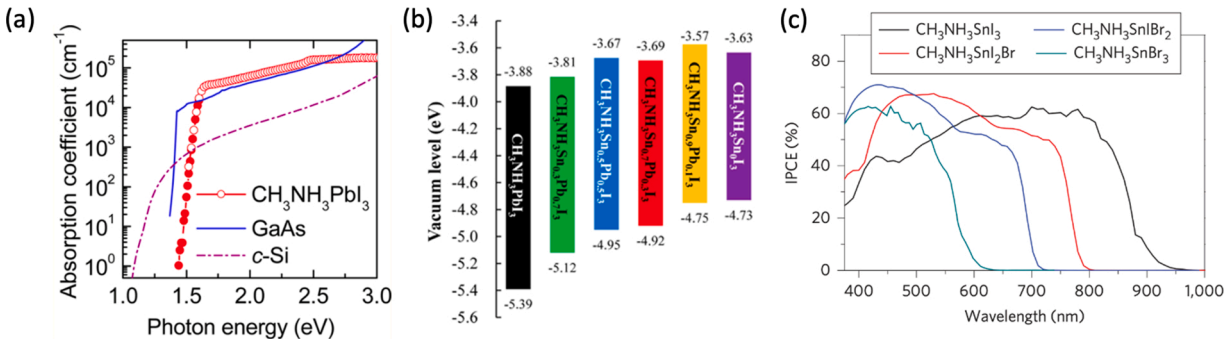

Fig. 12. (a) Comparison of absorption coefficients of $CH_3NH_3PbI_3$, GaAs and c-Si. Reproduced with permission from Ref. [241]. (b) Band energy levels of $CH_3NH_3Sn_xPb_{1-x}I_3$ with various Pb and Sn ratios. Reproduced with permission from Ref. [244]. (c) Photoresponse spectra of $CH_3NH_3SnI_{3-x}Br_x$ devices as a function of Br composition. Reproduced with permission from Ref. [231].

Table 5
Comparison of perovskite devices, with infrared response to wavelengths ≥ 800 nm. PC: photoconductor. PD: photodiode. PT: phototransistor.

Device configuration				Device performance							Year/ Ref#
Absorption materials	Structure	Type	Features	Spectral range (μm)	Responsivity (A W^{-1})	Detectivity (Jones)	*LDR* (dB)	Noise (A $Hz^{-0.5}$)	Bandwidth (kHz)	Rise time/ fall time	
$CH_3NH_3PbI_3$ QDs/TiO_2 NTs	Bilayer	PC	Perovskite QDs/ TiO2 NTs bilayer heterostructure, flexible	0.3–0.85	1.3 at 350 nm, 0.2 at 700 nm	2.5×10^{12} at 350 nm, 3.8×10^{11} at 700 nm	–	–	–	2/1 s at 350 nm,7/ 4 s at 700 nm	2017/ [250]
$CH_3NH_3PbI_3$/C8BTBT	Bilayer	PC	Perovskite/ organic heterojunction; Stable in ambient	0.35–0.8	24.8 at 532 nm	7.7×10^{12} at 532 nm	–	–	–	4.0/ 5.8 ms	2017/ [251]
$(Cs_{0.06}FA_{0.79}MA_{0.15})Pb(I_{0.85}Br_{0.15})_3$	Single layer	PC	Plasmonic nanoantenna to improve NIR detection	0.5–0.8	0.12 at 785 nm	1.5×10^{12} at 785 nm	–	–	–	49/27 ms	2020/ [252]
$FASnI_3$	Single layer	PC	Lead free, p-doping nature, flexible	0.35–1.05	10^5 at 685 nm	1.9×10^{12} at 685 nm	–	4×10^{-10} at 1 Hz	–	180/ 360 s	2019/ [253]
$CH_3NH_3PbI_3$ single crystal	Single layer	PD	Single crystal prepared from solutions; Self-powered mode due to the asymmetric electrodes	0.37–0.83	0.24 at 808 nm	–	–	–	–	71/ 112 us	2016/ [254]
$FAPbI_3$	Single layer	PD	Simultaneously light detection and emission	0.3–0.85	~0.2 at 450 nm	2×10^{12} at 804 nm	148	10^{-11} at 10 Hz	65,000	Fall time ~3.9 ns	2020/ [243]
$CH_3NH_3PbI_3$/CdS	Hybrid layer	PD	Self-powered CdS/perovskite hybrid photodetectors	0.35–0.85	0.48 at 700 nm	2.1×10^{13} at 700 nm	–	–	0.1	0.54/ 2.21 ms	2019/ [255]
$CH_3NH_3PbI_3$	Single layer	PD	Nanoimprinted interlayer, photoresponse was less dependent on incident light angle	0.3–0.8	~0.4 at 750 nm	2×10^{12} at 750 nm	–	–	440	Fall time 0.8 us	2019/ [256]
$MA_{0.5}FA_{0.5}Pb_{0.5}Sn_{0.5}I_3$	Single layer	PD	Tin based perovskite with longer photoresponse.	0.35–1.1	~0.2 at 950 nm	$>10^{12}$ from 800 to 970 nm	–	$\sim 10^{-12}$ at 0.8 Hz	100	–	2017/ [257]
$MA_{0.975}Rb_{0.025}Sn_{0.65}Pb_{0.35}I_3$	Single layer	PD	Rubidium enables increased crystallinity and strengthened preferred orientation	0.3–1.1	0.4 at 910 nm	$>10^{12}$ from 340 to 1000 nm	110	$\sim 3 \times 10^{-14}$ at 100 Hz	1000	40/ 468 ns	2018/ [258]
$CH_3NH_3PbI_3$	Single layer	PD	Ultra-broad photoresponse enabled by photoconductive effect and bolometric effect	UV-THz	~100 at 405 nm, 0.1 at 118 um	$\sim 10^{10}$ at 405 nm, $\sim 10^8$ at 118 um	–	–	–	76/ 126 ns	2020/ [240]
$MAPbI_{3-x}Cl_x$/black phosphorous	Bilayer	PT	Schottky barrier controlled high sensitivity and fast response	0.4–1.2	10^6–10^8	9×10^{13} at 598 nm	–	3×10^{-11}	–	8/17 ms	2019/ [259]
$CH_3NH_3PbI_3/MoS_2$	Bilayer	PT	Charge transfer between perovskite and MoS_2	0.52–0.85	2.12×10^4 at 520 nm, 1.11×10^2 at 850nm	1.38×10^{10} at 520 nm, 7.93×10^7 at 850 nm	–	$\sim 10^{-12}$ at 10 Hz	–	6.17/ 4.5 s	2016/ [260]
$CH_3NH_3PbI_3$:MoS_2 nanoflake BHJ/rGO	Bilayer	PT	Electron trapping in the MoS_2 reduces recombination; Flexible	0.42–0.85	1.08×10^4 at 660 nm	4.28×10^{13} at 660 nm	–	–	–	Both <45 ms	2018/ [261]
Quasi 2D perovskite/IGZO	Bilayer	PT		0.46–1.06			–		–	–	

(*continued on next page*)

Table 5 (*continued*)

Device configuration	Device performance				Year/ Ref#
	Quasi 2D perovskite. Type II band alignment; Large scale and flexible	$>10^5$ at 457 nm	5.1×10^{16} at 457 nm	1.9×10^{-14} at 10 Hz	2019/ [262]

selectivity in detectors [265]. In a thin film, the optical absorption and photogeneration of charges were uniformly distributed in the active layer upon light illumination. Charge collection efficiency was nearly identical for all wavelengths, resulting in a broadband photoresponse correlated to the absorption spectrum of the active layer. On the other hand, for a much thicker active layer (where thickness was greater than the reciprocal of the absorption coefficient), the optical field distribution became wavelength dependent based on the Beer-Lambert law.

As illustrated in Fig. 13e, the penetration of incident light with wavelengths above the detector bandgap decreased exponentially as a

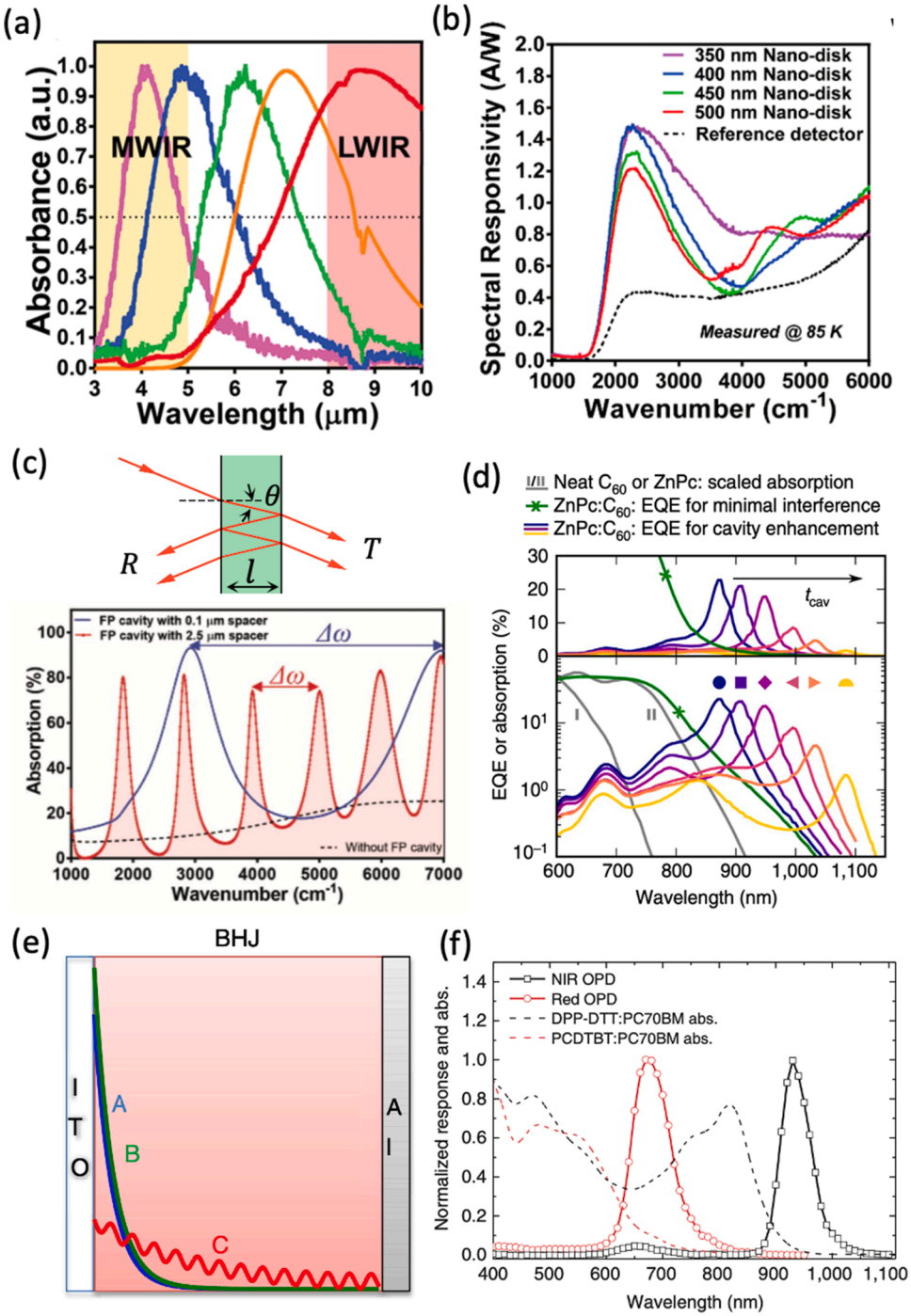

Fig. 13. (a) Absorption profiles of colloidal HgSe QDs with different diameters from 5 to 16 nm. Reproduced with permission of Ref. [269]. (b) Spectral responsivities of HgTe CQD detectors with and without plasmonic disks. Reproduced with permission of Ref. [273]. (c) A schematic of an FP cavity and absorption profiles of HgTe CQDs in an FP cavity with different spacer thickness. Reproduced with permission of Ref. [21]. (d) External quantum efficiencies of organic devices without (green) and with enhanced resonant cavity effects (blue to orange), plotted in linear and log scales. Reproduced with permission of Ref. [184]. (e) The optical field distribution of three different wavelengths in a thick active layer. Lines A and B represent wavelengths larger than the material bandgap, while line C represents a wavelength close to the bandgap with an increased penetration depth. (f) Normalized absorbance spectra of thin (dashed lines) vs thick devices (solid lines), as a function of wavelength. Reproduced with permission of Ref. [265].

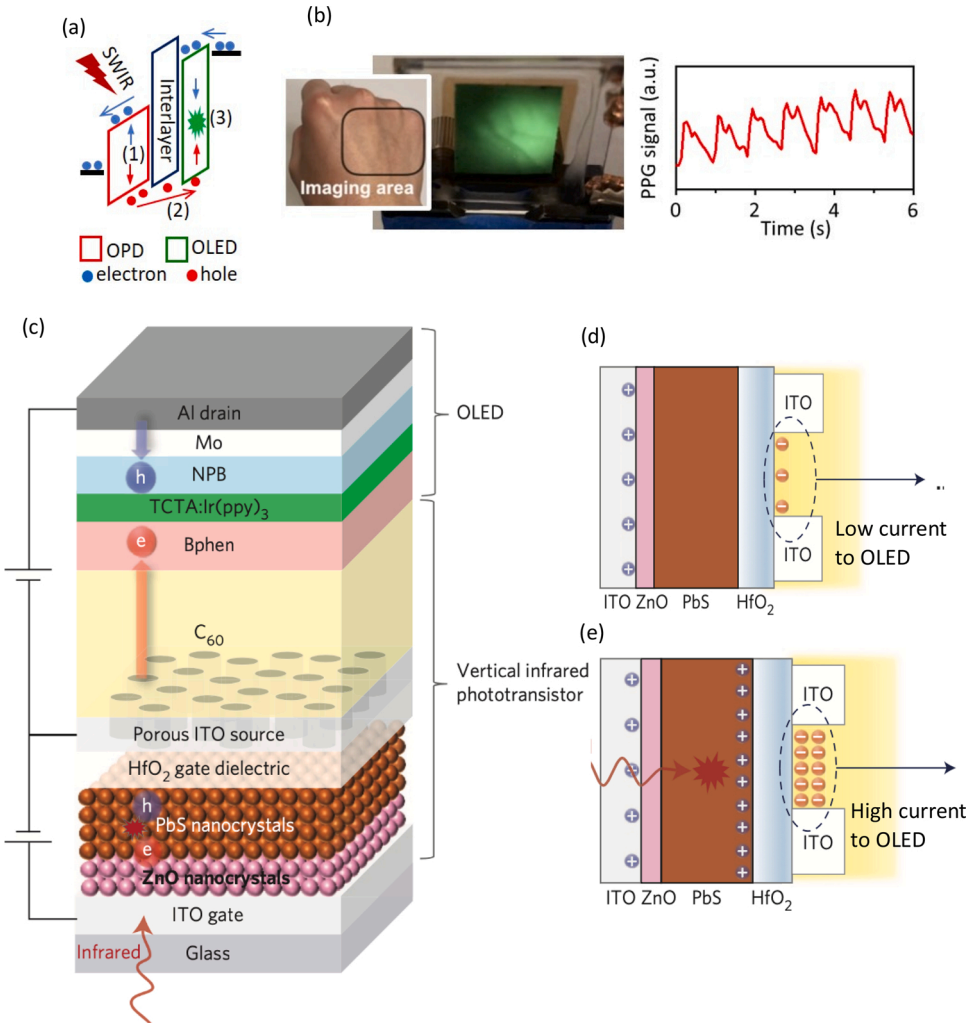

Fig. 14. (a) Operation schematic of an up-conversion imager. (b) Simultaneous spatial imaging of vein pattern and measurement of blood pulses by an organic up-conversion imager. Reproduced with permission from Ref. [17]. (c) Structure of a vertical phototransistor combined with OLED to form an up-conversion detector. Charge accumulation of the phototransistor operated under positive gate voltage (d) in the dark and (e) under IR light. Reproduced with permission from Ref. [[15]].

function of the active layer thickness, due to the strong absorption coefficient (Cases A&B). Meanwhile, radiation with wavelengths near the optical bandgap penetrated deep into the active layer, and charge carriers were generated across the whole active layer because of the relatively weak absorption coefficient for the long wavelengths (Case C). In Cases A&B, charge collection became problematic for carriers generated near one side to reach the collection electrode on the opposite side across the thick active layer, with loss due to recombination and space charge screening effects [265]. In Case C when the carriers were distributed throughout the layer, charge collection was better than in Cases A&B. With the wavelength-dependent charge collection, the CCN approach was successfully used to realize narrowband organic detectors in Fig. 13f, with peak photoresponse located at red and NIR wavelengths and FWHM $<$ 100 nm. The CCN method was material-agnostic and applicable for various disordered and polycrystalline semiconductor-based detectors, with the capability to achieve very narrowband photodetection (<20 nm in FWHM) [275]. The CCN approach alone showed low responsivity, but a combination of CCN and photomulitiplication mechanisms had greatly improved the detectivity of CCN detectors to 10^{11} Jones in the NIR [276,277].

5.2. Up-conversion imagers

Commercial IR imagers are based on focal plane arrays where the IR detecting elements are integrated with readout circuits in pixelated formats to retrieve spatial information. The sensor data are processed, and then the signal magnitudes and locations were reconstituted as an image to be displayed on a screen separate from the detector. Besides this conventional approach, there are alternative strategies to visualize infrared radiation for human vision by direct up-conversion. Thin-film materials are particularly suitable for realizing a monolithic structure that combines the IR detector and visible display into one device, realizing compact up-conversion imagers that does not require external processing electronics for IR visualization [16,23,207,278–283]. The scalability of thin-film imagers to easily reach a large active area of over few square centimeters offers an advantage over conventional arrays that are costly to scale up. In this section, the up-conversion imagers rely on electronic processes based on extrinsic device designs, notably different from the optical anti-Stokes processes originating from materials properties [284].

In Fig. 14a, the up-conversion imager is an integrated stack of an IR photodiode and a visible light emitting diode (LED) in a back-to-back diode configuration. The multi-layer architecture poses challenges for fabrication using vacuum-processed crystalline inorganic IR materials where lattice matching is usually required; but for disordered thin-film materials this epitaxial requirement is not relevant, and the deposition of multiple different layers is relatively straightforward. The working mechanism in the electronic up-conversion device starts with (1) photogeneration of charge carriers the in the detector layer upon IR illumination, followed by (2) charge transport into the LED emitter layer.

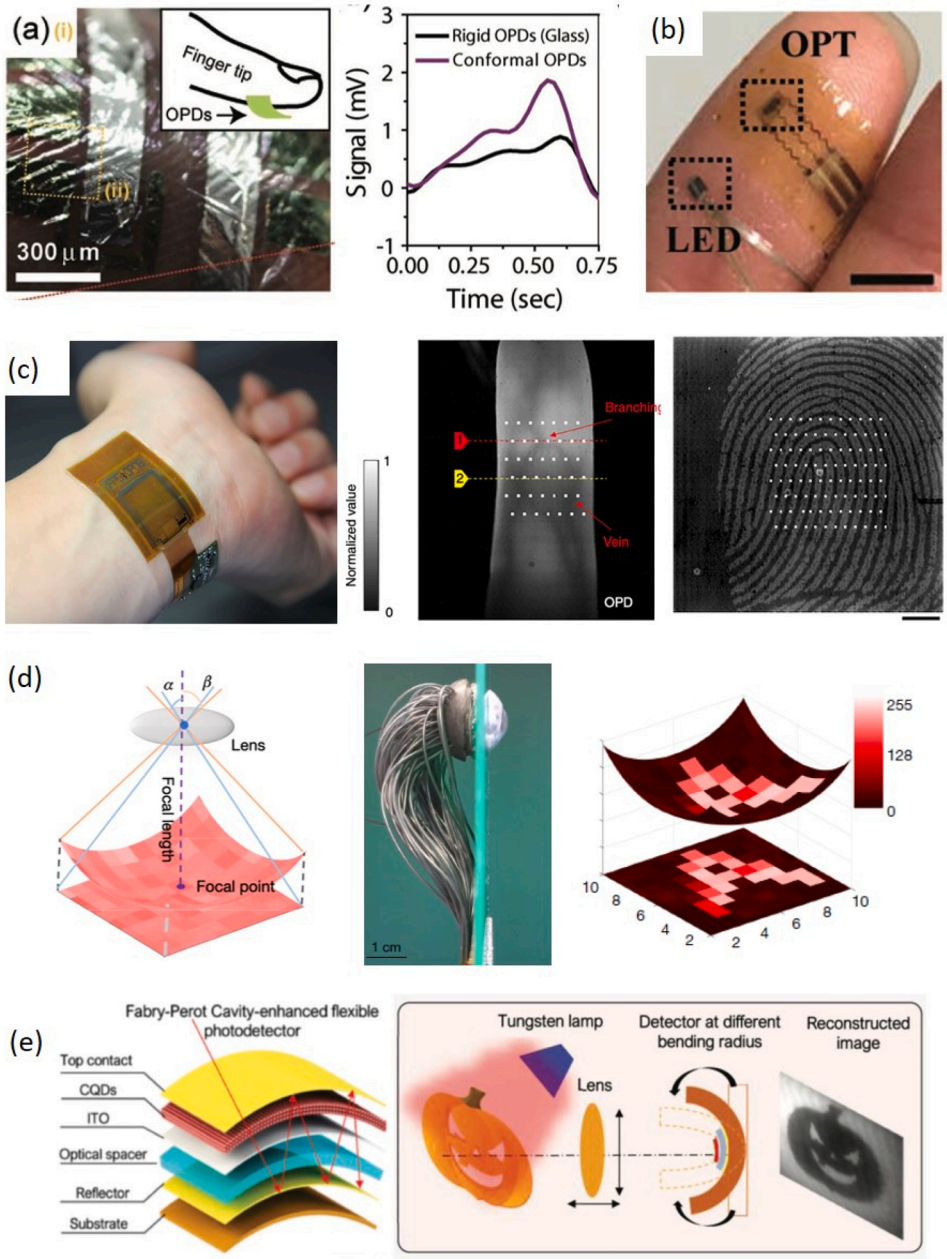

Fig. 15. (a) Conformal organic photodetector showing higher PPG signals than a rigid detector. Reproduced with permission of Ref. [301]. (b) Photograph of a conformal PPG sensor on a finger. Reproduced with permission of Ref. [224]. (c) High-resolution near-infrared imager that mapped out vasculature and a fingerprint. Reproduced with permission of Ref. [22]. (d) Biomimetic hemispherical perovskite nanowire array photodetector. Reproduced with permission of Ref. [303]. (e) Bendable QD photodetector sensitive in the shortwave infrared region. Reproduced with permission of Ref. [21].

Subsequently, (3) charge recombination in the LED layer produces visible photons. Due to the very thin active layers in the imager, charge transport in the direction perpendicular to the electric field is small. Thus, up-conversion is a local process with low lateral spread, such that only the area exposed to IR illumination will give rise to visible emissions, thereby forming an image reflecting the patterns of incident IR light. It is desirable to minimize lateral charge transport so to increase the spatial resolution of the imager, and for many solution-processed semiconductors, their field-dependent, anisotropic hopping transport is helpful to limit charge from spreading laterally.

The energy to convert low-energy IR photons to high-energy visible photons come from the external bias which injects charges into the visible bandgap material. When the injected charges were properly confined to the LED by carefully chosen blocking layers, the electrical current was proportional to the photogenerated charges, and the electrical detectivity of the upconversion imager showed comparable performance to individual diodes. The simultaneous optical and electronic readout of an up-conversion imager is shown in Figure 14b [17], which provided spatial information on the location of blood vessels and temporal measurement of blood pulses through those vessels.

The development of up-conversion imagers has focused on increasing the photon-to-photon up-conversion efficiency $\eta_{p\text{-}p}$ and extending the IR spectral range. The spectral response of the IR detection layer encompasses 1000–1600 nm by using organic dye molecules or PbS QDs [16,207]. The up-conversion efficiency $\eta_{p\text{-}p}$ is the ratio of the flux of emitted visible photons to the flux of incoming IR photons. Typical $\eta_{p\text{-}p}$ values are around a few percent for devices without gain, but in a vertical phototransistor up-conversion device, the photo-multiplication mechanism led to a $\eta_{p\text{-}p}$ record of over 1000 % [15]. The device was different from the back-to-back diode configuration and rather used a vertical phototransistor as the IR detector as shown in Fig. 14**c**. The high gain was enabled by the design of a porous indium tin oxide (ITO) source electrode, which modulated electron injection to the visible OLED under the effects of the gate bias and IR illumination. In the dark (Fig. 14d), the positive gate voltage accumulated only a small number of electrons at the porous ITO/HfO_2 interface,

and the current through the device was low, resulting in low emission at the OLED. With IR illumination, photogeneration took place in the PbS QD layer, effectively creating a significant hole accumulation at the PbS/HfO_2 interface. The accumulated holes increased the electron density in the C_{60} layer, led to a high current injection to the visible OLED, and greatly enhanced the visible light emission and $\eta_{lp\text{-}p}$.

5.3. New form factors

Semiconductors compatible with solution processing methods [48,285–290] allow large-scale fabrication of optoelectronic devices at low cost; moreover, the low-temperature solution-based methods enable facile patterning on flexible substrates to realize new form factors and functionalities, such as biodegradable electronics [291,292] and optoelectronic devices capable of self-healing and operation under mechanical deformations [293–296]. Conformal sensors are particularly appealing for wearable electronics [24,266,297–299] to non-intrusively monitor physiological conditions. Disordered semiconductors also show lower sensitivity to temperature than crystalline materials [300] and can operate at typical body temperatures. Examples of conformal photoplethysmography (PPG) sensors in Fig. 15a and 15b measured near IR optical reflectance through tissues to infer blood oxygenation and pressures during cardiac cycles [224,301,302]. Intimate contact between the PPG sensor and human skin improved the signal amplitude and reduced motion artifacts. The flexible near IR detector array in Fig. 15c provided high resolution maps of vasculatures and fingerprints, useful for biometric applications and detecting health issues such as blood clot locations.

In focal plane array (FPA) imaging systems, multiple lenses are needed to optimize the projection focus across the planar FPA, so as to correct optical aberrations [21]. However, sophisticated lens systems significantly increase the size and cost of the imaging system. To reduce the complexity of the imaging system, a biomimetic design using a hemispherical detector stayed in focus with a simple ball lens and broadened the field of view compared to FPAs (Fig. 15d) [303]. While the early demonstrations of hemispherical eye camera were fabricated by transfer of silicon diodes to curvilinear substrates [304,305], the process limited the fill factor and therefore spatial resolution of the array. Direct integration of solution QD or organic semiconductors [69,306] increased the density of pixels. In Fig. 15e, a bendable QD detector [21] responsive to shortwave infrared was demonstrated to capture high-resolution images with a scanning convex lens. The geometric freedom afforded by the thin film semiconductors have been beneficial to applications such as retinal prosthesis [307,308] and smart contact lens [309]. IR detection enabled by new technologies employing solution-processed semiconductors has been appealing for flexible, wearable optoelectronic systems, due to their unique properties such as light weight, large-area processability, and bio compatibility.

6. Summary and outlook

This review presents the materials and device physics of solution-processed infrared detectors and highlights the characteristics of emerging semiconductors that are different from conventional vacuum-processed crystalline counterparts. The disordered nature of solution-processed materials is a major challenge due to the increased recombination probability that adversely affects photogeneration and dark current noise. However, some of these issues have been mitigated by understanding and engineering the CQD particle interfaces and tuning aggregates and dielectric properties in organic films, to achieve performance within the same order of magnitude as crystalline detectors. Another major challenge is the long-term stability of solution processed devices. Intrinsic disorder increases the densities of midgap states and states near the band edges, leading to carrier trapping and a decline in photoresponse over time. Yet by tuning the biasing waveform and duty cycle, the detrapping process can be managed to obtain steady photoresponse. Extrinsic factors such as exposure to oxygen and humidity may also affect the device stability; fortunately, encapsulation has been well developed for commercial organic light emitting diodes and the know-how from that field is relevant and can be applied to encapsulate and suppress environmental degradation. Nonetheless, further studies are required to investigate device stability under different usage conditions.

With regards to the promising properties, the scalability of semiconductors prepared from solution would enable large-area coverage, low-cost deposition, and monolithic integration with readout circuits that have so far been elusive for infrared detectors. The thin film format allows mechanical flexibility and unique form factors that lower the system size and weight, facilitating new geometries and functions such as wide field-of-view hemispherical detectors and conformal wearable PPG monitors. With further research and development to push up the technology readiness level of solution-processed devices, this low-cost infrared technology will be transformative and offer new approaches to address detection problems in diverse fields ranging from autonomous navigation to health monitoring.

Declaration of Competing Interest

The authors declare that they have no known competing financial interests or personal relationships that could have appeared to influence the work reported in this paper.

Acknowledgement

N.L. and T.N.N acknowledge support from National Science Foundation (ECCS-1839361) and Samsung Advanced Institute of Technology. J.D.A. and P.M. acknowledge support from the Air Force Office of Scientific Research provided by the Organic Materials Chemistry Program (grant FA9550-20-1-0353, program manager: K. Caster) and the National Science Foundation (OIA-1757220).

References

[1] F.P. García De Arquer, A. Armin, P. Meredith, E.H. Sargent, Nat. Rev. Mater. 2 (3) (2017) 16100.
[2] C.L. Tan, H. Mohseni, Nanophotonics 7 (1) (2018) 169–197.
[3] A. Rogalski, Next Decade in Infrared Detectors, Proc. SPIE 10433 (2017) 104330L.
[4] C. Wang, X. Zhang, W. Hu, Chem. Soc. Rev. 49 (2020) 653–670.
[5] A. Rogalski, M. Kopytko, P. Martyniuk, Opto-electronics Rev. 28 (3) (2020) 107–154.
[6] L. Dou, Y. Liu, Z. Hong, G. Li, Y. Yang, Chem. Rev. 115 (23) (2015) 12633–12665.
[7] Z. Wu, Y. Zhai, H. Kim, J.D. Azoulay, T.N. Ng, Acc. Chem. Res. 51 (12) (2018) 3144–3153.
[8] R. Saran, R.J. Curry, Nat. Photonics 10 (2) (2016) 81–92.
[9] O.T. Bruns, T.S. Bischof, D.K. Harris, D. Franke, Y. Shi, L. Riedemann, A. Bartelt, F.B. Jaworski, J.A. Carr, C.J. Rowlands, M.W.B. Wilson, O. Chen, H. Wei, G. W. Hwang, D.M. Montana, I. Coropceanu, O.B. Achorn, J. Kloepper, J. Heeren, P. T.C. So, D. Fukumura, K.F. Jensen, R.K. Jain, M.G. Bawendi, Nat. Biomed. Eng. 1 (4) (2017) 0056.
[10] D.S. Weiss, M. Abkowitz, Chem. Rev. 110 (1) (2010) 479–526.
[11] K.J. Baeg, M. Binda, D. Natali, M. Caironi, Y.Y. Noh, Adv. Mater. 25 (31) (2013) 4267–4295.
[12] H. Wang, D.H. Kim, Chem. Soc. Rev. 46 (17) (2017) 5204–5236.
[13] Y. Xu, Q. Lin, Appl. Phys. Rev. 7 (1) (2020) 011315.
[14] H. Qiao, Z. Huang, X. Ren, S. Liu, Y. Zhang, X. Qi, H. Zhang, Adv. Opt. Mater. 8 (1) (2020) 1–20.
[15] H. Yu, D. Kim, J. Lee, S. Baek, J. Lee, R. Singh, F. So, Nat. Photonics 10 (2) (2016) 129–134.
[16] W. Zhou, Y. Shang, F.P. García de Arquer, K. Xu, R. Wang, S. Luo, X. Xiao, X. Zhou, R. Huang, E.H. Sargent, Z. Ning, F.P.G.De Arquer, K. Xu, R. Wang, S. Luo, X. Xiao, X. Zhou, R. Huang, E.H. Sargent, Z. Ning, Nat. Electron. 3 (5) (2020) 251–258.
[17] N. Li, N. Eedugurala, D.S. Leem, J.D. Azoulay, T.N. Ng, Adv. Funct. Mater. 31 (16) (2021), 2100565.
[18] F. Guo, B. Yang, Y. Yuan, Z. Xiao, Q. Dong, Y. Bi, J. Huang, Nat. Nanotechnol. 7 (12) (2012) 798–802.
[19] L. Li, F. Zhang, J. Wang, Q. An, Q. Sun, W. Wang, J. Zhang, F. Teng, Sci. Rep. 5 (2015) 9181.
[20] H.Y. Chen, M.K.F. Lo, G. Yang, H.G. Monbouquette, Y. Yang, Nat. Nanotechnol. 3 (9) (2008) 543–547.

[21] X. Tang, M.M. Ackerman, G. Shen, P. Guyot-Sionnest, Small 15 (12) (2019) 1804920.
[22] T. Yokota, T. Nakamura, H. Kato, M. Mochizuki, M. Tada, M. Uchida, S. Lee, M. Koizumi, W. Yukita, A. Takimoto, T. Someya, Nat. Electron. 3 (2) (2020) 113–121.
[23] R. Hany, M. Cremona, K. Strassel, Sci. Technol. Adv. Mater. 20 (1) (2019) 497–510.
[24] P.C.Y. Chow, T. Someya, Adv. Mater. 32 (15) (2020) 1902045.
[25] S. Yoon, K.M. Sim, D.S. Chung, J. Mater. Chem. C 6 (48) (2018) 13084–13100.
[26] Gondek, Opto-electronics Rev. 20 (3) (2012) 279–308.
[27] E.L. Dereniak, G.D. Boreman, Infrared Detectors and Systems, JOHN WILEY & SONS, INC., Hoboken, 1996.
[28] W.X.I.V. Herschel, Philos. Trans. R. Soc. London 90 (1800) 284–292.
[29] X. Tang, M.M. Ackerman, M. Chen, P. Guyot-Sionnest, Nat. Photonics 13 (4) (2019) 277–282.
[30] W. Smith, Nature 7 (1873) 303.
[31] F. Watkins, Philos. Mag. Ser. 3 11 (67) (1837) 304–307.
[32] S.P. Langley, Proc. Am. Acad. Arts Sci. 16 (1880) 342–358.
[33] S.P. Langley, Nature 57 (1898) 620–622.
[34] Smithsonian Institution, Smithsonian Miscelleanous Collections, Smithsonian Institution, 1907.
[35] Ohl, R. S. Light-Sensitive Electric Device. U. S. Patent No. 2402662, 1946.
[36] J.N. Shive, Phys. Rev. 76 (4) (1949) 575.
[37] D. Babic, L.W. Johnson, L.V. Snyder, J.J. San Roman, Chalcogenide (2020) 57–65.
[38] S.A. Dvoretsky, N.N. Mikhailov, V.G. Remesnik, Y.G. Sidorov, V.A. Shvets, D. G. Ikusov, V.S. Varavin, M.V. Yakushev, J.V. Gumenjuk-Sichevska, A. G. Golenkov, I.O. Lysiuk, Z.F. Tsybrii, A.V. Shevchik-Shekera, F.F. Sizov, A. V. Latyshev, A.L. Aseev, Opto-electronics Rev. 27 (3) (2019) 282–290.
[39] B.W. Jia, K.H. Tan, W.K. Loke, S. Wicaksono, S.F. Yoon, Appl. Surf. Sci. 440 (2018) 939–945.
[40] T.H. Kil, H.J. Choi, G. Lee, B.H. Lee, S.Y. Jung, R. Ning, C. Park, S.O. Won, H. J. Chang, W.J. Choi, S.H. Baek, J. Eur. Ceram. Soc. 40 (15) (2020) 5582–5588.
[41] J. Goyvaerts, S. Kumari, S. Uvin, J. Zhang, R. Baets, A. Gocalinska, E. Pelucchi, B. Corbett, G. Roelkens, Opt. Express 28 (14) (2020) 21275–21285.
[42] Y. Alimi, V. Pusino, M.J. Steer, D.R.S. Cumming, IEEE Trans. Electron Devices 67 (1) (2020) 179–184.
[43] D. Eich, W. Schirmacher, S. Hanna, K.M. Mahlein, P. Fries, H. Figgemeier, J. Electron. Mater. 46 (9) (2017) 5448–5457.
[44] A. Rogalski, P. Martyniuk, M. Kopytko, Prog. Quantum Electron. 68 (2019), 100228.
[45] J.H. Goldsmith, S. Vangala, J.R. Hendrickson, J.W. Cleary, J.H. Vella, J. Opt. Soc. Am. B 34 (9) (2017) 1965.
[46] J.Y. Na, B. Kang, D.H. Sin, K. Cho, Y.D. Park, Sci. Rep. 5 (1) (2015) 13288.
[47] D. Venkateshvaran, M. Nikolka, A. Sadhanala, V. Lemaur, M. Zelazny, M. Kepa, M. Hurhangee, A.J. Kronemeijer, V. Pecunia, I. Nasrallah, I. Romanov, K. Broch, I. McCulloch, D. Emin, Y. Olivier, J. Cornil, D. Beljonne, H. Sirringhaus, Nature 515 (7527) (2014) 384–388.
[48] Y. Diao, L. Shaw, Z. Bao, S.C.B. Mannsfeld, Energy Environ. Sci. 7 (2014) 2145–2159.
[49] J.F.P. Souza, J.P.M. Serbena, E.L. Kowalski, L.C. Akcelrud, J. Electron. Mater. 47 (2) (2018) 1611–1619.
[50] W.H. Lee, H.H. Choi, D.H. Kim, K. Cho, Adv. Mater. 26 (11) (2014) 1660–1680.
[51] T.N. Ng, M.L. Chabinyc, R.A. Street, A. Salleo, Bias Stress Effects in Organic Thin Film Transistors, IEEE International Reliability Physics Symposium; Phoenix (2007) 243–247.
[52] A. de Jamblinne de Meux, A. Bhoolokam, G. Pourtois, J. Genoe, P. Heremans, Phys. Status Solidi (A) Appl. Mater. Sci. 214 (6) (2017).
[53] W. Wang, G. Xu, M.D.H. Chowdhury, H. Wang, J.K. Um, Z. Ji, N. Gao, Z. Zong, C. Bi, C. Lu, N. Lu, W. Banerjee, J. Feng, L. Li, A. Kadashchuk, J. Jang, M. Liu, Phys. Rev. B 98 (24) (2018) 2–6.
[54] A.G. Dixon, R. Visvanathan, N.A. Clark, N. Stingelin, N. Kopidakis, S.E. Shaheen, J. Polym. Sci. Part B: Polym. Phys. 56 (1) (2018) 31–35.
[55] M. Heydari Gharahcheshmeh, K.K. Gleason, Adv. Mater. Interfaces 6 (1) (2019), 1801564.
[56] J.E. Greivenkamp, Field Guide to Infrared Systems, Detectors, and FPAs. Society of Photo-Optical Instrumentation Engineers (SPIE) All, 2018.
[57] A. Rogalski, P. Martyniuk, M. Kopytko, Rep. Prog. Phys. 79 (4) (2016) 46501.
[58] H. Yu, Z. Dong, J. Guo, D. Kim, F. So, ACS Appl. Mater. Interfaces 8 (16) (2016) 10430–10435.
[59] J.L. Bredas, G.B. Street, Acc. Chem. Res. 18 (10) (1985) 309–315.
[60] J. Benduhn, K. Tvingstedt, F. Piersimoni, S. Ullbrich, Y. Fan, M. Tropiano, K. A. McGarry, O. Zeika, M.K. Riede, C.J. Douglas, S. Barlow, S.R. Marder, D. Neher, D. Spoltore, K. Vandewal, Nat. Energy 2 (2017) 17053.
[61] Z. Wu, W. Yao, A.E. London, J.D. Azoulay, T.N. Ng, Adv. Funct. Mater. 28 (18) (2018), 1800391.
[62] I.G. Scheblykin, A. Yartsev, T. Pullerits, V. Gulbinas, V. Sundström, J. Phys. Chem. B 111 (23) (2007) 6303–6321.
[63] Q. Li, Y. Guo, Y. Liu, Chem. Mater. 31 (17) (2019) 6359–6379.
[64] K. Vandewal, S. Albrecht, E.T. Hoke, K.R. Graham, J. Widmer, J.D. Douglas, M. Schubert, W.R. Mateker, J.T. Bloking, G.F. Burkhard, A. Sellinger, J.M. J. Fréchet, A. Amassian, M.K.M.K. Riede, M.D. McGehee, D. Neher, A. Salleo, Nat. Mater. 13 (1) (2013) 63–68.
[65] Z. Ren, J. Sun, H. Li, P. Mao, Y. Wei, X. Zhong, J. Hu, S. Yang, J. Wang, Adv. Mater. 29 (33) (2017) 1–7.
[66] T.P. Osedach, N. Zhao, S.M. Geyer, L.Y. Chang, D.D. Wanger, A.C. Arango, M. C. Bawendi, V. Bulović, Adv. Mater. 22 (46) (2010) 5250–5254.
[67] C. Li, H. Wang, F. Wang, T. Li, M. Xu, H. Wang, Z. Wang, X. Zhan, W. Hu, L. Shen, Light Sci. Appl. 9 (1) (2020) 1–8.
[68] D. Baran, R.S. Ashraf, D.A. Hanifi, M. Abdelsamie, N. Gasparini, J.A. Röhr, S. Holliday, A. Wadsworth, S. Lockett, M. Neophytou, C.J.M. Emmott, J. Nelson, C.J. Brabec, A. Amassian, A. Salleo, T. Kirchartz, J.R. Durrant, I. Mcculloch, Nat. Mater. 16 (3) (2017) 363–370.
[69] T. Rauch, M. Boberl, S.F. Tedde, J. Furst, M.V. Kovalenko, G.G. Hesser, U. Lemmer, W. Heiss, O. Hayden, Nat. Photonics 3 (6) (2009) 332–336.
[70] J. Hou, O. Inganäs, R.H. Friend, F. Gao, Nat. Mater. 17 (2) (2018) 119–128.
[71] D. Qian, Z. Zheng, H. Yao, W. Tress, T.R. Hopper, S. Chen, S. Li, J. Liu, S. Chen, J. Zhang, X. Liu, B. Gao, L. Ouyang, Y. Jin, G. Pozina, I.A. Buyanova, W.M. Chen, O. Inganäs, V. Coropceanu, J. Bredas, H. Yan, J. Hou, F. Zhang, A.A. Bakulin, F. Gao, Nat. Mater. 17 (8) (2018) 703–709.
[72] N. Gasparini, A. Wadsworth, M. Moser, D. Baran, I. Mcculloch, C.J. Brabec, Adv. Energy Mater. 8 (12) (2018), 1703298.
[73] J. Liu, S. Chen, D. Qian, B. Gautam, G. Yang, J. Zhao, J. Bergqvist, F. Zhang, W. Ma, H. Ade, O. Inganäs, K. Gundogdu, Nat. Energy 1 (9) (2016) 16089.
[74] N. Strobel, M. Seiberlich, T. Rodlmeier, U. Lemmer, G. Hernandez-Sosa, ACS Appl. Mater. Interfaces 10 (49) (2018) 42733.
[75] Z. Wu, N. Li, N. Eedugurala, J.D. Azoulay, D.-S. Leem, T.N. Ng, Npj Flex. Electron. 4 (1) (2020) 6.
[76] I. Constantinou, X. Yi, N.T. Shewmon, E.D. Klump, C. Peng, S. Garakyaraghi, C. K. Lo, J.R. Reynolds, F.N. Castellano, F. So, Adv. Energy Mater. 7 (2017), 1601947.
[77] S. Torabi, F. Jahani, I. Van Severen, C. Kanimozhi, S. Patil, R.W.A. Havenith, R. C. Chiechi, L. Lutsen, D.J. Vanderzande, T.J. Cleij, J.C. Hummelen, L.J.A. Koster, Adv. Funct. Mater. 25 (1) (2015) 150–157.
[78] Z. Wu, Y. Zhai, W. Yao, N. Eedugurala, S. Zhang, L. Huang, X. Gu, J.D. Azoulay, T. N. Ng, Adv. Funct. Mater. 28 (50) (2018), 1805738.
[79] J.J.M. Van Der Holst, M.A. Uijttewaal, R. Balasubramanian, R. Coehoorn, P. Bobbert, G. A.; De Wijs, R.A. A.; De Groot, Phys. Rev. B - Condensed Matter and Mater. Phys. 79 (8) (2009), 085203.
[80] R. Noriega, J. Rivnay, K. Vandewal, F.P.V. Koch, N. Stingelin, P. Smith, M. F. Toney, A. Salleo, Nat. Mater. 12 (11) (2013) 1038–1044.
[81] T. Tiedje, A. Rose, Solid State Commun. 37 (1) (1981) 49–52.
[82] L. Lv, W. Dang, X. Wu, H. Chen, T. Wang, L. Qin, Z. Wei, K. Zhang, G. Shen, H. Huang, Macromolecules 53 (23) (2020) 10636–10643.
[83] M. Wang, M.J. Ford, C. Zhou, M. Seifrid, T.Q. Nguyen, G.C. Bazan, J. Am. Chem. Soc. 139 (48) (2017) 17624–17631.
[84] G. Konstantatos, I. Howard, A. Fischer, S. Hoogland, J. Clifford, E. Klem, L. Levina, E.H. Sargent, Nature 442 (7099) (2006) 180–183.
[85] S. Keuleyan, E. Lhuillier, V. Brajuskovic, P. Guyot-Sionnest, Nat. Photonics 5 (8) (2011) 489–493.
[86] X. Tang, X. Tang, K.W.C. Lai, ACS Photonics 3 (12) (2016) 2396–2404.
[87] D. Kufer, I. Nikitskiy, T. Lasanta, G. Navickaite, F. Koppens, G. Konstantatos, Adv. Mater. 27 (1) (2015) 176–180.
[88] X. Gong, M. Tong, Y. Xia, W. Cai, J.S. Moon, Y. Cao, G. Yu, C.-L.C.-L. Shieh, B. Nilsson, A.J. Heeger, Science 325 (5948) (2009) 1665–1667.
[89] X. Zhou, D. Yang, D. Ma, Adv. Opt. Mater. 3 (11) (2015) 1570–1576.
[90] S.J. Oh, J. Kim, J.M. Mativetsky, Y.-L. Loo, C.R. Kagan, ACS Appl. Mater. Interfaces 8 (42) (2016) 28743–28749.
[91] A.C. Arias, J. Macromol. Sci. Part C- Polym. Rev. 46 (1) (2006) 103–125.
[92] A.C. Arias, N. Corcoran, M. Banach, R.H. Friend, J.D. MacKenzie, W.T.S. Huck, Appl. Phys. Lett. 80 (10) (2002) 1695–1697.
[93] Z. Zhong, L. Bu, P. Zhu, T. Xiao, B. Fan, L. Ying, G. Lu, G. Yu, F. Huang, Y. Cao, ACS Appl. Mater. Interfaces 11 (8) (2019) 8350–8356.
[94] R.A. Street, A. Krakaris, S.R. Cowan, Adv. Funct. Mater. 22 (21) (2012) 4608–4619.
[95] H. Wang, H. Liu, Q. Zhao, Z. Ni, Y. Zou, J. Yang, L. Wang, Y. Sun, Y. Guo, W. Hu, Y. Liu, Adv. Mater. 29 (32) (2017), 1701772.
[96] R. Maiti, C. Patil, M.A.S.R. Saadi, T. Xie, J.G. Azadani, B. Uluutku, R. Amin, A. F. Briggs, M. Miscuglio, D. Van Thourhout, S.D. Solares, T. Low, R. Agarwal, S. R. Bank, V.J. Sorger, Nat. Photonics 14 (9) (2020) 578–584.
[97] C. Liu, Y. Xu, Y. Noh, Mater. Today 18 (2) (2015) 79–96.
[98] Y. Zhou, C. Fuentes-hernandez, J. Shim, J. Meyer, A.J. Giordano, H. Li, P. Winget, T. Papadopoulos, H. Cheun, J. Kim, M. Fenoll, A. Dindar, W. Haske, E. Najafabadi, T.M. Khan, H. Sojoudi, S. Barlow, S. Graham, J. Brédas, S. R. Marder, A. Kahn, B. Kippelen, Science 336 (2012) 327–332.
[99] D. Ouyang, Z. Huang, W.C.H. Choy, Adv. Funct. Mater. 29 (1) (2019) 1804660.
[100] D. Qian, Z. Zheng, H. Yao, W. Tress, T.R. Hopper, S. Chen, S. Li, J. Liu, S. Chen, J. Zhang, X.K. Liu, B. Gao, L. Ouyang, Y. Jin, G. Pozina, I.A. Buyanova, W. M. Chen, O. Inganäs, V. Coropceanu, J.L. Bredas, H. Yan, J. Hou, F. Zhang, A. A. Bakulin, F. Gao, Nat. Mater. 17 (8) (2018) 703–709.
[101] J. Yoo, S. Jeong, S. Kim, J.H. Je, Adv. Mater. 27 (10) (2015) 1712–1717.
[102] N. Li, Z. Lan, L. Cai, F. Zhu, J. Mater. Chem. C 7 (13) (2019) 3711–3729.
[103] G. Simone, M.J. Dyson, S.C.J.J. Meskers, R.A.J.J. Janssen, G.H. Gelinck, Adv. Funct. Mater. 30 (20) (2019), 1904205.
[104] G. Simone, M.J. Dyson, C.H.L. Weijtens, S.C.J. Meskers, R. Coehoorn, R.A. J. Janssen, G.H. Gelinck, Adv. Opt. Mater. 8 (1) (2019), 1901568.
[105] J. Huang, J. Lee, J. Vollbrecht, V.V. Brus, A.L. Dixon, D.X. Cao, Z. Zhu, Z. Du, H. Wang, K. Cho, G.C. Bazan, T.Q. Nguyen, Adv. Mater. 32 (1) (2020) 1906027.
[106] Z. Huang, Z. Zhong, F. Peng, L. Ying, G. Yu, F. Huang, Y. Cao, ACS Appl. Mater. Interfaces 13 (2021) 1027.

[107] G. Simone, D. Tordera, E. Delvitto, B. Peeters, A.J.J.M. van Breemen, S.C. J. Meskers, R.A.J. Janssen, G.H. Gelinck, Adv. Opt. Mater. 8 (10) (2020), 1901989.
[108] W. Li, Y. Xu, X. Meng, Z. Xiao, R. Li, L. Jiang, L. Cui, M. Zheng, C. Liu, L. Ding, Q. Lin, Adv. Funct. Mater. 29 (20) (2019) 1808948.
[109] E. Saracco, B. Bouthinon, J.M. Verilhac, C. Celle, N. Chevalier, D. Mariolle, O. Dhez, J.P. Simonato, Adv. Mater. 25 (45) (2013) 6534–6538.
[110] S. Gielen, C. Kaiser, F. Verstraeten, J. Kublitski, J. Benduhn, D. Spoltore, P. Verstappen, W. Maes, P. Meredith, A. Armin, K. Vandewal, Adv. Mater. 32 (47) (2020), 2003818.
[111] R. Bube, Photoconductivity of Solids, JOHN WILEY & SONS, INC., 1978.
[112] A. Pierre, A. Gaikwad, A.C. Arias, Nat. Photonics 11 (3) (2017) 193–199.
[113] J. Han, D. Yang, D. Ma, W. Qiao, Z.Y. Wang, Adv. Opt. Mater. 6 (15) (2018) 1800038.
[114] N. Li, J. Lim, J.D. Azoulay, T.N. Ng, J. Mater. Chem. C 8 (43) (2020) 15142–15149.
[115] R. Dong, C. Bi, Q. Dong, F. Guo, Y. Yuan, Y. Fang, Z. Xiao, J. Huang, Adv. Opt. Mater. 2 (6) (2014) 549–554.
[116] H. Kim, Z. Wu, N. Eedugurala, J.D. Azoulay, T.N. Ng, ACS Appl. Mater. Interfaces 11 (40) (2019) 36880–36885.
[117] J.W. Lee, D.Y. Kim, F. So, Adv. Funct. Mater. 25 (8) (2015) 1233–1238.
[118] Y. Fang, A. Armin, P. Meredith, J. Huang, Nat. Photonics 13 (1) (2019) 1–4.
[119] Y. Fang, J. Huang, Adv. Mater. 27 (17) (2015) 2804–2810.
[120] K. Kato, S. Hata, J. Yoshida, A. Kozen, Design of High-Speed and High-Sensitivity Photodiode with an Input Optical Waveguide on Semi-Insulating InP Substrate, LEOS 1992 Summer Topical Meeting Digest on Broadband Analog and Digital Optoelectronics, Optical Multiple Access Networks, Integrated Optoelectronics, and Smart Pixels (1992) 254–257.
[121] F. Xia, T. Mueller, Yming Lin, P. Avouris, Nat. Nanotechnol. 4 (2009) 839.
[122] G. Konstantatos, L. Levina, A. Fischer, E.H. Sargent, Nano Lett. 8 (5) (2008) 1446–1450.
[123] M. Chen, H. Yu, S.V. Kershaw, H. Xu, S. Gupta, F. Hetsch, A.L. Rogach, N. Zhao, Adv. Funct. Mater. 24 (1) (2014) 53–59.
[124] L. Yan, Y. Yu, A.C. Zhang, D. Hall, I.A. Niaz, M.A. Raihan Miah, Y.H. Liu, Y.H. Lo, Appl. Phys. Lett. 111 (10) (2017), 101104.
[125] V. Adinolfi, E.H. Sargent, Nature 542 (7641) (2017) 324–327.
[126] J.W. Lee, D.Y. Kim, S. Baek, H. Yu, F. So, Small 12 (10) (2016) 1328–1333.
[127] M. Böberl, M.V. Kovalenko, S. Gamerith, E.J.W. List, W. Heiss, Adv. Mater. 19 (21) (2007) 3574–3578.
[128] J.S. Lee, M.V. Kovalenko, J. Huang, D.S. Chung, D.V. Talapin, Nat. Nanotechnol. 6 (6) (2011) 348–352.
[129] M. Shim, P. Guyot-sionnest, Nature 407 (6807) (2000) 981–983.
[130] I. Ramiro, O. Özdemir, S. Christodoulou, S. Gupta, M. Dalmases, I. Torre, G. Konstantatos, Nano Lett. 20 (2) (2020) 1003–1008.
[131] R.D. Harris, S. Bettis Homan, M. Kodaimati, C. He, A.B. Nepomnyashchii, N. K. Swenson, S. Lian, R. Calzada, E.A. Weiss, Chem. Rev. 116 (21) (2016) 12865–12919.
[132] C.H.M. Chuang, P.R. Brown, V. Bulović, M.G. Bawendi, Nat. Mater. 13 (8) (2014) 796–801.
[133] S.J. Oh, D.B. Straus, T. Zhao, J.-H. Choi, S.-W. Lee, E.A. Gaulding, C.B. Murray, C. R. Kagan, Chem. Commun. 53 (2017) 728–731.
[134] C. Livache, B. Martinez, N. Goubet, J. Ramade, E. Lhuillier, Front. Chem. 6 (2018) 575.
[135] M. Yarema, S. Pichler, M. Sytnyk, R. Seyrkammer, R.T. Lechner, G. Fritz-Popovski, D. Jarzab, K. Szendrei, R. Resel, O. Korovyanko, M.A. Loi, O. Paris, G. Hesser, W. Heiss, ACS Nano 5 (5) (2011) 3758–3765.
[136] V. Srivastava, E. Dunietz, V. Kamysbayev, J.S. Anderson, D.V. Talapin, Chem. Mater. 30 (11) (2018) 3623–3627.
[137] S. Dongre, S. Paul, S. Mondal, R. Kumar, D. Panda, S.A. Gazi, D. Das, R. Kumar, S. R. Shriram, M.R. Mantri, B. Tongbram, S. Chakrabarti, ACS Appl. Electron. Mater. 2 (5) (2020) 1243–1253.
[138] D. Franke, D.K. Harris, O. Chen, O.T. Bruns, J.A. Carr, M.W.B. Wilson, M. G. Bawendi, Nat. Commun. 7 (1) (2016) 1–9.
[139] A.Y. Chang, W. Liu, D.V. Talapin, R.D. Schaller, ACS Nano 8 (8) (2014) 8513–8519.
[140] W.Y. Lee, S. Ha, H. Lee, J.H. Bae, B. Jang, H.J. Kwon, Y. Yun, S. Lee, J. Jang, Adv. Opt. Mater. 7 (22) (2019) 2–8.
[141] A. Sahu, L. Qi, M.S. Kang, D. Deng, D.J. Norris, J. Am. Chem. Soc. 133 (17) (2011) 6509–6512.
[142] S.B. Hafiz, M.R. Scimeca, P. Zhao, I.J. Paredes, A. Sahu, D.K. Ko, ACS Appl. Nano Mater. 2 (3) (2019) 1631–1636.
[143] K. Xu, W. Zhou, Z. Ning, Small 16 (47) (2020) 2003397.
[144] A.P. Litvin, I.V. Martynenko, F. Purcell-Milton, A.V. Baranov, A.V. Fedorov, Y. K. Gun'Ko, J. Mater. Chem. A 5 (26) (2017) 13252–13275.
[145] Y. Tang, F. Wu, F. Chen, Y. Zhou, P. Wang, M. Long, W. Zhou, Z. Ning, J. He, F. Gong, Z. Zhu, S. Qin, W. Hu, Small 14 (48) (2018) 1–8.
[146] A. Yousefiamin, N.A. Killilea, M. Sytnyk, P. Maisch, K.C. Tam, H.J. Egelhaaf, S. Langner, T. Stubhan, C.J. Brabec, T. Rejek, M. Halik, K. Poulsen, J. Niehaus, A. Köck, W. Heiss, ACS Nano 13 (2) (2019) 2389–2397.
[147] X. Wang, K. Xu, X. Yan, X. Xiao, C. Aruta, V. Foglietti, Z. Ning, N. Yang, ACS Appl. Mater. Interfaces 12 (7) (2020) 8403–8410.
[148] J.Y. Zhang, J.L. Xu, T. Chen, X. Gao, S.D. Wang, ACS Appl. Mater. Interfaces 11 (47) (2019) 44430–44437.
[149] Y. Wei, Z. Ren, A. Zhang, P. Mao, H. Li, X. Zhong, W. Li, S. Yang, J. Wang, Adv. Funct. Mater. 28 (11) (2018), 1706690.
[150] E. Georgitzikis, P.E. Malinowski, J. Maes, A. Hadipour, Z. Hens, P. Heremans, D. Cheyns, Adv. Funct. Mater. 28 (42) (2018), 1804502.
[151] R. Sliz, M. Lejay, J.Z. Fan, M.J. Choi, S. Kinge, S. Hoogland, T. Fabritius, F. P. Garciá De Arquer, E.H. Sargent, ACS Nano 13 (10) (2019) 11988–11995.
[152] K. Xu, X. Xiao, W. Zhou, X. Jiang, Q. Wei, H. Chen, Z. Deng, J. Huang, B. Chen, Z. Ning, ACS Appl. Mater. Interfaces 12 (13) (2020) 15414–15421.
[153] X. Xiao, K. Xu, M. Yin, Y. Qiu, W. Zhou, L. Zheng, X. Cheng, Y. Yu, Z. Ning, Appl. Phys. Lett. 116 (10) (2020).
[154] F.P. García De Arquer, X. Gong, R.P. Sabatini, M. Liu, G.H. Kim, B.R. Sutherland, O. Voznyy, J. Xu, Y. Pang, S. Hoogland, D. Sinton, E. Sargent, Nat. Commun. 8 (2017) 14757.
[155] A. Jagtap, B. Martinez, N. Goubet, A. Chu, C. Livache, C. Gréboval, J. Ramade, D. Amelot, P. Trousset, A. Triboulin, S. Ithurria, M.G. Silly, B. Dubertret, E. Lhuillier, ACS Photonics 5 (11) (2018) 4569–4576.
[156] C. Dong, S. Liu, N. Barange, J. Lee, T. Pardue, X. Yi, S. Yin, F. So, ACS Appl. Mater. Interfaces 11 (47) (2019) 44451–44457.
[157] Q. Xu, L. Meng, T. Zeng, K. Sinha, C. Dick, X. Wang, Opt. Lett. 44 (2) (2019) 463.
[158] T. Zhu, Y. Yang, L. Zheng, L. Liu, M.L. Becker, X. Gong, Adv. Funct. Mater. 30 (15) (2020), 1909487.
[159] E. Lhuillier, M. Scarafagio, P. Hease, B. Nadal, H. Aubin, X.Z. Xu, N. Lequeux, G. Patriarche, S. Ithurria, B. Dubertret, Nano Lett. 16 (2) (2016) 1282–1286.
[160] L. Zheng, W. Zhou, Z. Ning, G. Wang, X. Cheng, W. Hu, W. Zhou, Z. Liu, S. Yang, K. Xu, M. Luo, Y. Yu, Adv. Opt. Mater. 6 (23) (2018), 1800985.
[161] S. Goossens, G. Navickaite, C. Monasterio, S. Gupta, J.J. Piqueras, R. Pérez, G. Burwell, I. Nikitskiy, T. Lasanta, T. Galán, E. Puma, A. Centeno, A. Pesquera, A. Zurutuza, G. Konstantatos, F. Koppens, Nat. Photonics 11 (6) (2017) 366–371.
[162] O. Özdemir, I. Ramiro, S. Gupta, G. Konstantatos, ACS Photonics 6 (10) (2019) 2381–2386.
[163] S. Pak, Y. Cho, J. Hong, J. Lee, S. Lee, B. Hou, G.H. An, Y.W. Lee, J.E. Jang, H. Im, S.M. Morris, J.I. Sohn, S. Cha, J.M. Kim, ACS Appl. Mater. Interfaces 10 (44) (2018) 38264–38271.
[164] H. Zhang, Y. Zhang, X. Song, Y. Yu, M. Cao, Y. Che, Z. Zhang, H. Dai, J. Yang, G. Zhang, J. Yao, ACS Photonics 4 (3) (2017) 584–592.
[165] N. Huo, S. Gupta, G. Konstantatos, Adv. Mater. 29 (17) (2017), 1606576.
[166] Z. Ni, L. Ma, S. Du, Y. Xu, M. Yuan, H. Fang, Z. Wang, M. Xu, D. Li, J. Yang, W. Hu, X. Pi, D. Yang, ACS Nano 11 (10) (2017) 9854–9862.
[167] Y. Dong, M. Chen, W.K. Yiu, Q. Zhu, G. Zhou, S.V. Kershaw, N. Ke, C.P. Wong, A. L. Rogach, Adv. Sci. 7 (12) (2020), 2000068.
[168] M.S. Arnold, J.D. Zimmerman, C.K. Renshaw, X. Xu, R.R. Lunt, C.M. Austin, S. R. Forrest, Nano Lett. 9 (2009) 3354–3358.
[169] B. Deng, C. Ma, Q. Wang, S. Yuan, K. Watanabe, T. Taniguchi, F. Zhang, F. Xia, Nat. Photonics 14 (9) (2020) 549–553.
[170] M. Zhang, J.T.W. Yeow, Carbon 156 (2020) 339–345.
[171] J. Yan, M.H. Kim, J.A. Elle, A.B. Sushkov, G.S. Jenkins, H.M. Milchberg, M. S. Fuhrer, H.D. Drew, Nat. Nanotechnol. 7 (7) (2012) 472–478.
[172] C. Yin, C. Gong, J. Chu, X. Wang, C. Yan, S. Qian, Y. Wang, G. Rao, H. Wang, Y. Liu, X. Wang, J. Wang, W. Hu, C. Li, J. Xiong, Adv. Mater. 32 (25) (2020), 2002237.
[173] X. Ren, Z. Li, Z. Huang, D. Sang, H. Qiao, X. Qi, J. Li, J. Zhong, H. Zhang, Adv. Funct. Mater. 27 (18) (2017), 1606834.
[174] X. Li, D. Yu, J. Chen, Y. Wang, F. Cao, Y. Wei, Y. Wu, L. Wang, Y. Zhu, Z. Sun, J. Ji, Y. Shen, H. Sun, H. Zeng, ACS Nano 11 (2) (2017) 2015–2023.
[175] Y. Wang, R. Fullon, M. Acerce, C.E. Petoukhoff, J. Yang, C. Chen, S. Du, S.K. Lai, S.P. Lau, D. Voiry, D. O'Carroll, G. Gupta, A.D. Mohite, S. Zhang, H. Zhou, M. Chhowalla, Adv. Mater. 29 (4) (2017), 1603995.
[176] H. Bronstein, C.B. Nielsen, B.C. Schroeder, I. McCulloch, Nat. Rev. Chem. 4 (2) (2020) 66–77.
[177] T.M. Clarke, J.R. Durrant, Chem. Rev. 110 (11) (2010) 6736–6767.
[178] Z.B. Henson, K. Müllen, G.C. Bazan, Nat. Chem. 4 (9) (2012) 699–704.
[179] Z. Qiu, B.A.G. Hammer, K. Müllen, Prog. Polym. Sci. 100 (2020), 101179.
[180] K. Müllen, W. Pisula, J. Am. Chem. Soc. 137 (30) (2015) 9503–9505.
[181] V.V. Brus, J. Lee, B.R. Luginbuhl, S.-J. Ko, G.C. Bazan, T.-Q. Nguyen, Adv. Mater. 31 (30) (2019), 1900904.
[182] M.C. Scharber, N.S. Sariciftci, Adv. Mater. Technol. 6 (4) (2021), 2000857.
[183] G. Li, W.-H. Chang, Y. Yang, Nat. Rev. Mater. 2 (8) (2017) 17043.
[184] B. Siegmund, A. Mischok, J. Benduhn, O. Zeika, S. Ullbrich, F. Nehm, M. Böhm, D. Spoltore, H. Fröb, C. Körner, K. Leo, K. Vandewal, M. Bohm, D. Spoltore, H. Frob, C. Korner, K. Leo, K. Vandewal, Nat. Commun. 8 (2017) 15421.
[185] J. Roncali, Chem. Rev. 97 (1) (1997) 173–206.
[186] J. Huang, G. Yu, Chem. Mater. 33 (5) (2021) 1513–1539.
[187] M. Heydari Gharahcheshmeh, K.K. Gleason, Mater. Today Adv. 8 (2020), 100086.
[188] P.M. Burrezo, J.L. Zafra, J.T. López Navarrete, J. Casado, Angew. Chem. Int. Ed. 56 (9) (2017) 2250–2259.
[189] B. Yuan, C. Li, Y. Zhao, O. Gröning, X. Zhou, P. Zhang, D. Guan, Y. Li, H. Zheng, C. Liu, Y. Mai, P. Liu, W. Ji, J. Jia, S. Wang, J. Am. Chem. Soc. 142 (22) (2020) 10034–10041.
[190] V. Lemaur, J. Cornil, R. Lazzaroni, H. Sirringhaus, D. Beljonne, Y. Olivier, Chem. Mater. 31 (17) (2019) 6889–6899.
[191] N. Bérubé, J. Gaudreau, M. Côté, Macromolecules 46 (17) (2013) 6873–6880.
[192] K.S. Mayer, D.J. Adams, N. Eedugurala, M.M. Lockart, P. Mahalingavelar, L. Huang, L.A. Galuska, E.R. King, X. Gu, M.K. Bowman, J.D. Azoulay, Cell Rep. Phys. Sci. 2 (6) (2021) 100467.
[193] J. Casado, Topics Curr. Chem. (Cham) 375 (4) (2017) 73.
[194] C. Kitamura, S. Tanaka, Y. Yamashita, Chem. Mater. 8 (2) (1996) 570–578.
[195] E. Havinga, Polym. Bull. 29 (1) (1992) 119–126.
[196] C. Zhan, J. Yao, Chem. Mater. 28 (7) (2016) 1948–1964.

[197] G. Conboy, H.J. Spencer, E. Angioni, A.L. Kanibolotsky, N.J. Findlay, S.J. Coles, C. Wilson, M.B. Pitak, C. Risko, V. Coropceanu, J.-L. Brédas, P.J. Skabara, Mater. Horiz. 3 (4) (2016) 333–339.
[198] H. Huang, L. Yang, A. Facchetti, T.J. Marks, Chem. Rev. 117 (15) (2017) 10291–10318.
[199] R.C. Jemison, R.D. McCullough, Techniques for the Molecular Design of Push-Pull Polymers towards Enhanced Organic Photovoltaic Performance, in: Polymer Composites for Energy Harvesting, Conversion, and Storage; ACS Symposium Series; American Chemical Society, 1161, 2014, pp. 4–71.
[200] J.D. Azoulay, Z.A. Koretz, B.M. Wong, G.C. Bazan, Macromolecules 46 (2013) 1337–1342.
[201] J. Mei, Z. Bao, Chem. Mater. 26 (1) (2014) 604–615.
[202] A. London, L. Huang, B. Zhang, B. Oviedo, J. Tropp, W. Yao, Z. Wu, B. Wong, T. N. Ng, J.D. Azoulay, Polym. Chem. 8 (2017) 2922–2930.
[203] D.B. Sulas, A.E. London, L. Huang, L. Xu, Z. Wu, T.N. Ng, B.M. Wong, C. W. Schlenker, J.D. Azoulay, M.Y. Sfeir, Adv. Opt. Mater. 6 (2018), 1701138.
[204] W. Yao, Z. Wu, E. Huang, L. Huang, A.E. London, Z. Liu, J.D. Azoulay, T.N. Ng, ACS Appl. Electron. Mater. 1 (2019) 660–666.
[205] F. Verstraeten, S. Gielen, P. Verstappen, J. Raymakers, H. Penxten, L. Lutsen, K. Vandewal, W. Maes, J. Mater. Chem. C 8 (29) (2020) 10098–10103.
[206] J. Han, D. Yang, L. Hu, D. Ma, W. Qiao, Z.Y. Wang, Chem. Select 3 (25) (2018) 7385–7393.
[207] N. Li, Z. Lan, Y.S. Lau, J. Xie, D. Zhao, F. Zhu, Adv. Sci. 7 (14) (2020), 2000444.
[208] K. Strassel, W.-H. Hu, S. Osbild, D. Padula, D. Rentsch, S. Yakunin, Y. Shynkarenko, M. Kovalenko, F. Nüesch, R. Hany, M. Bauer, Sci. Technol. Adv. Mater. 22 (1) (2021) 194–204.
[209] J.S. Wilson, N. Chawdhury, M.R.A. Al-Mandhary, M. Younus, M.S. Khan, P. R. Raithby, A. Köhler, R.H. Friend, J. Am. Chem. Soc. 123 (38) (2001) 9412.
[210] Y.C. Wei, S.F. Wang, Y. Hu, L.S. Liao, D.G. Chen, K.H. Chang, C.W. Wang, S. H. Liu, W.H. Chan, J.L. Liao, W.Y. Hung, T.H. Wang, P.T. Chen, H.F. Hsu, Y. Chi, P.T. Chou, Nat. Photonics 14 (9) (2020) 570–577.
[211] N.A. Ran, S. Roland, J.A. Love, V. Savikhin, C.J. Takacs, Y.T. Fu, H. Li, V. Coropceanu, X. Liu, J.L. Brédas, G.C. Bazan, M.F. Toney, Di. Neher, T. Q. Nguyen, Nat. Commun. 8 (1) (2017) 79.
[212] F.C. Spano, C. Silva, Annu. Rev. Phys. Chem. 65 (1) (2014) 477–500.
[213] S.M. Menke, N.A. Ran, G.C. Bazan, R.H. Friend, Joule 2 (1) (2018) 25–35.
[214] L. Huang, N. Eedugurala, A. Benasco, S. Zhang, K.S. Mayer, D.J. Adams, B. Fowler, M.M. Lockart, M. Saghayezhian, H. Tahir, E.R. King, S. Morgan, M. K. Bowman, X. Gu, J.D. Azoulay, Adv. Funct. Mater. 30 (24) (2020), 1909805.
[215] K. Wang, L. Huang, N. Eedugurala, S. Zhang, M.A. Sabuj, N. Rai, X. Gu, J. D. Azoulay, T.N. Ng, Adv. Energy Mater. 9 (47) (2019), 1902806.
[216] J.H. Vella, L. Huang, N. Eedugurala, K. Mayer, T.N. Ng, J. Azoulay, Sci. Adv. 7 (24) (2021) abg2418.
[217] S. Chen, C. Teng, M. Zhang, Y. Li, D. Xie, G. Shi, Adv. Mater. 4 (6) (2016) 5969–5974.
[218] J. Lee, S.J. Ko, H. Lee, J. Huang, Z. Zhu, M. Seifrid, J. Vollbrecht, V.V. Brus, A. Karki, H. Wang, K. Cho, T.Q. Nguyen, G.C. Bazan, ACS Energy Lett. (2019) 1401–1409.
[219] T.J. Wen, D. Wang, L. Tao, Y. Xiao, Y.D. Tao, Y. Li, X. Lu, Y. Fang, C.Z. Li, H. Chen, D. Yang, ACS Appl. Mater. Interfaces 12 (35) (2020) 39515–39523.
[220] D. Tordera, B. Peeters, E. Delvitto, S. Shanmugam, J. Maas, J. de Riet, R. Verbeek, R. van de Laar, T. Bel, G. Haas, L. Ugalde, A. van Breemen, I. Katsouras, A. J. Kronemeijer, H. Akkerman, E. Meulenkamp, G. Gelinck, J. Soc. Inf. Disp. 28 (5) (2020) 381–391.
[221] L. Shen, Y. Lin, C. Bao, Y. Bai, Y. Deng, M. Wang, T. Li, Y. Lu, A. Gruverman, W. Li, J. Huang, Mater. Horiz. 4 (2) (2017) 242–248.
[222] Q. Lin, Z. Wang, M. Young, J.B. Patel, R.L. Milot, L. Martinez Maestro, R.R. Lunt, H.J. Snaith, M.B. Johnston, L.M. Herz, Adv. Funct. Mater. 27 (38) (2017) 1–7.
[223] Y. He, J.T.E. Quinn, D. Hou, J.H.L. Ngai, Y. Li, J. Mater. Chem. C 5 (46) (2017) 12163–12171.
[224] H. Xu, J. Liu, J. Zhang, G. Zhou, N. Luo, N. Zhao, Adv. Mater. 29 (31) (2017), 1700975.
[225] G. Wang, K. Huang, Z. Liu, Y. Du, X. Wang, H. Lu, G. Zhang, L. Qiu, ACS Appl. Mater. Interfaces 10 (42) (2018) 36177–36186.
[226] F. Li, Y. Chen, C. Ma, U. Buttner, K. Leo, T. Wu, Adv. Electron. Mater. 3 (1) (2017) 1600430.
[227] J.H. Jung, M.J. Yoon, J.W. Lim, Y.H. Lee, K.E. Lee, D.H. Kim, J.H. Oh, Adv. Funct. Mater. 27 (6) (2017) 1604528.
[228] N. Li, Y. Lei, W.K.E. Chan, F. Zhu, J. Mater. Chem. C 7 (16) (2019) 4808–4816.
[229] M.A. Iqbal, A. Liaqat, S. Hussain, X. Wang, M. Tahir, Z. Urooj, L. Xie, Adv. Mater. 32 (37) (2020) 2002628.
[230] G. Xing, N. Mathews, S.S. Lim, Y.M. Lam, S. Mhaisalkar, T.C. Sum, Science 342 (6156) (2013) 344–347.
[231] F. Hao, C.C. Stoumpos, D.H. Cao, R.P.H. Chang, M.G. Kanatzidis, Nat. Photonics 8 (6) (2014) 489–494.
[232] M.J.P. Alcocer, T. Leijtens, L.M. Herz, A. Petrozza, H.J. Snaith, Science 342 (5156) (2013) 341–344.
[233] Q. Lin, A. Armin, R.C.R. Nagiri, P.L. Burn, P. Meredith, Nat. Photonics 9 (2) (2015) 106–112.
[234] L.M. Herz, ACS Energy Lett. 2 (7) (2017) 1539–1548.
[235] D. Barrit, P. Cheng, M.C. Tang, K. Wang, H. Dang, D.M. Smilgies, S. Liu, T. D. Anthopoulos, K. Zhao, A. Amassian, Adv. Funct. Mater. 29 (47) (2019), 1807544.
[236] P. Wang, Y. Wu, B. Cai, Q. Ma, X. Zheng, W.H. Zhang, Adv. Funct. Mater. 29 (47) (2019), 1807661.
[237] J. Zhao, L. Zhao, Y. Deng, X. Xiao, Z. Ni, S. Xu, J. Huang, Nat. Photonics 14 (10) (2020) 612–617.
[238] H. Wei, Y. Fang, P. Mulligan, W. Chuirazzi, H.H. Fang, C. Wang, B.R. Ecker, Y. Gao, M.A. Loi, L. Cao, J. Huang, Nat. Photonics 10 (5) (2016) 333–339.
[239] H. Wei, J. Huang, Nat. Commun. 10 (1) (2019) 1066.
[240] Y. Li, Y. Zhang, T. Li, M. Li, Z. Chen, Q. Li, H. Zhao, Q. Sheng, W. Shi, J. Yao, Nano Lett. 20 (2020) 5646–5654.
[241] S. De Wolf, J. Holovsky, S.J. Moon, P. Löper, B. Niesen, M. Ledinsky, F.J. Haug, J. H. Yum, C. Ballif, J. Phys. Chem. Lett. 5 (6) (2014) 1035–1039.
[242] L. Dou, Y.M. Yang, J. You, Z. Hong, W.H. Chang, G. Li, Y. Yang, Nat. Commun. 5 (2014) 5404.
[243] C. Bao, W. Xu, J. Yang, S. Bai, P. Teng, Y. Yang, J. Wang, N. Zhao, W. Zhang, W. Huang, F. Gao, Nat. Electron. 3 (3) (2020) 156–164.
[244] Y. Ogomi, A. Morita, S. Tsukamoto, T. Saitho, N. Fujikawa, Q. Shen, T. Toyoda, K. Yoshino, S.S. Pandey, S. Hayase, J. Phys. Chem. Lett. 5 (2014) 1004–1011.
[245] S.J. Lee, S.S. Shin, Y.C. Kim, D. Kim, T.K. Ahn, J.H. Noh, J. Seo, S.Il Seok, J. Am. Chem. Soc. 138 (12) (2016) 3974–3977.
[246] F. Hao, C.C. Stoumpos, R.P.H. Chang, M.G. Kanatzidis, J. Am. Chem. Soc. 136 (22) (2014) 8094–8099.
[247] Y. Li, W. Sun, W. Yan, S. Ye, H. Rao, H. Peng, Z. Zhao, Z. Bian, Z. Liu, H. Zhou, C. Huang, Adv. Energy Mater. 6 (24) (2016), 1601353.
[248] R. Wang, M. Mujahid, Y. Duan, Z.K. Wang, J. Xue, Y. Yang, Adv. Funct. Mater. 29 (47) (2019), 1808843.
[249] M.V. Khenkin, E.A. Katz, A. Abate, G. Bardizza, J.J. Berry, C. Brabec, F. Brunetti, V. Bulović, Q. Burlingame, A. Di Carlo, R. Cheacharoen, Y.B. Cheng, A. Colsmann, S. Cros, K. Domanski, M. Dusza, C.J. Fell, S.R. Forrest, Y. Galagan, D. Di Girolamo, M. Grätzel, A. Hagfeldt, E. von Hauff, H. Hoppe, J. Kettle, H. Köbler, M.S. Leite, S. Liu, Y.L. Loo, J.M. Luther, C.Q. Ma, M. Madsen, M. Manceau, M. Matheron, M. McGehee, R. Meitzner, M.K. Nazeeruddin, A.F. Nogueira, Ç. Odabaşı, A. Osherov, N.G. Park, M.O. Reese, F. De Rossi, M. Saliba, U.S. Schubert, H. J. Snaith, S.D. Stranks, W. Tress, P.A. Troshin, V. Turkovic, S. Veenstra, I. Visoly-Fisher, A. Walsh, T. Watson, H. Xie, R. Yıldırım, S.M. Zakeeruddin, K. Zhu, M. Lira-Cantu, Nat. Energy 5 (1) (2020) 35–49.
[250] Z. Zheng, F. Zhuge, Y. Wang, J. Zhang, L. Gan, X. Zhou, H. Li, T. Zhai, Adv. Funct. Mater. 27 (43) (2017) 1–12.
[251] S. Tong, J. Sun, C. Wang, Y. Huang, C. Zhang, J. Shen, H. Xie, D. Niu, S. Xiao, Y. Yuan, J. He, J. Yang, Y. Gao, Adv. Electron. Mater. 3 (7) (2017) 1–8.
[252] B. Wang, Y. Zou, H. Lu, W. Kong, S.C. Singh, C. Zhao, C. Yao, J. Xing, X. Zheng, Z. Yu, C. Tong, W. Xin, W. Yu, B. Zhao, C. Guo, Small 16 (24) (2020), 2001417.
[253] C.K. Liu, Q. Tai, N. Wang, G. Tang, H.L. Loi, F. Yan, Adv. Sci. 6 (17) (2019), 1900751.
[254] J. Ding, H. Fang, Z. Lian, J. Li, Q. Lv, L. Wang, J.L. Sun, Q. Yan, CrystEngComm 18 (23) (2016) 4405–4411.
[255] F. Cao, L. Meng, M. Wang, W. Tian, L. Li, Adv. Mater. 31 (12) (2019) 1–7.
[256] N. Li, W. Lan, Y.S. Lau, L. Cai, A.A. Syed, F. Zhu, J. Mater. Chem. C 7 (31) (2019) 9573–9580.
[257] X. Xu, C.C. Chueh, P. Jing, Z. Yang, X. Shi, T. Zhao, L.Y. Lin, A.K.Y. Jen, Adv. Funct. Mater. 27 (28) (2017) 1–6.
[258] H.L. Zhu, Z. Liang, Z. Huo, W.K. Ng, J. Mao, K.S. Wong, W.J. Yin, W.C.H. Choy, Adv. Funct. Mater. 28 (16) (2018) 1706068.
[259] X. Zou, Y. Li, G. Tang, P. You, F. Yan, Small 15 (25) (2019) 1–9.
[260] D.H. Kang, S.R. Pae, J. Shim, G. Yoo, J. Jeon, J.W. Leem, J.S. Yu, S. Lee, B. Shin, J. H. Park, Adv. Mater. 28 (35) (2016) 7799–7806.
[261] Z.Y. Peng, J.L. Xu, J.Y. Zhang, X. Gao, S.D. Wang, Adv. Mater. Interfaces 5 (18) (2018) 1–7.
[262] S. Wei, F. Wang, X. Zou, L. Wang, C. Liu, X. Liu, W. Hu, Z. Fan, J.C. Ho, L. Liao, Adv. Mater. 32 (6) (2020) 1–9.
[263] Z. Lan, Y.S. Lau, Y. Wang, Z. Xiao, L. Ding, D. Luo, F. Zhu, Adv. Opt. Mater. 8 (24) (2020), 2001388.
[264] Q. Lin, Q. Lin, A. Armin, P.L. Burn, P. Meredith, Nat. Photonics 9 (10) (2015) 687.
[265] A. Armin, R.D. Jansen-van Vuuren, N. Kopidakis, P.L. Burn, P. Meredith, Nat. Commun. 6 (1) (2015) 6343.
[266] Y. Khan, D. Han, A. Pierre, J. Ting, X. Wang, C.M. Lochner, G. Bovo, N. Yaacobi-Gross, C. Newsome, R. Wilson, A.C. Arias, Proc. Natl. Acad. Sci. 115 (47) (2018) E11015–E11024.
[267] T.N. Ng, D.E. Schwartz, P. Mei, B. Krusor, S. Kor, J. Veres, P. Bröms, T. Eriksson, Y. Wang, O. Hagel, C. Karlsson, Sci. Rep. 5 (1) (2015) 13457.
[268] H. Zhang, S. Jenatsch, J. De Jonghe, F. Nuësch, R. Steim, A.C. Véron, R. Hany, Sci. Rep. 5 (2015) 9439.
[269] X. Tang, Gfu Wu, K.W.C. Lai, J. Mater. Chem. C 5 (2) (2017) 362–369.
[270] M.R. Antognazza, U. Scherf, P. Monti, G. Lanzani, Appl. Phys. Lett. 90 (16) (2007) 21–24.
[271] W. Li, D. Li, G. Dong, L. Duan, J. Sun, D. Zhang, L. Wang, Laser Photon. Rev. 10 (3) (2016) 473–480.
[272] D.S. Leem, K.H. Lee, N. Li, B.W. Park, T. Choi, T. Ro, O.K. Kwon, Y.N. Kwon, T. N. Ng, S. Kim, Adv. Opt. Mater. 9 (4) (2020), 2001682.
[273] X. Tang, M.M. Ackerman, P. Guyot-Sionnest, ACS Nano (2018) 7362–7370.
[274] S.A. Pollack, Appl. Opt. 5 (11) (1966) 1749.
[275] Y. Zhong, T.J. Sisto, B. Zhang, K. Miyata, X.Y. Zhu, M.L. Steigerwald, F. Ng, C. Nuckolls, J. Am. Chem. Soc. 139 (16) (2017) 5644–5647.
[276] L. Shen, Y. Zhang, Y. Bai, X. Zheng, Q. Wang, J. Huang, Nanoscale 8 (26) (2016) 12990–12997.
[277] W. Wang, F. Zhang, M. Du, L. Li, M. Zhang, K. Wang, Y. Wang, B. Hu, Y. Fang, J. Huang, Nano Lett. 17 (3) (2017) 1995–2002.
[278] D.Y. Kim, D.W. Song, N. Chopra, P. De Somer, F. So, Adv. Mater. 22 (20) (2010) 2260–2263.

[279] N. Li, Y.S. Lau, Z. Xiao, L. Ding, F. Zhu, Adv. Opt. Mater. (2018), 1801084.
[280] S.W. Liu, C.C. Lee, C.H. Yuan, W.C. Su, S.Y. Lin, W.C. Chang, B.Y. Huang, C.F. Lin, Y.Z. Lee, T.H. Su, K.T. Chen, Adv. Mater. 27 (7) (2015) 1217–1222.
[281] D. Yang, X. Zhou, D. Ma, A. Vadim, T. Ahamad, S.M. Alshehri, Mater. Horiz. 5 (5) (2018) 874–882.
[282] Q. Song, T. Lin, Z. Su, B. Chu, H. Yang, W. Li, C.S. Lee, J. Phys. Chem. Lett. 9 (23) (2018) 6818–6824.
[283] D.Y. Kim, K.R. Choudhury, J.W. Lee, D.W. Song, G. Sarasqueta, F. So, Nano Lett. 11 (5) (2011) 2109–2113.
[284] Z. Xu, Z. Huang, T. Jin, T. Lian, M.L. Tang, Acc. Chem. Res. 54 (2020) 70.
[285] Y. Zhai, Z. Wang, K.S. Kwon, S. Cai, D. Lipomi, T.N. Ng, Adv. Mater. 33 (19) (2020), 2002541.
[286] T.N. Ng, D.E. Schwartz, P. Mei, S. Kor, J. Veres, P. Bröms, C. Karlsson, Flex. Print. Electron. 1 (1) (2016) 15002.
[287] K.N. Al-Milaji, R.R. Secondo, T.N. Ng, N. Kinsey, H. Zhao, Adv. Mater. Interfaces 5 (10) (2018), 1701561.
[288] Y. Bonnassieux, C.J. Brabec, Y. Cao, T.B. Carmichael, M.L. Chabinyc, K. Cheng, G. Cho, A. Chung, C.L. Cobb, A. Distler, H.-J. Egelhaaf, G. Grau, X. Guo, G. Haghiashtiani, T.-C. Huang, M.M. Hussain, B. Iniguez, T. Lee, L. Li, Y. Ma, D. Ma, M.C. McAlpine, T.N. Ng, R. Osterbacka, S. Patel, J. Peng, H. Peng, J. Rivnay, L. Shao, D. Steingart, R.A. Street, V. Subramanian, L. Torsi, Y. Wu, Flex. Print. Electron. 6 (2) (2021) 023001.
[289] G. Grau, J. Cen, H. Kang, R. Kitsomboonloha, W.J. Scheideler, V. Subramanian, Flex. Print. Electron. 1 (2) (2016), 023002.
[290] S. Wu, L. Yao, A. Shiller, A.H. Barnard, J.D. Azoulay, Adv. Electron. Mater. 7 (6) (2021), 2100223.
[291] V.R. Feig, H. Tran, Z. Bao, ACS Cent. Sci. 4 (3) (2018) 337–348.
[292] K. Kwon, T.N. Ng, Org. Electron. 15 (1) (2014) 294–298.
[293] Y.J. Tan, H. Godaba, G. Chen, S.T.M. Tan, G. Wan, G. Li, P.M. Lee, Y. Cai, S. Li, R. F. Shepherd, J.S. Ho, B.C.K. Tee, Nat. Mater. 19 (2) (2020) 182–188.
[294] R. Ma, S.Y. Chou, Y. Xie, Q. Pei, Chem. Soc. Rev. 48 (6) (2019) 1741–1786.
[295] T.N. Ng, W.S. Wong, R.A. Lujan, R.A. Street, Adv. Mater. 21 (18) (2009) 1855–1859.
[296] K. Wang, L. Yao, M. Jahon, J. Liu, M. Gonzalez, P. Liu, V. Leung, X. Zhang, T. N. Ng, ACS Energy Lett. 5 (2020) 3276–3284.
[297] B.C.-K.C.-K. Tee, A. Chortos, A. Berndt, A.K. Nguyen, A. Tom, A. McGuire, Z. C. Lin, K. Tien, W.-G.W.-G. Bae, H. Wang, P. Mei, H.-H. Chou, B. Cui, K. Deisseroth, T.N. Ng, Z. Bao, Science 350 (6258) (2015) 313–316.
[298] M. Amit, L. Chukoskie, A.J. Skalsky, H. Garudadri, T.N. Ng, Adv. Funct. Mater. 30 (20) (2019), 1905241.
[299] K. Wang, U. Parekh, T. Pailla, H. Garudadri, V. Gilja, T.N. Ng, Adv. Healthc. Mater. 6 (19) (2017), 1700552.
[300] Z. Wu, W. Yao, A.E. London, J.D. Azoulay, T.N. Ng, ACS Appl. Mater. Interfaces 9 (2017) 1654–1660.
[301] S. Park, K. Fukuda, M. Wang, C. Lee, T. Yokata, H. Jin, H. Jinno, H. Kimura, P. Zalar, N. Matshuhisa, S. Umezu, G.C. Bazan, T. Someya, Adv. Mater. 30 (34) (2018), 1802359.
[302] T. Yokota, P. Zalar, M. Kaltenbrunner, H. Jinno, N. Matsuhisa, H. Kitanosako, Y. Tachibana, W. Yukita, M. Koizumi, T. Someya, Sci. Adv. 2 (4) (2016) e1501856–e1501856.
[303] L. Gu, S. Poddar, Y. Lin, Z. Long, D. Zhang, Q. Zhang, L. Shu, X. Qiu, M. Kam, A. Javey, Z. Fan, Nature 581 (7808) (2020) 278–282.
[304] H.C. Ko, M.P. Stoykovich, J. Song, V. Malyarchuk, W.M. Choi, C.J. Yu, J.B. Geddes, J. Xiao, S. Wang, Y. Huang, J.A. Rogers, Nature 454 (7205) (2008) 748–753.
[305] S.-B. Rim, P.B. Catrysse, R. Dinyari, K. Huang, P. Peumans, Opt. Express 16 (7) (2008) 4965.
[306] T.N. Ng, W.S. Wong, M.L. Chabinyc, S. Sambandan, R.A. Street, Appl. Phys. Lett. 92 (21) (2008), 213303.
[307] J.F. Maya-Vetencourt, D. Ghezzi, M.R. Antognazza, E. Colombo, M. Mete, P. Feyen, A. Desii, A. Buschiazzo, M. Di Paolo, S. Di Marco, F. Ticconi, L. Emionite, D. Shmal, C. Marini, I. Donelli, G. Freddi, R. MacCarone, S. Bisti, G. Sambuceti, G. Pertile, G. Lanzani, F. Benfenati, Nat. Mater. 16 (6) (2017) 681–689.
[308] G. Simone, D. Di Carlo Rasi, X. de Vries, G.H.L. Heintges, S.C.J. Meskers, R.A. J. Janssen, G.H. Gelinck, Adv. Mater. 30 (51) (2018), 1804678.
[309] A. Vásquez Quintero, P. Pérez-Merino, H. De Smet, Sci. Rep. 10 (1) (2020) 14641.

Ning Li received his BS in optoelectronics and MSC in optics engineering from Shandong University in 2012 and 2015, respectively. Then he continued his PhD study in Hong Kong Baptist University with a major in physics, studying the solution processable semiconductors for optoelectronic applications, and earned the degree in 2018. Currently, as a postdoc researcher in professor Ng's group at UCSD, his research interests are focused on infrared light sensing and imaging technology for medical applications, by using solution-based techniques.

Paramasivam Mahalingavelar received his Ph.D. in Materials Chemistry from the CSIR-Indian Institute of Chemical Technology (2014), Hyderabad, India. After the post-doctoral stays at IIT Gandhinagar and Korea University, he joined Prof. Jason D. Azoulay research group as a post-doctoral research associate at the University of Southern Mississippi. His current research mainly focuses on the design and synthesis of shortwave infrared (SWIR) polymers for organic photodiode, phototransistor, photodetector applications and evaluating their structure-property relationship at the molecular level using various computational techniques.

Jarrett H. Vella received his Ph.D. in Chemistry from the University of Florida Gainsville. He is a Research Chemist in the Sensors Directorate in the US Air Force Research Laboratory since 2010. His research is focused on optical infrared materials and devices, ranging from pyroelectric detectors, plasmonic structures, photonic devices, and focal plane arrays.

Dong-Seok Leem received his Ph.D. in Materials from Gwangju Institute of Science and Technology (GIST), Republic of Korea in 2006. After then he worked in the OLED Center at Seoul National University (2006–2008) and Centre for Plastic Electronics at Imperial College London (2008–2010) as a postdoc. He joined Samsung Advanced Institute of Technology (SAIT) in 2011 and now a principle researcher in Organic Material Lab. His main research field is organic photodiodes, infrared materials, and their sensor applications.

Jason D. Azoulay received his Ph.D. in Chemistry in 2010 from the University of California Santa Barbara (UCSB), where he studied late transition metal catalysts for olefin polymerization. Afterward, he performed his postdoctoral studies at the Center for Polymers and Organic Solids at UCSB (2010–2011) then Sandia National Laboratories (2011–2014) in electronic and photonic materials research. He is an Associate Professor of Polymer Science and Engineering at The University of Southern Mississippi. His research group studies electronic, photonic, magnetic, and quantum materials; homogeneous catalysis applied to polymer synthesis; and multidisciplinary investigations that address large scale objectives in materials development.

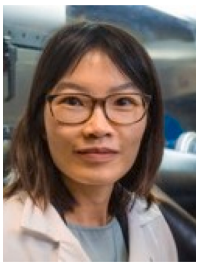

Tse Nga Ng received her Ph.D. in physical chemistry from Cornell University and started her career at Xerox Palo Alto Research Center prior to joining UCSD in 2016. She is an Associate Professor in the Electrical and Computer Engineering Department at University of California San Diego. Her research group studies methodologies to fabricate large-area optoelectronics and thin-film devices for human-computer interfaces, to seamlessly integrate electronics onto any surfaces or structures towards the vision of ubiquitous computing. She has authored 56+ peer-reviewed papers and is an inventor on more than 39 patents in the area of materials and processes for flexible printed electronics.